

**First-Principles Computational Analyses of
Catalytic Dehydrogenation and Cracking of Hydrocarbon Fuels**

A Dissertation Presented to
the Faculty of the School of Engineering and Applied Science
University of Virginia

In Partial Fulfillment
of the Requirement for the Degree
Doctor of Philosophy in Chemical Engineering

by

Qiang Qian

May 2014

APPROVAL SHEET

The dissertation is submitted in partial fulfillment of the requirements
for the degree of
Doctor of Philosophy



AUTHOR

This dissertation has been read and approved by the examining committee:

Prof. Matthew Neurock

Advisor

Prof. Robert J. Davis

Prof. Roseanne M. Ford

Prof. Ian Harrison

Prof. Giovanni Zangari

Accepted for the School of Engineering and Applied Science:



Dean, School of Engineering and Applied Science
May 2014

Abstract

The development of heterogeneous catalytic materials that can be used to promote the regenerative cooling of jet fuels and enhance their subsequent catalytic combustion is of great importance in engineering advanced hypersonic propulsion systems. First-principles density functional theory (DFT) calculations were carried out to examine elementary reaction paths, plausible mechanisms and the nature of the active catalytic sites involved in the catalytic dehydrogenation over supported metal and metal oxide clusters and catalytic cracking over solid acid catalysts. More specifically we examined the influence of the size, shape and composition of the metal as well as the influence of the support in the catalytic dehydrogenation and the role of solid acid acidity on the catalytic cracking of alkanes.

Propane and cyclohexane were used as surrogate molecules for the catalytic dehydrogenation of longer chain hydrocarbons in jet fuel over sub-nanometer Pt_n and Co_n clusters. The intrinsic barriers for activating the secondary C-H bond of propane at metal sites with same coordination numbers were found to be directly correlated with the calculated chemical hardness properties of Pt_n and Co_n clusters. The negatively charged Pt sites on supported Pt_n clusters were found to be less active for C-H activation than the same sites on freestanding Pt_n clusters. On nanometer-sized Pt particles, ratio of collective rates of cyclohexene dehydrogenation and desorption reactions at different surface sites all over a truncated cubo-octahedral particle with high surface coverage indicate that smaller particles favor cyclohexene dehydrogenation towards benzene while larger particles favor desorption of cyclohexene. The calculations were found to be in good agreement with reported experimental results.

Model Au/Co_3O_4 catalysts were used to examine the catalytic oxidative dehydrogenation of cyclohexane (a surrogate for naphthenic fuels), a first step toward catalytic oxidation and combustion. DFT results show that the Au particles transfer electrons to the Co_3O_4 support upon adsorption. The charge is localized near the gold-oxide interface, which subsequently weakens the Co-O bond and increases the hydrogen affinity of the O sites,

thus lowers the activation barrier of initial C-H bond activation of cyclohexane while increasing the reducibility of the Co_3O_4 support. These results help to provide a fundamental understanding of the experimentally observed reactivity increases in the oxidative dehydrogenation of cyclohexane over $\text{Au}/\text{Co}_3\text{O}_4$ as compared to that on pure Co_3O_4 surfaces.

Catalytic cracking offers a second, and perhaps more viable, reaction that can be used to remove heat in jet propulsion systems. Butane cracking was carried out computationally over a series of model solid acid catalytic materials including polyoxotungstates and WO_x clusters supported on ZrO_2 substrates in order to elucidate the role of catalyst structure and acidity on the cracking of model hydrocarbon intermediates. The deprotonation energy (DPE) was used as a direct measure of the Brønsted acidity and was used to correlate with reactivity studies. Zr-containing polyoxotungstates of different structural forms (Dawson, Keggin, Lindqvist) were found to be more acidic than two-dimensional surface tungstate clusters supported on ZrO_2 . The calculated activation barriers for these reactions were found to directly correlate to the acidity of the catalyst. The sensitivity of activation barrier to the changes in DPE were found to be different for different elementary reaction steps which reflect the differences in the sensitivity of the reactions to acid site strength. The different sensitivities may help to aid in the development of solid acid catalysts that can promote cracking and minimize coking.

Acknowledgements

First and foremost, I would like to express my sincere gratitude to my advisor, Professor Matthew Neurock, for the excellent academic training with his patience, knowledge and high standards. I also wish to thank my advisory and examining committee.

My special thanks go to our outstanding experimental collaborators at the Argonne National Laboratory, Yale University, Tufts University and University of Virginia. I am also indebted to all of my colleagues in the computational catalysis group for stimulating discussions and critical reviews of my manuscripts, especially the help from Steven Merz and Eric Dybeck during the final stage of writing this thesis. It has been a great pleasure working with and getting to know Dr. Corneliu Buda, Dr. Yu Cai, Dr. Lijun Xu, Dr. Wenjie Tang, Dr. Brian Prascher, Dr. Michael Francis, Dr. David Hibbitts and Dr. Craig Plaisance.

My greatest debt is to my parents, for their continuous unconditional love, support and encouragement. I am also grateful to all friends who positively influenced me in recent years, especially Mrs. Trotman, Mr. Yee, Zhou, and Ying.

Financial support of this work was provided by the AFOSR MURI grant FA9550-08-0309. The computational research was performed by using the ITC Linux cluster at University of Virginia, the Chinook supercomputer at EMSL of the Pacific Northwest National Laboratory, and the Extreme Science and Engineering Discovery Environment (XSEDE) supported by National Science Foundation grant number OCI-1053575.

献给父母亲大人

To my dearest parents

Table of Contents

Chapter 1 Introduction	1
1.1 Motivation.....	1
1.2 Methodology.....	3
1.2.1 Density functional theory.....	3
1.2.2 Bloch's theorem and supercell approach.....	6
1.2.3 Brillouin zone sampling.....	7
1.2.4 Plane wave basis set and pseudopotential approximation.....	8
1.2.5 Transition state theory.....	9
1.3 Overview of chapters.....	10
References.....	11
Chapter 2 Propane Dehydrogenation on Pt and Co sub-nm clusters	13
2.1 Introduction.....	13
2.2 Method.....	16
2.3 Results and Discussion.....	19
2.3.1 Propane activation on bare Pt _n and Co _n clusters.....	19
2.3.2 Charge analyses.....	24
2.3.3 Propane Dehydrogenation on CNT supported Pt ₅ clusters.....	31
2.4 Summary.....	35
Supplementary Materials.....	36
References.....	38
Chapter 3 Selective Dehydrogenation of Cyclohexane on Pt nm-particles	41
3.1 Introduction.....	41
3.2 Method.....	43
3.3 Results and Discussion.....	47
3.3.1 Plausible reaction paths of c-C ₆ H ₁₂ dehydrogenation on bare Pt ₅₅ and Pt ₂₀₁	47
3.3.2 Statistical sampling of reactions over bare and covered Pt nanoparticles.....	50
3.3.3 Selectivity of cyclohexane dehydrogenation.....	60
3.4 Summary.....	63

Supplementary Materials	64
References.....	72
Chapter 4 Oxidative Dehydrogenation of Cyclohexane on Au/Co₃O₄	74
4.1 Introduction.....	74
4.2 Method	77
4.3 Results and Discussion	80
4.3.1 C-H bond activation of cyclohexane.....	80
4.3.2 O ₂ activation.....	84
4.3.3 Reducibility of the oxide surface	87
4.4 Summary.....	89
References.....	90
Chapter 5 Catalytic Cracking of Hydrocarbons on Solid Acid Catalysts	93
5.1 Introduction.....	93
5.2 Method	96
5.2.1 Computational Details	96
5.2.2 Measurement of Acid Strength	97
5.3 Results and Discussion	100
5.3.1 Monomolecular and bimolecular cracking	100
5.3.2 More discussion on monomolecular cracking	104
5.3.3 Structure-reactivity relationships.....	108
5.3.4 Reactions related to coke formation	111
5.4 Summary.....	113
Supplementary Materials	114
References.....	117
Chapter 6 Conclusions and Recommendations	120
6.1 Conclusions.....	120
6.2 Recommendations.....	123

Chapter 1 Introduction

1.1 Motivation

As aircrafts reach supersonic and hypersonic speeds, conventional gas-turbine jet engines become inefficient and need to be replaced by hypersonic airbreathing propulsion systems, such as ramjets (Mach 3~6) and scramjets (Mach >6) [1]. Operating at such a high speed, these aircrafts experience high temperatures caused by aerodynamic heating primarily at its leading edge and within the engine. Regenerative cooling using onboard jet fuels as the primary coolant is thought to be the best solution for thermal management, which circulates fuels behind the walls of various aircraft components and removes waste heat before the injection of fuels to the combustion chamber [2]. The heat sink requirement for jet fuels was estimated as a function of the flight speed (e.g. 1.4 MJ kg⁻¹ at Mach 4; 2.7 MJ kg⁻¹ at Mach 6; and 4.6 MJ kg⁻¹ at Mach 8, for manned aircrafts) [3]. Heating typical hydrocarbon fuels from ambient temperature to about 500 °C results in the absorption of 1.6 ~ 1.8 MJ kg⁻¹ sensible heat, which provides a sufficient heat sink for aircrafts with a speed up to Mach 5, whereas beyond this limit additional cooling is needed. This extra heat sink capacity for hydrocarbon fuels can be obtained by endothermic reactions [3-6], such as dehydrogenation and cracking which involve C-H and C-C bond activation, respectively. The catalytic dehydrogenation of naphthenic fuels and surrogate model fuels, such as the dehydrogenation of methylcyclohexane to form toluene and hydrogen (chemical heat sink of 2.2 MJ kg⁻¹), have been intensely examined since the 1960s [3, 7, 8]. The emphasis on catalytic dehydrogenation has decreased as the dehydrogenation of the naphthenics usually generates aromatics, which increase soot formation [5]. On the other hand, thermal and

catalytic cracking has received considerable attention since the 1960s [4, 9-11]. In this dissertation, propane and cyclohexane are used as surrogate molecules of fuel to examine the mechanisms for the catalytic dehydrogenation reactions over metal and metal oxide nanoparticles, whereas butane is used as a model system to study catalytic cracking reactions.

Besides acting as a coolant, the hydrocarbon jet fuel's primary function is of course combustion which is required for thrust. Catalysts that are added to the fuel can be used to not only aid in endothermic reactions but also enhance hydrocarbon combustion reactions by lowering the ignition temperatures, reducing soot formation, abating CO, NO_x, and light hydrocarbons emissions in the exhaust gas [12, 13]. Catalytic combustion at leaner fuel-to-air ratios has already been implemented in industrial gas turbines [14-16]. In this dissertation, we examine the catalytic oxidative dehydrogenation of light alkanes as model fuels, and more specifically we examine the partial oxidation of cyclohexane (a surrogate fuel model), which is considered the first step in total oxidation or combustion.

1.2 Methodology

First-principles periodic density functional theory (DFT) calculations are carried out in this dissertation to examine the catalytic kinetics, pathways and mechanisms as well as the catalyst sites responsible for carrying out catalytic reactions. Compared with other *ab initio* electronic structure methods, such as Møller–Plesset perturbation theory (MPn) [17] and coupled cluster theory (CC) [18], density functional theory provides reliable accuracy at a much lower cost. Current state-of-the-art DFT calculations can reliably handle hundreds of heavy atoms and explicitly model the intrinsic kinetics and pathways and, as such, be used to examine the apparent kinetics and catalytic sites that carry out these transformations.

1.2.1 Density functional theory

The interactions among electrons and atomic nuclei can be described by solving Schrödinger's equation. The equations are too complicated and cannot be solved directly for any systems larger than H₂. As a result, a number of simplifications are required in order to allow for the solution of these large many-body problems. Due to the large difference between the mass of nuclei and electrons, the nuclear and electronic coordinates in the many-body wave function can be separated via the well-known Born-Oppenheimer [19] approximation. Density functional theory further simplifies the problem of N -interacting electrons over $3N$ spatial coordinates to one problem which solves electron interactions over 3 spatial coordinates. Hohenberg and Kohn [20] were the first to demonstrate that (1) the ground-state energy of a system of N - interacting electrons is a unique functional of its electron density; (2) the ground-state energy can be determined by minimizing the energy functional; and (3) the density that results in the minimum energy

is the true ground-state electron density. Kohn and Sham [21] then proposed a set of self-consistent one-electron equations,

$$\left[\frac{-\hbar^2}{2m} \nabla^2 + V_{ion}(\mathbf{r}) + V_H(\mathbf{r}) + V_{XC}(\mathbf{r}) \right] \psi_i(\mathbf{r}) = \varepsilon_i \psi_i(\mathbf{r}) \quad (1.1)$$

where ψ_i is the wave function of electronic state i , and ε_i is the eigenvalue. The Kohn-Sham equation recasts the interacting many-body electron system into an equivalent system of non-interacting electrons in an effective potential that arises from the interaction of all the other electrons and nuclei. The effective potential includes the static total ion-electron potential V_{ion} , the Hartree potential V_H and the exchange-correlation (XC) [22] potential V_{XC} . The effective potential, however, cannot be evaluated exactly as the electron exchange and correlation energy functional is unknown. Various different approximations have been developed to approximate the exchange and correlation functional, which have increased over the years in sophistication and accuracy. The most basic approximation involves assuming that the XC energy functional depends solely upon the electronic density and is known as the local density approximation (LDA) [21]. This was subsequently improved via the development of the generalized gradient approximation (GGA) [23] which further takes into account the gradient of the electronic density. These methods have been rather successful in simulating the physical properties (such as lattice parameter, band gap, elastic constants and bulk modulus, etc.) for a number of systems. These approximations are, however, not always appropriate and break down in some cases; it is well known that for strongly correlated electron materials (SCEMs) such as $3d$ transition-metal oxides LDA and GGA both fail to give correct descriptions of bulk physical properties [24].

Conventional DFT adopts homogeneous-electron-gas framework to construct the local density approximation [25]. In systems with narrow d - or f - bands and localized orbitals, however, one can no longer assume that these electron interactions are weak compared to the bandwidth [24]. In order to address the on-site strong Coulomb repulsion in the localized d - or f - orbitals of transition metal and rare earth compounds, Anisimov et al. [24, 26] added a Hubbard-type [27] term to the DFT energy functional. In the simplified rotationally invariant approach developed by Dudarev et al. [28], the DFT+U energy functional can be expressed as

$$E^{DFT+U} = E^{DFT} + \frac{\bar{U} - \bar{J}}{2} \sum_{\sigma} \left[\text{Tr} \rho^{\sigma} - \text{Tr} (\rho^{\sigma} \rho^{\sigma}) \right] \quad (1.2)$$

where \bar{U} is the Hubbard parameter that describes the increase in the coulomb energy required to localize two electrons on the same atomic site, \bar{J} is the screened Stoner-like parameter, measuring the intra-atomic electron exchange energy, and ρ is the on-site electron density matrix.

1.2.2 Bloch's theorem and supercell approach

There are effectively an infinite number of electrons within a solid. However for a solid with perfect periodicity, it is only necessary to consider a finite number of electrons within a unit cell. Bloch's theorem [29] states that, within a periodic solid, the wave function of each electronic state i can be written as the product of a part with wavelike properties $\exp(i\mathbf{k}\cdot\mathbf{r})$ and a part with periodicity of the unit cell $u_i(\mathbf{r})$:

$$\psi_{i,\mathbf{k}}(\mathbf{r}) = \exp(i\mathbf{k}\cdot\mathbf{r})u_i(\mathbf{r}) \quad (1.3)$$

where \mathbf{k} is a wave vector confined to the first Brillouin zone (Wigner-Seitz primitive cell in reciprocal space). The cell-periodic part can be expanded in terms of Fourier series,

$$u_i(\mathbf{r}) = \sum_{\mathbf{G}} c_{i,\mathbf{G}} \exp(i\mathbf{G}\cdot\mathbf{r}) \quad (1.4)$$

where \mathbf{G} are reciprocal lattice vectors of the crystal defined by $\mathbf{G}\cdot\mathbf{R} = 2\pi m$ for all lattice vector \mathbf{R} of the crystal in real space where m is an integer. Therefore each electronic wave function can be written as a linear combination of plane waves,

$$\psi_{i,\mathbf{k}}(\mathbf{r}) = \sum_{\mathbf{G}} c_{i,\mathbf{k}+\mathbf{G}} \exp[i(\mathbf{k} + \mathbf{G})\cdot\mathbf{r}] \quad (1.5)$$

Bloch's theorem can also be applied to non-periodic systems, such as molecules, clusters, surfaces, defects etc., a supercell with sufficiently large vacuum region needs to be used so that the interaction between repeated images are negligible.

1.2.3 Brillouin zone sampling

Because of periodic boundary condition, Bloch wave vectors \mathbf{k} are only allowed by the form

$$\mathbf{k} = \sum_{i=1}^3 \frac{m_i}{N_i} \mathbf{g}_i \quad (1.6)$$

where \mathbf{g}_i are the reciprocal lattice unit vectors, N_i are numbers of cells along the real lattice vector and m_i are integers [30]. There are effectively an infinite number of \mathbf{k} -points. The Bloch's theorem transforms the problem of calculating infinite number of electronic wave functions to the problem of calculating finite number of electronic wave functions at infinite number of \mathbf{k} -points. However the electronic wave functions at \mathbf{k} -points that are very close to one another are almost identical. Therefore the electron wave functions at a single \mathbf{k} -point can represent those over a region in the \mathbf{k} -space. For example, the Monkhorst-Pack scheme [31] homogeneously samples \mathbf{k} -points in the Brillouin zone.

1.2.4 Plane wave basis set and pseudopotential approximation

In principle, an infinite discrete plane wave basis set is required to expand the electronic wave function at each \mathbf{k} -point. In practice, only a finite number of plane waves with kinetic energy $\frac{\hbar^2}{2m}|\mathbf{k} + \mathbf{G}|^2$ less than a chosen cutoff energy are included in the basis set, because the calculated total energy converges with increasing kinetic energy cutoff [30]. However, it's still too computationally expensive to perform an all electron calculation, as it would require an incalculable number of plane waves to expand the wave functions of tightly bound electrons in the core region. By using a pseudopotential [32] to replace the core electrons and the strong ionic potential, the electronic wave functions can be expanded with a significantly smaller plane wave basis set.

1.2.5 Transition state theory

Eyring [33], Evans and Polanyi's [34] transition state theory describes the reaction rates of elementary reactions by making the following assumptions [35], (1) reactant molecules are distributed according to the Maxwell-Boltzmann laws; (2) reaction trajectories do not recross the transition state and transition states are in quasi-equilibrium with reactants; (3) the motion along the reaction coordinate of the activated complex can be separated from the other motions and treated classically as a translation. The rate constant for the elementary reaction:



where R_i , X^\ddagger and P are the reactant, transition and product states, the rate constant can be written as:

$$k = \frac{k_B T}{h} \frac{Q_{X^\ddagger}}{Q_{R_1} Q_{R_2}} \exp(-E^\ddagger/k_B T) \quad (1.8)$$

where Q_{X^\ddagger} is the equilibrium partition function per unit volume for the transition state, Q_{R_i} is the partition function for reactant, E^\ddagger is the energy difference between the lowest level of transition state and the lowest level of reactants, k_B is the Boltzmann constant.

1.3 Overview of chapters

This dissertation, beyond the introduction and the conclusion, is organized into 4 other chapters. Chapter 2 introduces the dehydrogenation of propane over sub-nanometer metal clusters and discusses structure-reactivity relationships that can be used to understand and predict C-H bond activation energies over sub-nanometer sized Pt_n and Co_n clusters. Chapter 3 examines the catalytic dehydrogenation of cyclohexane over Pt nanoparticles. An extensive set of first-principles DFT calculations are carried out to examine the Pt particle size effects on the elementary steps that control the successive dehydrogenation of cyclohexane and the desorption of the unsaturated products. Rigorous kinetic analyses are carried out and used to explain the experimentally observed size-dependent selectivity. Chapter 4 extends the catalytic dehydrogenation studies to include oxidative dehydrogenation and examines the unique reactivity of Au/ Co_3O_4 in the oxidative dehydrogenation of cyclohexane. In Chapter 5, we examine the mechanisms that control the catalytic cracking of model hydrocarbons on solid acid catalysts in order to begin to develop structure-reactivity relationships that can describe the structure and composition of the solid acid catalysts and their influence on the acidity and cracking activity as well as the influence of reactant structure on its cracking behavior.

References

1. W.H. Heiser, D.T. Pratt, D.H. Daley, and U.B. Mehta, *Hypersonic Airbreathing Propulsion*. 1994, AIAA, Inc.: Washington, DC.
2. C. Segal, *The Scramjet Engine: Processes and Characteristics*. 2009, New York: Cambridge University Press.
3. H. Lander and A.C. Nixon, *Endothermic fuels for hypersonic vehicles*. *Journal of Aircraft*, 1971. **8**(4): p. 200-207.
4. D.R. Sobel and L.J. Spadaccini, *Hydrocarbon fuel cooling technologies for advanced propulsion*. *Journal of Engineering for Gas Turbines and Power*, 1997. **119**(2): p. 344-351.
5. L. Maurice, T. Edwards, and J. Griffiths, *Liquid Hydrocarbon Fuels for Hypersonic Propulsion*, in *Scramjet Propulsion*, E.T. Curran and S.N.B. Murthy, Editors. 2000, AIAA: Reston, VA. p. 757-822.
6. H. Huang, L.J. Spadaccini, and D.R. Sobel, *Fuel-Cooled Thermal Management for Advanced Aeroengines*. *Journal of Engineering for Gas Turbines and Power*, 2004. **126**(2): p. 284-293.
7. J.J. Lipinski and C. White. *Testing of an Endothermic Heat Exchanger/Reactor for a Mach 4 Turbojet*. in *JANNAF Propulsion Meeting (CPIA Publication 580)*. 1992. CPIA.
8. R.W. Johnson, W.C. Zackro, D. Germanas, and S. Keenan. *Development of High Density Endothermic Fuel Systems*. in *JANNAF Propulsion Meeting (CPIA Publication 580)*. 1992. CPIA.
9. B.M. Fabuss, J.O. Smith, R.I. Lait, A.S. Borsanyi, and C.N. Satterfield, *Rapid Thermal Cracking of n-Hexadecane at Elevated Pressures*. *Industrial & Engineering Chemistry Process Design and Development*, 1962. **1**(4): p. 293-299.
10. B.M. Fabuss, J.O. Smith, R.I. Lait, M.A. Fabuss, and C.N. Satterfield, *Kinetics of Thermal Cracking of Paraffinic and Naphthenic Fuels at Elevated Pressures*. *Industrial & Engineering Chemistry Process Design and Development*, 1964. **3**(1): p. 33-37.
11. X.J. Fan, F.Q. Zhong, G. Yu, J.G. Li, and C.J. Sung, *Catalytic Cracking and Heat Sink Capacity of Aviation Kerosene under Supercritical Conditions*. *Journal of Propulsion and Power*, 2009. **25**(6): p. 1226-1232.
12. D.L. Trimm, *Catalytic combustion (review)*. *Applied Catalysis*, 1983. **7**(3): p. 249-282.
13. J. Saint-Just and J. der Kinderen, *Catalytic combustion: from reaction mechanism to commercial applications*. *Catalysis Today*, 1996. **29**(1-4): p. 387-395.
14. R.A. Dalla Betta and T. Rostrup-Nielsen, *Application of catalytic combustion to a 1.5 MW industrial gas turbine*. *Catalysis Today*, 1999. **47**(1-4): p. 369-375.
15. D. Anson, M. Decorso, and W.P. Parks, *Catalytic combustion for industrial gas turbines*. *International Journal of Energy Research*, 1996. **20**(8): p. 693-711.
16. Z.R. Ismagilov and M.A. Kerzhentsev, *Catalytic Fuel Combustion - A Way of Reducing Emission of Nitrogen Oxides*. *Catalysis Reviews: Science and Engineering*, 1990. **32**(1): p. 51 - 103.
17. C. Møller and M.S. Plesset, *Note on an Approximation Treatment for Many-Electron Systems*. *Physical Review*, 1934. **46**(7): p. 618-622.
18. J. Čížek, *On the Correlation Problem in Atomic and Molecular Systems. Calculation of Wavefunction Components in Ursell-Type Expansion Using Quantum-Field Theoretical Methods*. *The Journal of Chemical Physics*, 1966. **45**(11): p. 4256-4266.
19. M. Born and J.R. Oppenheimer, *Zur Quantentheorie der Moleküln*. *Annalen der Physik*, 1927(84): p. 458.
20. P. Hohenberg and W. Kohn, *Inhomogeneous Electron Gas*. *Physical Review*, 1964. **136**(3B): p. B864.
21. W. Kohn and L.J. Sham, *Self-Consistent Equations Including Exchange and Correlation Effects*. *Physical Review*, 1965. **140**(4A): p. A1133.
22. A.L. Fetter and J.D. Walecka, *Quantum theory of many-particle systems*. 1971, New York: McGraw-Hill.
23. J.P. Perdew and W. Yue, *Accurate and simple density functional for the electronic exchange energy: Generalized gradient approximation*. *Physical Review B*, 1986. **33**(12): p. 8800.
24. V.I. Anisimov, J. Zaanen, and O.K. Andersen, *Band theory and Mott insulators: Hubbard U instead of Stoner I*. *Physical Review B*, 1991. **44**(3): p. 943.
25. D.M. Ceperley and B.J. Alder, *Ground State of the Electron Gas by a Stochastic Method*. *Physical Review Letters*, 1980. **45**(7): p. 566.

26. Vladimir I Anisimov, F Aryasetiawan, and A.I. Lichtenstein, *First-principles calculations of the electronic structure and spectra of strongly correlated systems: the LDA+ U method* Journal of Physics: Condensed Matter, 1997. **9**(4).
27. J. Hubbard. *Electron Correlations in Narrow Energy Bands*. in *Proceedings of the Royal Society of London*. 1963. The Royal Society.
28. S.L. Dudarev, G.A. Botton, S.Y. Savrasov, C.J. Humphreys, and A.P. Sutton, *Electron-energy-loss spectra and the structural stability of nickel oxide: An LSDA+U study*. Physical Review B, 1998. **57**(3): p. 1505.
29. N.W. Ashcroft and N.D. Mermin, *Solid State Physics*. 1976, Philadelphia: W. B. Saunders.
30. M.C. Payne, M.P. Teter, D.C. Allan, T.A. Arias, and J.D. Joannopoulos, *Iterative minimization techniques for ab initio total-energy calculations: molecular dynamics and conjugate gradients*. Reviews of Modern Physics, 1992. **64**(4): p. 1045-1097.
31. H.J. Monkhorst and J.D. Pack, *Special points for Brillouin-zone integrations*. Physical Review B, 1976. **13**(12): p. 5188-5192.
32. J.C. Phillips, *Energy-Band Interpolation Scheme Based on a Pseudopotential*. Physical Review, 1958. **112**(3): p. 685-695.
33. H. Eyring, *The Activated Complex in Chemical Reactions*. The Journal of Chemical Physics, 1935. **3**(2): p. 107-115.
34. M.G. Evans and M. Polanyi, *Some applications of the transition state method to the calculation of reaction velocities, especially in solution*. Transactions of the Faraday Society, 1935. **31**(0): p. 875-894.
35. J.I. Steinfeld, J.S. Francisco, and W.L. Hase, *Statistical Approach to Reaction Dynamics: Transition State Theory*, in *Chemical Kinetics and Dynamics*. 1998, Prentice Hall: Upper Saddle River, New Jersey. p. 287.

Chapter 2 Propane Dehydrogenation on Pt and Co sub-nm clusters

2.1 Introduction

As discussed in Chapter 1, the regenerative cooling of jet engines [1] involves endothermic reactions of jet fuels, such as dehydrogenation and cracking of hydrocarbons. The catalytic dehydrogenation of propane is an important reaction as it serves as an invaluable surrogate model reaction for the dehydrogenation of other alkanes with higher molecular weights that constitute hydrocarbons fuels. The dehydrogenation of propane to propylene is also an important commercial process since propylene is used as a feedstock in the production of a wide range of products. In 2010, a total of 14.3 million tons of propylene were produced in the US and 80 million tons worldwide; about 65% of the propylene global production were used to make polypropylene, the rest were used to produce chemical intermediates (epoxypropane, propenal, cumene, etc.) and solvents (acetone, butanol, etc.) [2]. While propylene is predominantly produced by steam cracking of naphtha (56%) and from off-gases produced in fluid catalytic cracking (33%) [2, 3], dehydrogenation of propane to propylene has gained significantly increasing attention from chemical companies, as the propane price decreases with the expanding exploitation of shale oil and gas [4].

The catalytic dehydrogenation of alkanes is carried out commercially over supported Pt catalysts [5], such as in the Oleflex process [6] developed by UOP. Earth-abundant metals, such as Ni and Co, are being studied as potential cheaper substitutes to these precious metals [7], especially for the potential application as jet fuel additives which are not reusable and will eventually be emitted with the exhaust gas. Metal oxide supported Co

catalysts have shown catalytic activity for methane activation in CH₄/CO₂ reforming reactions [8-11]. In this work, propane serves as a simplified hydrocarbon fuel surrogate to probe the mechanism of catalytic activation and dehydrogenation of hydrocarbons, and we will focus on Pt and Co catalysts.

Sub-nanometer clusters are known to exhibit pronounced variations in their chemical properties as the size and geometry are varied [12], which is typically described as finite or quantum size effects. Extensive experimental studies have been carried out to explore catalytic properties of both freestanding [13] as well as supported [14] metal clusters in this “non-scalable” size regime. Clusters with specific atomic counts and structures can be created either via the chemical synthesis using ligand-stabilized clusters [15] or via high-frequency laser evaporation methods [16]. Catalytic kinetic analyses carried out over these well-controlled clusters can be directly compared with theoretical calculations. The size-dependent properties and catalytic reactivity can only be partially explained by structural properties such as the metal coordination number, and electronic descriptors such as frontier orbitals [17] and the d-band center [18, 19]. Herein, we provide a more detailed analysis of both Pt_n and Co_n clusters in order to explain the catalytic reactivity on different sizes of clusters.

The chemical properties along with the catalytic behavior of these free-standing metal clusters can markedly change if they are deposited onto catalytic supports. Carbon nanotubes (CNT) are considered promising catalyst support materials as they offer large surface areas, exceptional mechanical stability and rich functionalization opportunities [20-

23]. In this work, we will examine the metal-support interactions and catalytic activity of Pt_5 on different diameter CNTs in order to understand the influence of CNT size on their electronic properties and catalytic activities of the Pt_5 clusters.

2.2 Method

All the calculations reported herein were carried out using periodic plane-wave density functional theory (DFT) [24, 25], as implemented in the Vienna *ab initio* Simulation Package (VASP) [26-29]. The spin polarized generalized gradient approximation (SGGA), in the form of Perdew-Burke-Ernzerhof (PBE) [30, 31] was used to model electronic exchange and correlation effects. The interactions between valence and the core electrons were described with the projector augmented wave method (PAW) [32, 33]. The wave functions are expanded in a plane wave basis set with a kinetic energy cut-off of 400 eV. The electronic energies were converged to within 10^{-6} eV. All of the geometric structures for reactants, intermediates, products were converged to a point where the displacement forces on each of atoms in the unit cell were converged to within 0.05 eV/Å. Transition states were located by using a combination of the climbing image nudged elastic band (CI-NEB) [34, 35] method and the dimer method [36] and also converged to within 0.05 eV/Å.

The initial structures of small metal clusters were first determined by using structural Monte Carlo methods [37] previously developed in our laboratory, which uses Embedded-Atom Method (EAM) [38] potentials to calculate the energies. The structures obtained from the structural Monte Carlo simulations were further optimized with DFT calculations discussed above. A cubic unit cell with the lattice parameter $a = 16 \text{ \AA}$, was found to be large enough to prevent any electronic interactions between the metal cluster and its periodic images. The Brillouin zone was sampled using a single Γ -point.

The 5-atom Platinum cluster (Pt_5) was used to examine the influence of carbon nanotube support. Four different sizes of single walled carbon nanotubes were used as supporting materials, including CNT(4,0), CNT(6,0), CNT(8,0), and CNT(12,0). The one-dimensional nanotube was simulated with infinite length. We used the tetragonal unit cell with the dimensions $a = 20 \text{ \AA}$, $b = 20 \text{ \AA}$, and $c = 12.7 \text{ \AA}$ (the c lattice is aligned with the axis of the nanotube), which were found to be large enough to prevent electronic interactions between the metal-nanotube composite and its periodic images. A $1 \times 1 \times 6$ Monkhorst–Pack [39] \mathbf{k} -point mesh was used to sample the first Brillouin zone. The \mathbf{k} -point sampling was found to be sufficient to ensure convergence of the structure and energy.

In order to tie the electronic properties of the metal cluster to their reactivity we examine both the highest occupied molecular orbital (HOMO) as well as the lowest unoccupied molecular orbital (LUMO) for each cluster as they provide a measure of the ability of the cluster to donate or accept electrons, respectively. In a simplified molecular orbital theory approach, the ionization potential (IP) is related to the energy of the highest occupied molecular orbital (HOMO) by Koopmanns' theorem [40] and the electron affinity (EA) is related to the energy of the lowest unoccupied molecular orbital (LUMO) [41]. The energies of the ionic states (M^+ and M^-) for each metal cluster M were calculated by starting with optimized structures of the charge neutral clusters. Dipole and quadrupole moments were calculated to correct the leading errors in total energy calculations of charged systems [42, 43] resulted from spurious interactions induced by the periodic boundary conditions. The ionization potentials (IP) and electron affinities (EA) were calculated from the DFT energies via Eqns. (2.1) and (2.2), respectively.

$$IP = E(M^+) - E(M) \quad (2.1)$$

$$EA = E(M) - E(M^-) \quad (2.2)$$

Smaller values of the IP indicate that less energy is required for ionization, and a larger EA indicates that more energy is released upon the addition of an electron. The chemical hardness, η , often provides some insights into a molecule's reactivity as it is related to the energy difference between the HOMO and the LUMO (HOMO-LUMO gap) [44]. The chemical hardness was calculated herein as $\eta = IP - EA$ based on the commonly used finite difference approximation [41].

The apparent activation barriers reported herein were calculated as the difference in energy between the transition state and the sum of the energies of separated reactants,

$$E_{\text{apparent_barrier}} = E^\ddagger - E_{\text{catalyst}} - E_{\text{propane}} \quad (2.3)$$

As such the apparent barriers for dissociative adsorption reactions can be negative in the case of strong adsorption of the reactants and relatively low intrinsic activation barrier. The intrinsic barrier is calculated as the energy difference between the transition state and reactant state,

$$E_{\text{intrinsic_barrier}} = E^\ddagger - E_R \quad (2.4)$$

2.3 Results and Discussion

2.3.1 Propane activation on bare Pt_n and Co_n clusters

In the sub-nanometer size regime, the catalytic activity of metal clusters can vary significantly with the number of atoms in the cluster. Previous experimental studies of gas phase reactivity of methane over neutral Pt_n ($n \leq 24$) clusters in a fast flow reactor showed an overall decrease in the reactivity of methane with increasing cluster size, with a dramatic drop in reactivity starting at Pt_6 and a jump to higher reactivity at Pt_{11-12} [45]. Similar studies were carried out for the dissociative adsorption of D_2 as the D-D bond is thought to behave similarly to a C-H bond, over a range of different Co clusters up to 28 atoms (Co_n ($n \leq 28$)) in a fast flow reactor. The results showed a minimum reactivity at Co_6 and a maximum reactivity at Co_{16} with a nearly monotonic increase between $n=6$ to $n=13$ [46].

DFT calculations were carried out herein to examine the activation of the secondary C-H bond of propane at different sites of sub-nanometer Pt_n ($n=4-9,13$) (as in Figure 2.1) and Co_n ($n=5-14$) (as in Figures 2.2 and 2.3) clusters. Within the studied size range, Pt_n clusters were found to have a much higher activity than Co_n clusters for propane activation. And in general, the C-H bond activation barriers are lower at less coordinatively saturated metal sites, with the exception of Pt_5 and Co_7 clusters. The reason for these exceptions and outliers will be discussed later in Section 2.3.2. For Pt_n clusters with the size of 4 to 9 atoms (Figure 2.4), the C-H activation barrier increases with the increasing size of the cluster, which is consistent with the experimental results that show a decrease in methane activity with increased Pt cluster size [45]. For Co_n clusters with a size of 6 to 13 atoms (Figure 2.5), the C-H bond activation barrier decreases monotonically with the increase in size,

which is also in agreement with experimental results for D_2 activation over Co_n clusters [46].

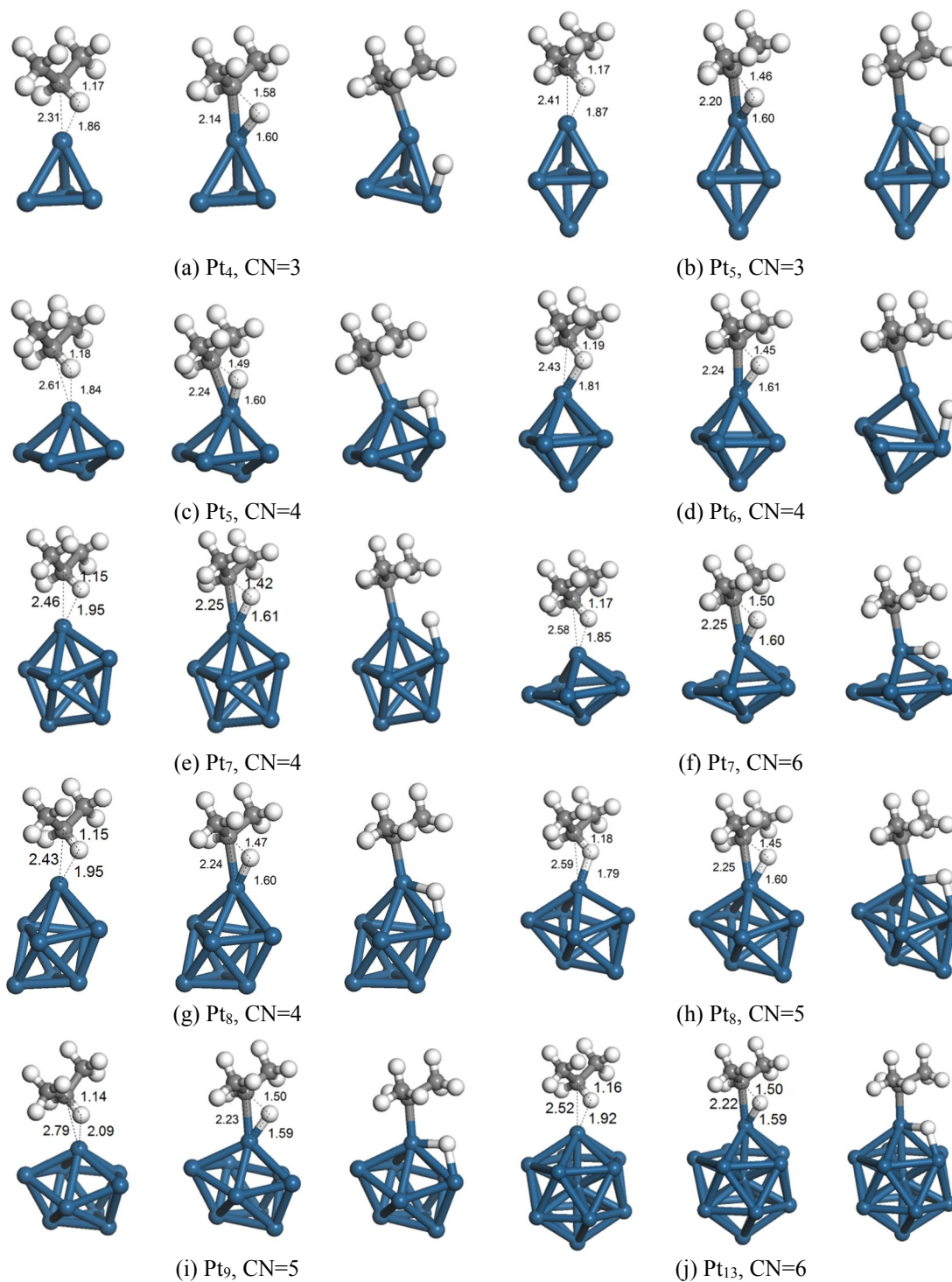


Figure 2.1 DFT-calculated reactant, transition, and product states for the activation of the secondary C-H bond of propane at metal sites with different coordination numbers (CN) on a variety of Pt_n ($n=4\sim 9, 13$) clusters.

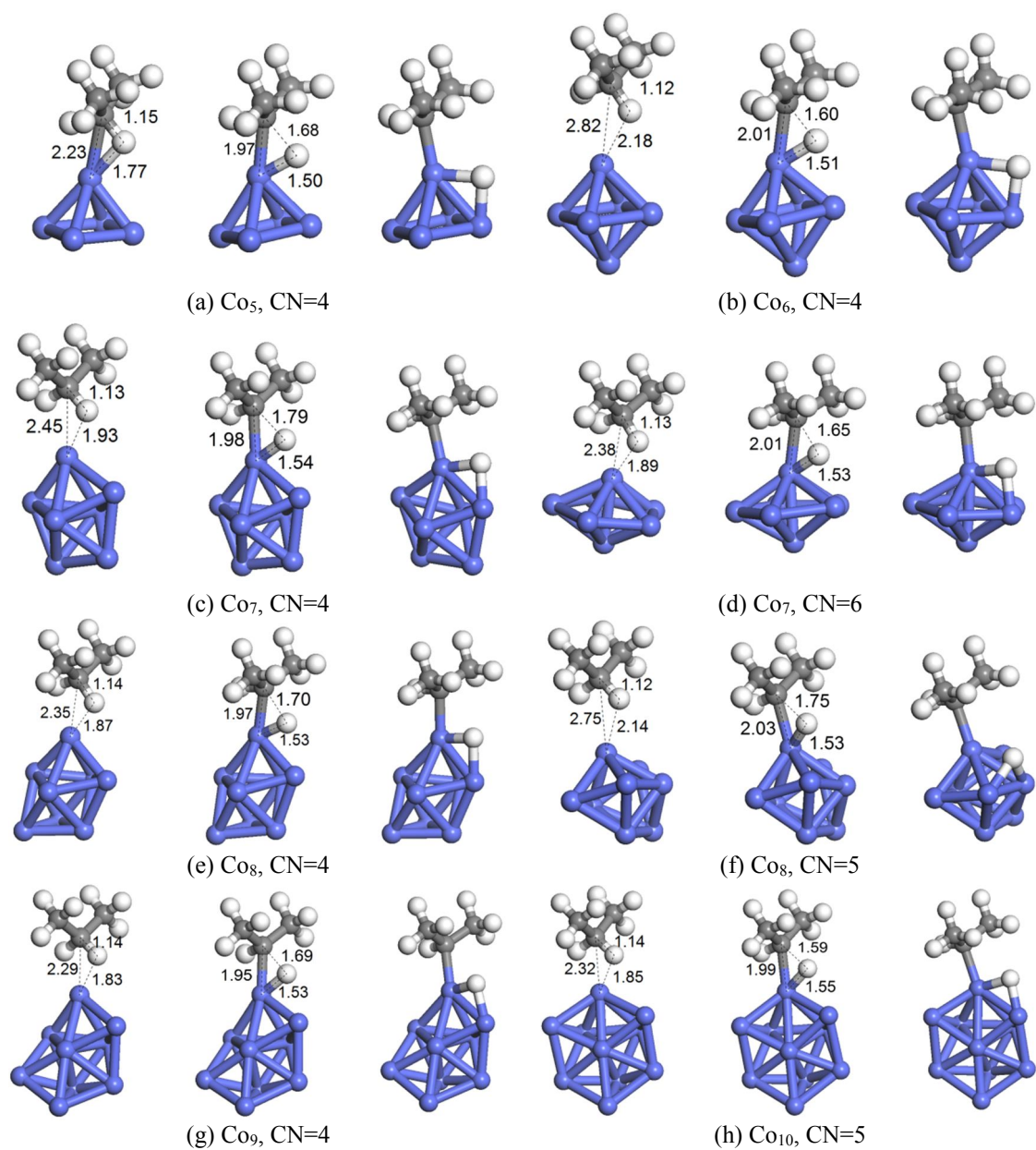


Figure 2.2 DFT-calculated reactant, transition, and product states for the activation of the secondary C-H bond of propane at metal sites with different coordination numbers (CN) on a variety of Co_n ($n=5\sim 10$) clusters.

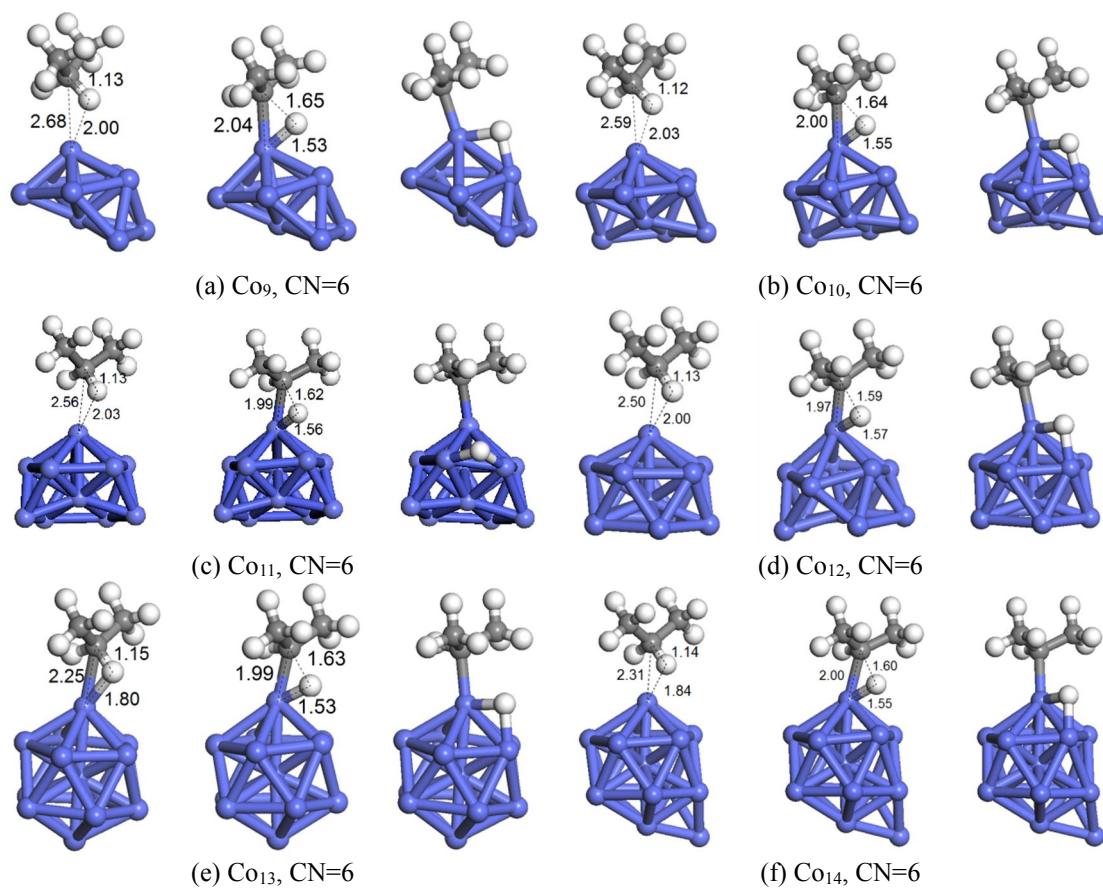


Figure 2.3 DFT-calculated reactant, transition, and product states for the activation of the secondary C-H bond of propane at metal sites with a coordination number (CN) = 6 on a variety of Co_n (n=9~14) clusters.

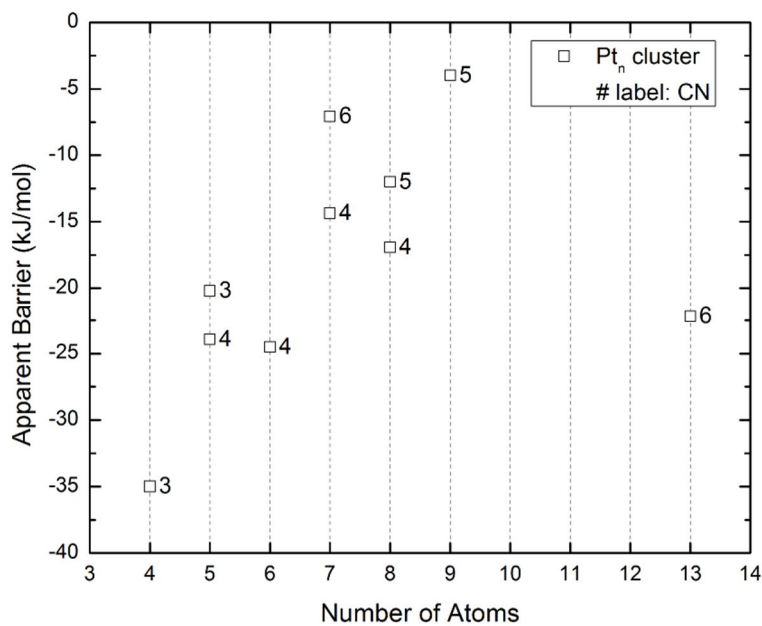


Figure 2.4 DFT-calculated apparent activation barrier for the activation of the secondary C-H bond of propane at metal sites with different coordination numbers (labeled besides hollow square) on Pt_n (n=4~9,13) clusters.

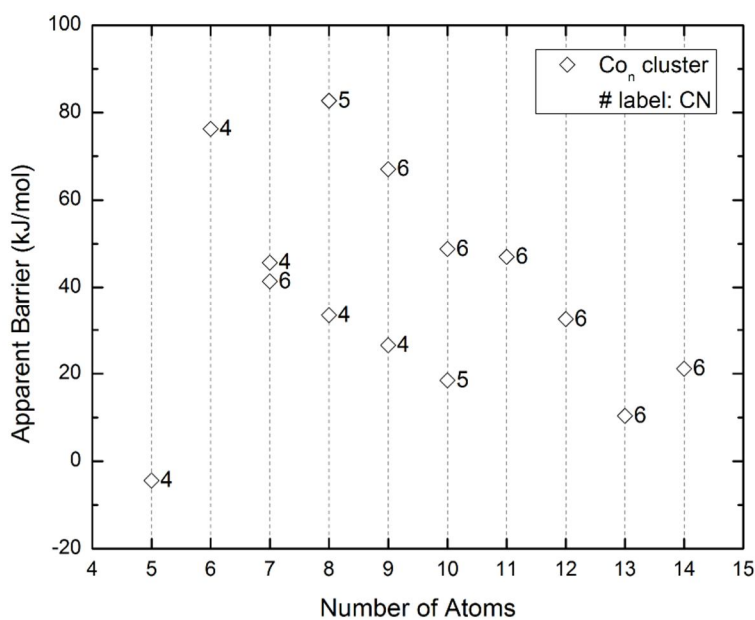


Figure 2.5 DFT-calculated apparent energy barrier for the activation of the secondary C-H bond of propane activation at metal sites with different coordination numbers (labeled besides hollow diamond) on Co_n (n=5~14) clusters.

2.3.2 Charge analyses

In order to understand the reactivity trends over the Pt_n and Co_n clusters, we carried out more detailed electronic structure analyses. Bader [47, 48] charge analyses were performed to calculate the initial charges on the metal sites where the reaction proceeds, the changes in the charges on the atoms directly involved in the reaction from reactant state to the transition state and the charge transfer between the metal cluster and propane (Table 2.1). The initial charges on the metal site of the Pt_n and Co_n clusters where reaction proceeds are predominantly neutral; some sites have a very small ($< 0.15e$) net charge due to their special coordination environment. The C-H bond activation of propane occurs more readily on Pt_n than on Co_n . The reaction proceeds via oxidative addition [49] with a metal Pt atom insertion into the secondary C-H bond of propane. This elementary step has an early transition state. A negative charge is transferred from the C-H bond to metal d-states in Pt_n in the transition state of C-H activation and the hydrogen picks up a slight positive charge. The reaction on Co_n clusters, on the other hand, has a late transition state as the electron is transferred from Co_n to propane; there is a back-donation of electrons into the C-H antibonding which ultimately results in negative charge on the H which becomes hydridic. This indicates that although the geometric structure of the transition states look similar, the electronic details in the mechanism of propane C-H bond activation are different for Pt_n and Co_n clusters.

A closer monitoring of net charges along the reaction path of propane C-H bond activation at a 4-coordinated metal site of Pt_6 and Co_6 reveals the significant distinction in charge transfer between these two metal clusters (Figure 2.6). Upon adsorption of propane, the Pt_6

cluster picks up a 0.13 e negative charge. There is a small transfer of charge from the Pt cluster to propane as the C-H bond is activated. As the C-H bond breaks, Pt-C and Pt-H bonds form and the Pt cluster transfers -0.14 e to the resulting propyl and hydride surface fragments that form. This is consistent with the current understanding in organometallic literature that late transition metal complexes are dominated by electrophilic reaction profiles [50]. The charge transfer from the cluster to the propyl and hydride fragments appears to occur rather late along the reaction channel.

In contrast to the adsorption and activation of propane on Pt₆, there is only a negligible amount of charge that is transferred from propane to the Co₆ cluster before the C-H bond is activated. Upon the activation of the C-H bond, the Co cluster transfers -0.13 e to the propane in the transition state. The Co cluster transfers additional charge as the reaction proceeds and ultimately reaches a net positive charge of +0.44 e as the propyl and hydride fragments that form pick up about -0.22 e each. This is in agreement with the $4s^23d^7$ electronic configuration of cobalt that Co preferentially donates electrons to form half-filled d-states.

We calculated ionization potential, electron affinity, and chemical hardness of these Pt and Co metal clusters (Table 2.2). Our calculations indicate that the Pt_n clusters have a higher electron affinity than the Co_n clusters. The Co_n clusters, on the other hand, are more readily ionized than the Pt_n clusters. In the plot of intrinsic propane activation barrier against chemical hardness ($\eta = IP - EA$), which is a measure of the HOMO-LUMO gap, we found a direct correlation between the two as shown in Figure 2.7. This may be expected as a

lower LUMO or a higher HOMO of the metal cluster would enhance more charge transfer from the C-H bond to the cluster and the back-donation of charge in the cluster to the antibonding C-H bond on propane thus resulting in a smaller energy gap and lower activation energy for the activation of the C-H bond to the metal cluster [51]. Pt₄, Pt₁₃, Co₅, and Co₇ were recognized as outliers in the correlation between intrinsic C-H activation barriers and chemical hardness properties of metal clusters. Pt₄ (tetrahedron) and Pt₁₃ (icosahedron) adopt stable geometric structures and are known as “magic number clusters” [52] which usually have lower chemical activity than non-magic clusters. On the other hand, the 4-coordinated site on Co₅ and the 6-coordinated site on Co₇ are found to be more active than usual. The reason behind this is still unclear, we speculate that it could be caused by the formation of some specific “magnetic magic number clusters” [53, 54], which is an interesting topic for future research.

Table 2.1 Summary of activation barrier and Bader charge analyses for propane activation over different bare Pt_n and Co_n clusters. (CN represents the coordination number at the reaction site)

	Propane C-H Bond		Charge on the Reaction Site of Bare Metal Cluster (e)	Change of Charge $\Delta\rho = \rho_{TS} - \rho_R$ (e)			
	Apparent Activation Barrier (kJ mol ⁻¹)	Intrinsic Activation Barrier (kJ mol ⁻¹)		Whole Metal Cluster	Reaction Site on Cluster	C	H
Pt ₄ , CN=3	-35.0	24.0	-0.035	-0.104	0.052	-0.107	0.030
Pt ₅ , CN=3	-20.2	13.0	-0.125	-0.113	0.086	-0.101	0.039
Pt ₅ , CN=4	-23.9	16.2	0.084	-0.098	0.047	-0.121	0.019
Pt ₆ , CN=4	-24.5	15.0	0.001	-0.128	0.016	-0.073	0.026
Pt ₇ , CN=4	-14.4	10.7	-0.037	-0.124	0.019	-0.125	0.033
Pt ₇ , CN=5	-7.1	19.0	0.109	-0.117	-0.032	-0.085	0.045
Pt ₈ , CN=4	-16.9	9.5	-0.040	-0.112	0.035	-0.105	0.032
Pt ₈ , CN=5	-12.0	13.2	0.045	-0.149	-0.003	-0.095	0.048
Pt ₉ , CN=5	-4.0	8.5	0.009	-0.143	0.035	-0.104	0.050
Pt ₁₃ , CN=6	-22.2	22.4	-0.034	-0.147	0.035	-0.121	0.054
Co ₅ , CN=4	-4.4	48.5	0.046	0.161	0.191	-0.167	-0.083
Co ₆ , CN=4	76.3	86.2	-0.002	0.134	0.164	-0.188	-0.071
Co ₇ , CN=4	45.7	69.2	-0.015	0.214	0.229	-0.173	-0.140
Co ₇ , CN=6	41.4	59.4	0.030	0.168	0.182	-0.151	-0.085
Co ₈ , CN=4	33.4	58.8	-0.040	0.181	0.206	-0.185	-0.112
Co ₈ , CN=5	82.8	90.9	0.042	0.223	0.183	-0.170	-0.118
Co ₉ , CN=4	26.5	56.8	-0.009	0.179	0.177	-0.115	-0.114
Co ₉ , CN=6	67.1	77.9	0.032	0.211	0.194	-0.185	-0.097
Co ₁₀ , CN=5	18.5	61.6	0.002	0.176	0.179	-0.173	-0.113
Co ₁₀ , CN=6	48.8	41.9	0.014	0.177	0.186	-0.222	-0.108
Co ₁₁ , CN=6	47.0	78.7	-0.003	0.175	0.190	-0.197	-0.112
Co ₁₂ , CN=6	32.5	58.5	-0.013	0.517	0.214	-0.191	-0.146
Co ₁₃ , CN=6	10.3	50.4	0.000	0.177	0.150	-0.204	-0.107
Co ₁₄ , CN=6	21.2	47.8	0.016	0.174	0.145	-0.163	-0.106

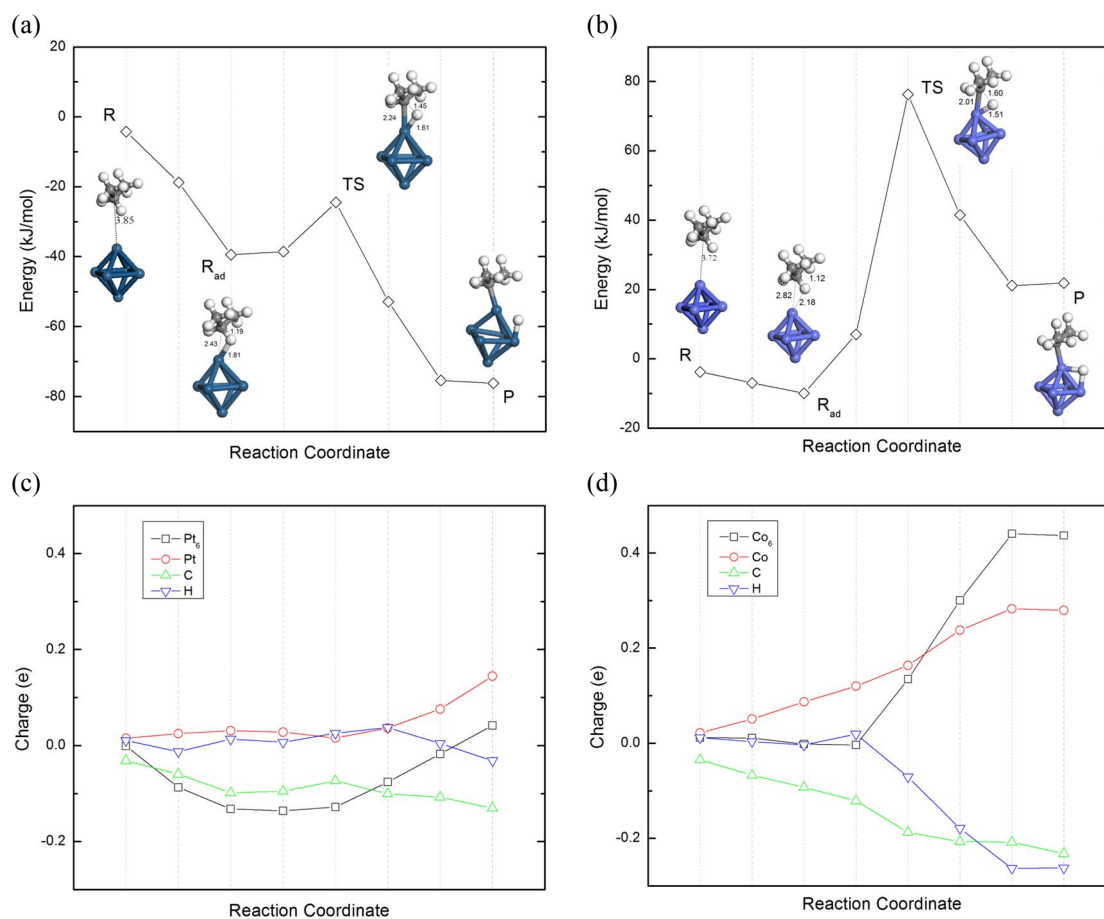


Figure 2.6 Reaction energy profile for the activation of the secondary C-H bond of propane on the 4-coordinate site of Pt₆ cluster (a), and the net Bader charges of Pt₆ cluster (black square), Pt site (red circle), C (green triangle) and H (blue inverted triangle) of corresponding images along the reaction path (c). The reaction energy profile for the activation of the secondary C-H bond of propane on the 4-coordinate site of Co₆ cluster (b), and the net Bader charge of Co₆ cluster (black square), Co site (red circle), C (green triangle) and H (blue inverted triangle) of corresponding images along the reaction path (d).

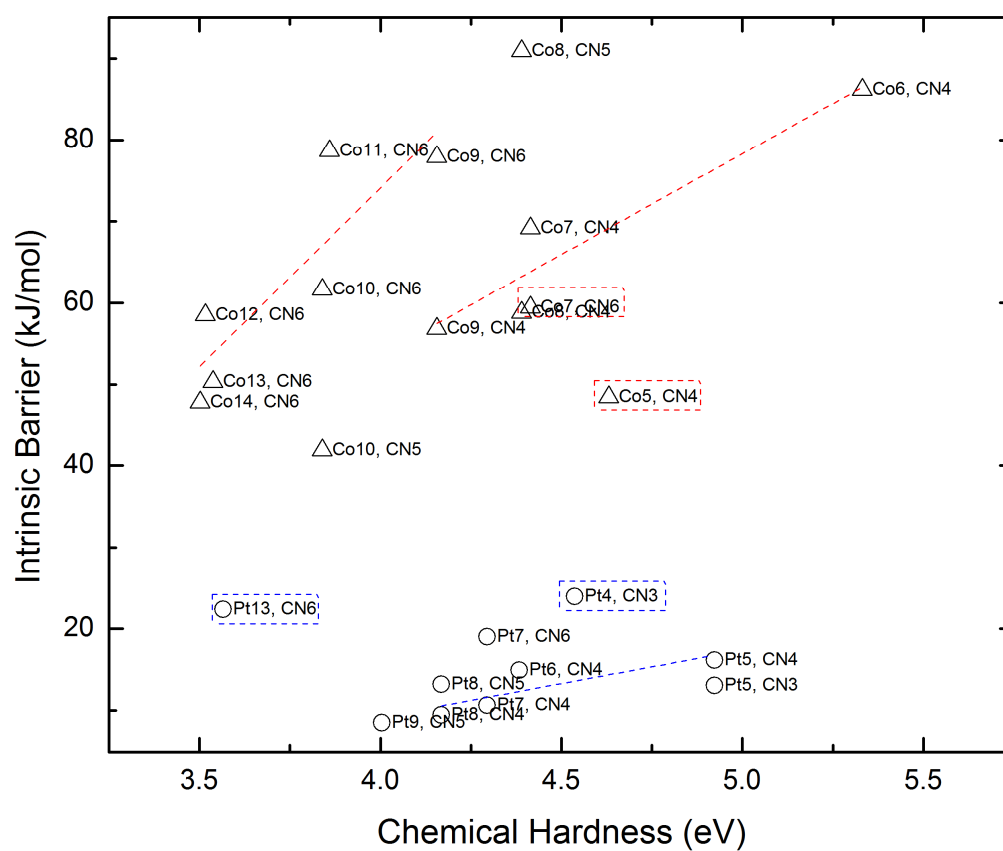


Figure 2.7 Intrinsic propane C-H bond activation barriers vs. chemical hardness. Hollow triangles represent data from Co_n clusters, labeled by cluster size and coordination number at the reaction site. Hollow circles represent data from Pt_n clusters, labeled by cluster size and coordination number at the reaction site. Dashed lines were drawn by fitting data from Pt_n ($n=5,6,7,8$; $\text{CN}=4$), Co_n ($n=6,7,8,9$; $\text{CN}=4$), and Co_n ($n=9, 10, 11, 12, 13, 14$; $\text{CN}=6$). Apparent outliers were enclosed in dashed boxes.

Table 2.2 Ionization potential, electron affinity and chemical hardness of the Pt₄-Pt₁₃ clusters and the Co₅-Co₁₄ clusters.

Metal clusters	IP (eV)	EA (eV)	Hardness (eV)
Pt ₄	6.73	2.19	4.54
Pt ₅	7.28	2.36	4.92
Pt ₆	7.24	2.85	4.38
Pt ₇	6.89	2.60	4.29
Pt ₈	7.02	2.85	4.17
Pt ₉	6.98	2.97	4.00
Pt ₁₃	6.91	3.35	3.57
Co ₅	6.41	1.78	4.63
Co ₆	6.72	1.38	5.33
Co ₇	6.09	1.68	4.41
Co ₈	5.95	1.56	4.39
Co ₉	5.72	1.56	4.16
Co ₁₀	5.59	1.75	3.84
Co ₁₁	5.51	1.65	3.86
Co ₁₂	5.52	2.01	3.52
Co ₁₃	5.43	1.89	3.54
Co ₁₄	5.52	2.02	3.50

2.3.3 Propane Dehydrogenation on CNT supported Pt₅ clusters

Carbon is often used as a support for metal particles in electrocatalysis as well as in other heterogeneous catalyzed reactions due to its ability to stabilize the particles as well as conduct electrons. There has been considerable interest in using single walled carbon nanotubes as support due to their high surface to volume ratios along with unique electronic structures that can be tuned by changing the tube diameter. Herein we probe the influence of the size of the CNT support on the electronic properties and reactivities of Pt₅ clusters. The Pt₅ cluster discussed above were supported on four different sizes of single walled carbon nanotubes. The Pt₅ clusters were found to adsorb most strongly on the CNTs that had the smallest diameter and highest curvatures (Figure 2.8), which is consistent with previous computational results [55]. There is direct electron transfer from the Pt₅ cluster to the CNT upon adsorption which is also consistent with previous results [56]. In addition, we found that the amount of charge that is transferred increases with the increasing curvature of CNT (Figure 2.8). Interestingly, the top atom of the Pt₅ cluster which is not directly bonded to CNT is negatively charged, whereas the Pt₅ cluster as a whole takes on a net positive charge upon adsorption to the CNT (Table 2.3). This charge polarization [57] is thought to be induced by the charge transfer from the Pt cluster to the CNT substrate.

DFT calculations were subsequently carried out to examine the activation of the secondary C-H bond of propane at the top atom of the CNT supported Pt₅ cluster as shown in supplementary Figure 2.11. A Bader charge analysis (Table 2.4) shows that there is an electron transfer from propane to Pt₅-CNT in the transition state for C-H bond activation, thus leading to an increase in electron density on both the Pt₅ cluster as well as the CNT

support. The H appears to be positively charged. The activation energy is much higher than that at the corresponding site (CN=4) on the freestanding Pt₅ cluster. The calculations show that the more negatively charged Pt atom at the top of the cluster leads to a higher apparent C-H activation barrier (see the upper panel of Figure 2.9). This is consistent with experiment findings that anionic Pt_n (n≤21) clusters are less reactive than cationic and neutral Pt_n clusters for methane activation (except Pt₄[±]) [58, 59]. DFT calculations were also carried out for the secondary C-H bond of propane at one of the bottom Pt sites that are bound to the CNT substrate. The C-H bond activation energy at these positively charged bottom Pt sites is much lower than those at negatively charged top Pt sites, but still higher than the C-H activation barrier on the bare Pt₅ cluster (see Tables 2.3 and 2.1). Furthermore, the more positively charged Pt atom at the bottom of the cluster leads to a lower apparent C-H activation barrier as shown in the lower panel of Figure 2.9. In summary, our calculations indicate that CNT supported Pt_n clusters are less active than the freestanding ones and it is viable to tune the reactivity of sub-nanometer Pt_n clusters by changing the diameter of CNT.

Table 2.3 The influence of the diameter of the carbon nanotube support on the apparent activation barriers and charge analyses for the activation of the secondary C-H of propane over the top and bottom Pt sites on the Pt₅-CNT.

	Diameter of CNT (Å)	Pt ₅ Ads. Energy (kJ mol ⁻¹)	Charge on Pt ₅ Cluster (e)	Top Pt site		Bottom Pt site	
				Charge on the Pt site (e)	Propane C-H Act. Barrier (kJ mol ⁻¹)	Charge on the Pt site (e)	Propane C-H Act. Barrier (kJ mol ⁻¹)
Pt ₅ -CNT(4,0)	3.38	-494	0.334	-0.219	32.1	+0.140	-20.2
Pt ₅ -CNT(6,0)	4.85	-342	0.151	-0.240	59.9	+0.094	2.7
Pt ₅ -CNT(8,0)	6.39	-237	0.117	-0.220	39.0	+0.065	8.4
Pt ₅ -CNT(12,0)	9.48	-178	0.051	-0.236	46.7	+0.063	22.5

Table 2.4 The change of charge from reaction state to transition state in the activation of the secondary C-H bond of propane over the top Pt site on the Pt₅-CNT.

	Change of Charge $\Delta\rho = \rho_{TS} - \rho_R$ (e)					
	CNT	Pt ₅	Pt ₅ -CNT	Pt active site	C	H
Pt ₅ -CNT(4,0)	-0.095	-0.075	-0.170	0.149	-0.086	0.035
Pt ₅ -CNT(6,0)	-0.101	-0.034	-0.135	0.154	-0.093	0.022
Pt ₅ -CNT(8,0)	-0.105	-0.042	-0.147	0.142	-0.078	0.040
Pt ₅ -CNT(12,0)	-0.142	0.001	-0.141	0.145	-0.092	0.031

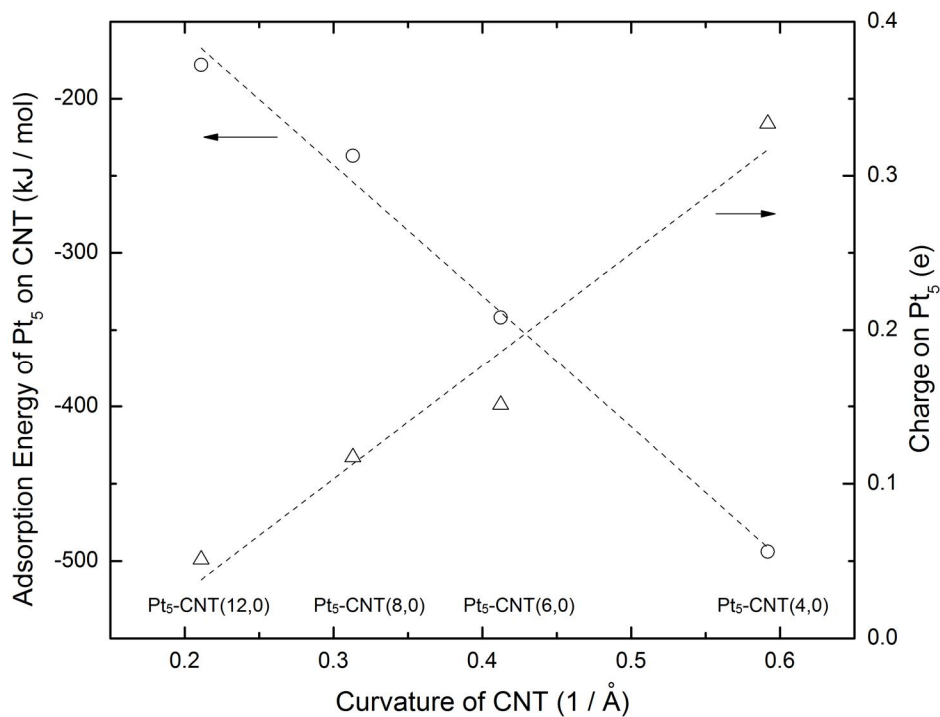


Figure 2.8 The effect of the curvature of the CNT support on the Pt adsorption energy and corresponding electron transfer from the Pt₅ cluster to the CNT support.

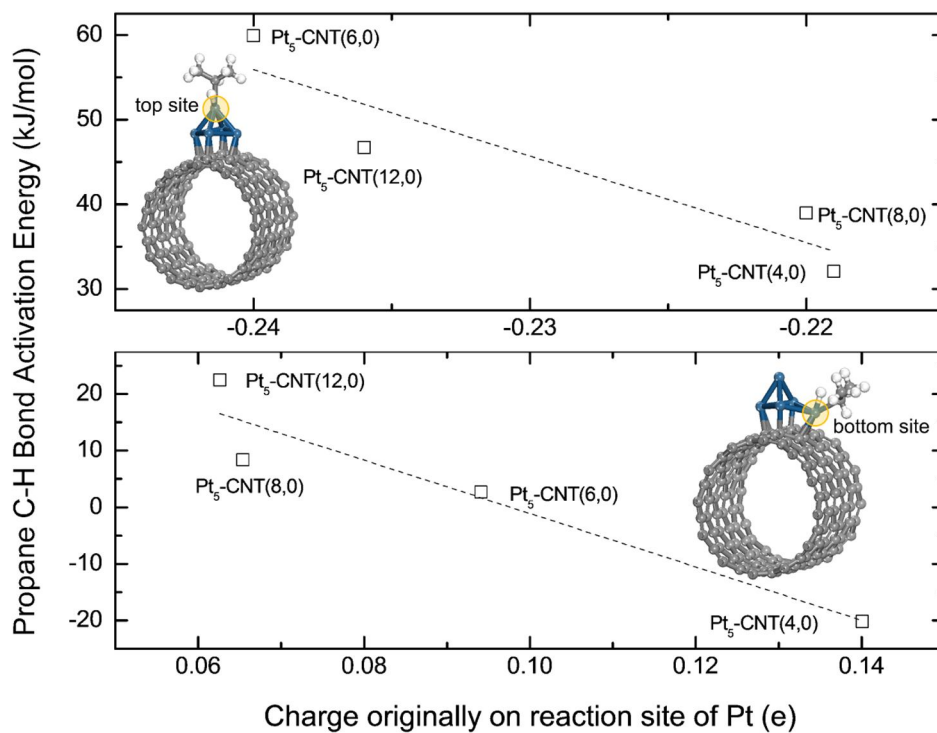


Figure 2.9 The effect of charge on the top (upper panel) and bottom (lower panel) Pt sites of Pt₅-CNT on the resulting apparent activation barriers for the activation of the secondary C-H bond of propane.

2.4 Summary

DFT calculations were carried out to analyze the effects of metal, cluster size and support on the initial activation of the C-H bonds of propane over bare Pt_n and Co_n sub-nanometer clusters and Pt_5 on single-walled carbon nanotube supports. Within the studied size range, Pt_n clusters were found to have a much higher activity than Co_n clusters for propane activation. In the transition state for the activation of the secondary C-H bond of propane, the Pt_n clusters accept electrons from propane, whereas Co_n clusters donate electrons to propane. The intrinsic barriers for C-H bond activation are directly correlated with the chemical hardness of Pt_n and Co_n clusters. Pt_5 -CNT models were used to study the CNT support effect on propane activation. The top Pt atom that is not bonding to CNT acquires a negative charge due to the polarization induced by the charge transfer from the Pt cluster to the CNT substrate. The activation of the C-H bond at this top Pt site on Pt_5 -CNT has a much higher barrier than that on bare Pt_5 cluster, which is consistent with experimental observation that anionic Pt clusters are less reactive than charge neutral and cationic ones. Our calculations also indicate that it is viable to tune the catalytic activities of CNT supported sub-nanometer metal clusters by varying the diameter of CNT.

Supplementary Materials

We observed drastic re-structuring of some metal cluster models, which made it very difficult to compare with results on the well-structured models. This restructuring indicates a poor choice of the structural configuration and an unstable cluster. As such, we do not report the results on those clusters herein. Small clusters, either free-standing or supported, typically exhibit a number of different interconvertible configurations, and this structural fluxionality was also observed in previous theoretical studies [60]. The fluxionality of small clusters may indicate unstable catalysts that can undergo sintering or the adaptability of the clusters to catalyze certain reactions.

A set of test DFT calculations with the correction of van der Waals interactions, which are described via a simple pair-wise force field by Grimme's [61] DFT-D2 method, were carried out for the first C-H activation of propane on Pt₆ (see Figure 2.10). The adsorption energy of propane onto Pt₆ is 15 kJ mol⁻¹ stronger with the correction of van der Waals interactions. However the intrinsic C-H bond activation barrier and the reaction energy only change 1 kJ mol⁻¹ and 4 kJ mol⁻¹, respectively. Therefore ignoring the dispersion correction will not substantially affect our discussion of C-H bond activation over Pt_n and Co_n clusters.

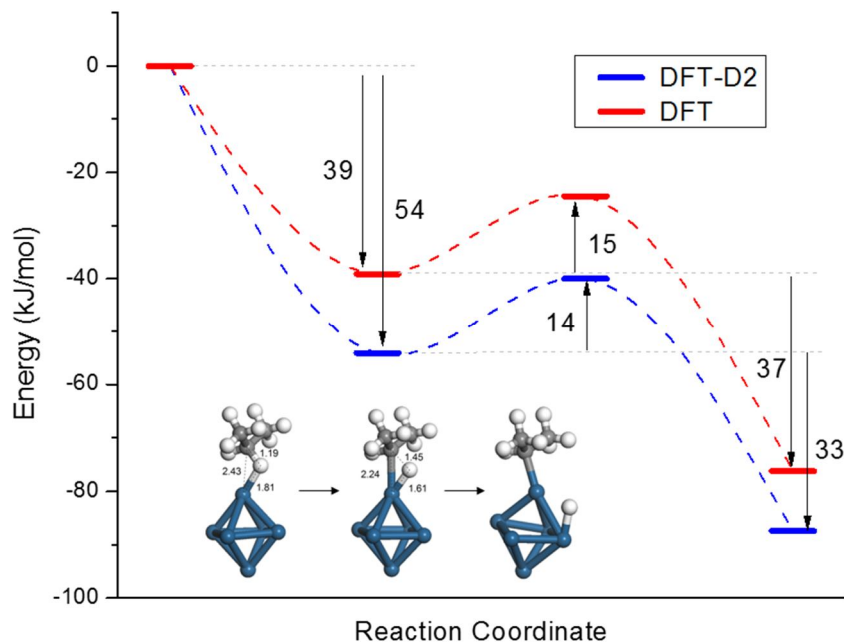


Figure 2.10 Comparison of DFT-D2 (with the correction of van der Waals interactions) and DFT-calculated energy profile of propane activation on the Pt₆ cluster.

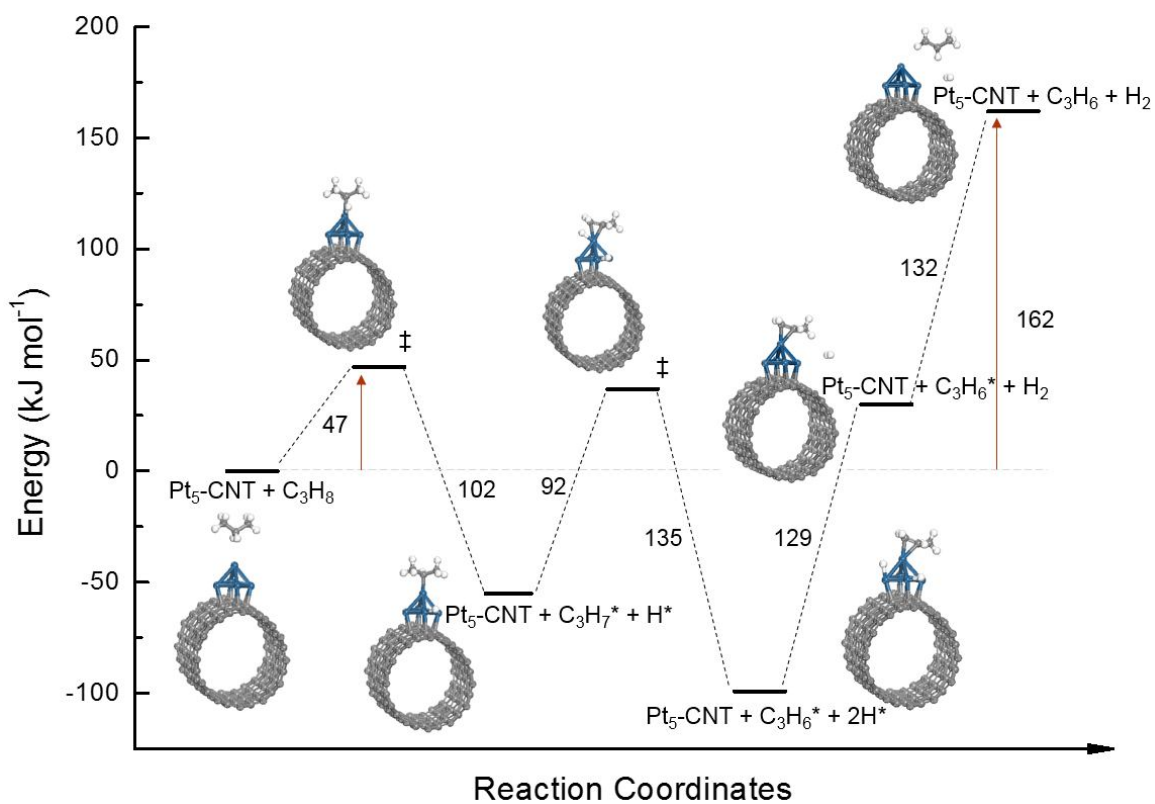


Figure 2.11 DFT-calculated potential energy diagram for the dehydrogenation of propane to propylene on Pt₅-CNT(12,0).

References

1. H. Lander and A.C. Nixon, *Endothermic fuels for hypersonic vehicles*. Journal of Aircraft, 1971. **8**(4): p. 200-207.
2. G.B. Giacobbe, *CEH Marketing Research Report: Propylene*, in *Chemical Economics Handbook*. 2011, SRI Consulting.
3. H.F. Rase, *Handbook of Commercial Catalysts: Heterogeneous Catalysts*. 2000: CRC Press.
4. *Annual Energy Outlook*. 2013, U.S. Energy Information Administration, Office of Integrated and International Energy Analysis, U.S. Department of Energy: Washington, DC.
5. G.C. Bond, *Dehydrogenation of Alkanes*, in *Metal-Catalysed Reactions of Hydrocarbons*. 2005, Springer. p. 501-523.
6. J. Gregor and D. Wei, *UOP Oleflex Process for Light Olefin Production*, in *Handbook of Petroleum Refining Processes*, A.M. Robert, Editor. 2003, McGraw-Hill. p. 5.3-5.10.
7. H. Burghgraef, A.P.J. Jansen, and R.A. van Santen, *Electronic structure calculations and dynamics of methane activation on nickel and cobalt*. The Journal of Chemical Physics, 1994. **101**(12): p. 11012-11020.
8. E. Ruckenstein and H.Y. Wang, *Carbon dioxide reforming of methane to synthesis gas over supported cobalt catalysts*. Applied Catalysis A: General, 2000. **204**(2): p. 257-263.
9. E. Ruckenstein and H.Y. Wang, *Carbon Deposition and Catalytic Deactivation during CO₂ Reforming of CH₄ over Co/ γ -Al₂O₃ Catalysts*. Journal of Catalysis, 2002. **205**(2): p. 289-293.
10. K. Nagaoka, K. Takanabe, and K.-i. Aika, *Modification of Co/TiO₂ for dry reforming of methane at 2 MPa by Pt, Ru or Ni*. Applied Catalysis A: General, 2004. **268**(1-2): p. 151-158.
11. K. Takanabe, K. Nagaoka, K. Nariai, and K.-i. Aika, *Influence of reduction temperature on the catalytic behavior of Co/TiO₂ catalysts for CH₄/CO₂ reforming and its relation with titania bulk crystal structure*. Journal of Catalysis, 2005. **230**(1): p. 75-85.
12. H. Haberland, ed. *Clusters of Atoms and Molecules II: Solvation and Chemistry of Free Clusters, and Embedded, Supported and Compressed Clusters*. Springer Series in Chemical Physics. Vol. 56. 1994, Springer.
13. A. Kaldor, D.M. Cox, and M.R. Zakin, *Molecular Surface Chemistry: Reactions of Gas-Phase Metal Clusters*, in *Evolution of Size Effects in Chemical Dynamics Part 2*, I. Prigogine and S.A. Rice, Editors. 1988, John Wiley & Sons, Inc. p. 211-261.
14. U. Heiz, F. Vanolli, A. Sanchez, and W.D. Schneider, *Size-Dependent Molecular Dissociation on Mass-Selected, Supported Metal Clusters*. Journal of the American Chemical Society, 1998. **120**(37): p. 9668-9671.
15. Z. Xu, F.S. Xiao, S.K. Purnell, O. Alexeev, S. Kawi, S.E. Deutsch, and B.C. Gates, *Size-dependent catalytic activity of supported metal clusters*. Nature, 1994. **372**(6504): p. 346-348.
16. U. Heiz, F. Vanolli, L. Trento, and W.D. Schneider, *Chemical reactivity of size-selected supported clusters: An experimental setup*. Review of Scientific Instruments, 1997. **68**(5): p. 1986-1994.
17. U. Heiz, A. Sanchez, S. Abbet, and W.D. Schneider, *Catalytic Oxidation of Carbon Monoxide on Monodispersed Platinum Clusters: Each Atom Counts*. Journal of the American Chemical Society, 1999. **121**(13): p. 3214-3217.
18. B. Hammer, O.H. Nielsen, and J.K. Nørskov, *Structure sensitivity in adsorption: CO interaction with stepped and reconstructed Pt surfaces*. Catalysis Letters, 1997. **46**(1-2): p. 31-35.
19. N. Watari and S. Ohnishi, *Electronic structure of H adsorbed on Pt₁₃ clusters*. The Journal of Chemical Physics, 1997. **106**(18): p. 7531-7540.
20. Y. Xing, *Synthesis and Electrochemical Characterization of Uniformly-Dispersed High Loading Pt Nanoparticles on Sonochemically-Treated Carbon Nanotubes*. The Journal of Physical Chemistry B, 2004. **108**(50): p. 19255-19259.
21. Y. Mu, H. Liang, J. Hu, L. Jiang, and L. Wan, *Controllable Pt Nanoparticle Deposition on Carbon Nanotubes as an Anode Catalyst for Direct Methanol Fuel Cells*. The Journal of Physical Chemistry B, 2005. **109**(47): p. 22212-22216.
22. Y. Wang, N. Shah, F.E. Huggins, and G.P. Huffman, *Hydrogen Production by Catalytic Dehydrogenation of Tetralin and Decalin Over Stacked Cone Carbon Nanotube-Supported Pt Catalysts*. Energy & Fuels, 2006. **20**(6): p. 2612-2615.

23. J.M. Planeix, N. Coustel, B. Coq, V. Brotons, P.S. Kumbhar, R. Dutartre, P. Geneste, P. Bernier, and P.M. Ajayan, *Application of Carbon Nanotubes as Supports in Heterogeneous Catalysis*. Journal of the American Chemical Society, 1994. **116**(17): p. 7935-7936.
24. P. Hohenberg and W. Kohn, *Inhomogeneous Electron Gas*. Physical Review, 1964. **136**(3B): p. B864.
25. W. Kohn and L.J. Sham, *Self-Consistent Equations Including Exchange and Correlation Effects*. Physical Review, 1965. **140**(4A): p. A1133.
26. G. Kresse and J. Hafner, *Ab initio molecular dynamics for liquid metals*. Phys. Rev. B, 1993. **47**: p. 558.
27. G. Kresse and J. Hafner, *Ab initio molecular-dynamics simulation of the liquid-metal-amorphous-semiconductor transition in germanium*. Phys. Rev. B, 1994. **49**: p. 14251.
28. G. Kresse and J. Furthmüller, *Efficiency of ab-initio total energy calculations for metals and semiconductors using a plane-wave basis set*. Comput. Mat. Sci., 1996. **6**: p. 15.
29. G. Kresse and J. Furthmüller, *Efficient iterative schemes for ab initio total-energy calculations using a plane-wave basis set*. Phys. Rev. B, 1996. **54**: p. 11169.
30. J.P. Perdew, K. Burke, and M. Ernzerhof, *Generalized Gradient Approximation Made Simple*. Phys. Rev. Lett., 1996. **77**: p. 3865.
31. J.P. Perdew, K. Burke, and M. Ernzerhof, *Erratum: Generalized Gradient Approximation Made Simple*. Phys. Rev. Lett., 1997. **78**: p. 1396.
32. P.E. Blöchl, *Projector augmented-wave method*. Phys. Rev. B, 1994. **50**: p. 17953.
33. G. Kresse and D. Joubert, *From ultrasoft pseudopotentials to the projector augmented-wave method*. Phys. Rev. B, 1999. **59**: p. 1758.
34. G. Mills, H. Jónsson, and G.K. Schenter, *Reversible work transition state theory: application to dissociative adsorption of hydrogen*. Surface Science, 1995. **324**(2-3): p. 305-337.
35. G. Henkelman, B.P. Uberuaga, and H. Jónsson, *A climbing image nudged elastic band method for finding saddle points and minimum energy paths*. The Journal of Chemical Physics, 2000. **113**(22): p. 9901-9904.
36. H. Graeme and J. Hannes, *A dimer method for finding saddle points on high dimensional potential surfaces using only first derivatives*. The Journal of Chemical Physics, 1999. **111**(15): p. 7010-7022.
37. D. Mei, *Monte Carlo Simulation Program for Energetics and Structure of Metal Clusters*. 2005: Charlottesville, VA.
38. M.S. Daw and M.I. Baskes, *Embedded-atom method: Derivation and application to impurities, surfaces, and other defects in metals*. Physical Review B, 1984. **29**(12): p. 6443-6453.
39. H.J. Monkhorst and J.D. Pack, *Special points for Brillouin-zone integrations*. Physical Review B, 1976. **13**(12): p. 5188-5192.
40. T. Koopmans, *Über die Zuordnung von Wellenfunktionen und Eigenwerten zu den Einzelnen Elektronen Eines Atoms*. Physica, 1934. **1**(1-6): p. 104-113.
41. C.-G. Zhan, J.A. Nichols, and D.A. Dixon, *Ionization Potential, Electron Affinity, Electronegativity, Hardness, and Electron Excitation Energy: Molecular Properties from Density Functional Theory Orbital Energies*. The Journal of Physical Chemistry A, 2003. **107**(20): p. 4184-4195.
42. J. Neugebauer and M. Scheffler, *Adsorbate-substrate and adsorbate-adsorbate interactions of Na and K adlayers on Al(111)*. Physical Review B, 1992. **46**(24): p. 16067-16080.
43. G. Makov and M.C. Payne, *Periodic boundary conditions in ab initio calculations*. Physical Review B, 1995. **51**(7): p. 4014-4022.
44. R.G. Parr and R.G. Pearson, *Absolute hardness: companion parameter to absolute electronegativity*. Journal of the American Chemical Society, 1983. **105**(26): p. 7512-7516.
45. D.J. Trevor, D.M. Cox, and A. Kaldor, *Methane activation on unsupported platinum clusters*. Journal of the American Chemical Society, 1990. **112**(10): p. 3742-3749.
46. M.D. Morse, M.E. Geusic, J.R. Heath, and R.E. Smalley, *Surface reactions of metal clusters. II. Reactivity surveys with D₂, N₂, and CO*. The Journal of Chemical Physics, 1985. **83**(5): p. 2293-2304.
47. G. Henkelman, A. Arnaldsson, and H. Jónsson, *A fast and robust algorithm for Bader decomposition of charge density*. Computational Materials Science, 2006. **36**(3): p. 354-360.
48. W. Tang, E. Sanville, and G. Henkelman, *A grid-based Bader analysis algorithm without lattice bias*. Journal of Physics: Condensed Matter, 2009. **21**(8): p. 084204.
49. A.E. Shilov and G.B. Shul'pin, *Activation of C-H Bonds by Metal Complexes*. Chemical Reviews, 1997. **97**(8): p. 2879-2932.

50. D.H. Ess, R.J. Nielsen, W.A. Goddard III, and R.A. Periana, *Transition-State Charge Transfer Reveals Electrophilic, Ambiphilic, and Nucleophilic Carbon–Hydrogen Bond Activation*. Journal of the American Chemical Society, 2009. **131**(33): p. 11686-11688.
51. S. Goldman Alan and I. Goldberg Karen, *Organometallic C-H Bond Activation: An Introduction*, in *Activation and Functionalization of C-H Bonds*. 2004, American Chemical Society. p. 1-43.
52. T. Imaoka, H. Kitazawa, W.-J. Chun, S. Omura, K. Albrecht, and K. Yamamoto, *Magic Number Pt₁₃ and Misshapen Pt₁₂ Clusters: Which One is the Better Catalyst?* Journal of the American Chemical Society, 2013. **135**(35): p. 13089-13095.
53. O. Diéguez, M.M.G. Alemany, C. Rey, P. Ordejón, and L.J. Gallego, *Density-functional calculations of the structures, binding energies, and magnetic moments of Fe clusters with 2 to 17 atoms*. Physical Review B, 2001. **63**(20): p. 205407.
54. A.N. Andriotis and M. Menon, *Tight-binding molecular-dynamics study of ferromagnetic clusters*. Physical Review B, 1998. **57**(16): p. 10069-10081.
55. J. Russell, P. Zapol, P. Král, and L.A. Curtiss, *Methane bond activation by Pt and Pd subnanometer clusters supported on graphene and carbon nanotubes*. Chemical Physics Letters, 2012. **536**(0): p. 9-13.
56. K. Okazaki-Maeda, Y. Morikawa, S. Tanaka, and M. Kohyama, *Structures of Pt clusters on graphene by first-principles calculations*. Surface Science, 2010. **604**(2): p. 144-154.
57. H. Yasumatsu, P. Murugan, and Y. Kawazoe, *Nanospace charge polarization of monatomic-layered platinum cluster disk constructed on silicon(111)-7 × 7 surface*. physica status solidi (b), 2012. **249**(6): p. 1193-1198.
58. U. Achatz, C. Berg, S. Joos, B.S. Fox, M.K. Beyer, G. Niedner-Schatteburg, and V.E. Bondybey, *Methane activation by platinum cluster ions in the gas phase: effects of cluster charge on the Pt₄ tetramer*. Chemical Physics Letters, 2000. **320**(1–2): p. 53-58.
59. C. Adlhart and E. Uggerud, *Reactions of platinum clusters Pt_n[±], n = 1-21, with CH₄: to react or not to react*. Chemical Communications, 2006(24): p. 2581-2582.
60. N.T. Cuong, A. Sugiyama, A. Fujiwara, T. Mitani, and D.H. Chi, *Density functional study of Pt₄ clusters adsorbed on a carbon nanotube support*. Physical Review B (Condensed Matter and Materials Physics), 2009. **79**(23): p. 235417-7.
61. S. Grimme, *Semiempirical GGA-type density functional constructed with a long-range dispersion correction*. Journal of Computational Chemistry, 2006. **27**(15): p. 1787-1799.

Chapter 3 Selective Dehydrogenation of Cyclohexane on Pt nm-particles

3.1 Introduction

Metal nanoparticles have different catalytic activity versus single-crystal surfaces, because of their high surface-area-to-volume ratio, high fraction of coordinatively unsaturated edge and corner sites [1, 2], and increased number of sites at the metal-support interface [3]. The changes in the size and shape of the metal particles will dictate their distribution of sites with different coordination numbers which in turn will affect the overall catalytic rate of reaction [4] as well as the mobility of surface species [5, 6]. While it is well-established that the changes in the size of catalytic metal nanoparticles can significantly influence their catalytic activity [7, 8], there are very few studies that report on how changes in the metal particle size and shape influence selectivity. In a recent experimental study, Pfefferle et al. [9] carried out well-controlled syntheses to produce highly stable supported Pt nanoparticles that were subsequently used in the catalytic dehydrogenation of cyclohexane. These syntheses along with in-situ characterization and first-principles theoretical calculations were used to gain insights into how the metal structure and particle size influence catalytic activity and selectivity. Herein, we present the detailed density functional theory (DFT) calculations along with experimental results to demonstrate how changes in the catalyst particle size dictate the distribution of different metal surface sites and how these sites control different elementary reaction steps that can subsequently alter catalytic selectivity.

Cycloalkanes form a considerable portion of most fuels [10]; their catalytic dehydrogenation paths offer a route towards improved fuel activation at lower temperatures and better heat sinks for regeneratively-cooled jet engines and gas turbines. Dehydrogenation of cyclohexane is a structure-sensitive reaction that appears to be promoted at the coordinative unsaturated metal sites that occur at stepped Pt surfaces as well as edge and corner sites found on small Pt particles [11-13]. Pfefferle et al. [9] were able to control the sizes of Pt nanoparticles by using different pretreatment to the supporting carbon nanotube. They showed that different sized Pt nanoparticles supported on carbon nanotubes directly influenced the catalytic selectivity for cyclohexane dehydrogenation: where larger Pt particles (2.2 nm) selectively produced cyclohexene and cyclohexadiene; while smaller Pt particles (1.3 nm) resulted in the formation of cyclohexadiene and benzene. DFT calculations identify surface sites with markedly different barriers for the activation of the C-H bond as well as the barriers for the desorption of different intermediates; the distribution of different sites thus dictates the catalytic activity as well as the selectivity.

3.2 Method

First-principles plane wave density functional theory calculations were used to examine the reactants, intermediates and products for the full-range of reactions in the dehydrogenation of cyclohexane. All calculations were carried out using periodic density functional theory (DFT) as implemented in the Vienna *ab initio* Simulation Package (VASP) [14-17]. The generalized gradient approximation (GGA), in the form of Perdew-Burke-Ernzerhof (PBE) [18, 19] was used to model exchange and correlation corrections. The interaction between the valence electrons and the core was described with the projector augmented wave method (PAW) [20, 21], where the kinetic-energy cutoff for plane wave basis set was 400 eV, which was sufficient to obtain well-converged energies. The Brillouin zone sampling was restricted to a single Γ -point. The structure optimization was carried out until the force due to displacements of each atom in the unit cell converged to within 0.05 eV/Å. In order to establish the minimum energy reaction pathway (MEP) for each of the reactions of interest, a series of eight to sixteen images were chosen by interpolating a set of equally spaced points between the individual reactant and their product, and subsequently optimized via nudged elastic band (NEB) algorithm [22] until the maximum force on each of the atoms was found to be lower than to 0.2 eV/Å. Starting from NEB calculations, the Dimer [23] method was employed, and transition states were determined when the force on each atom converged within 0.05 eV/Å.

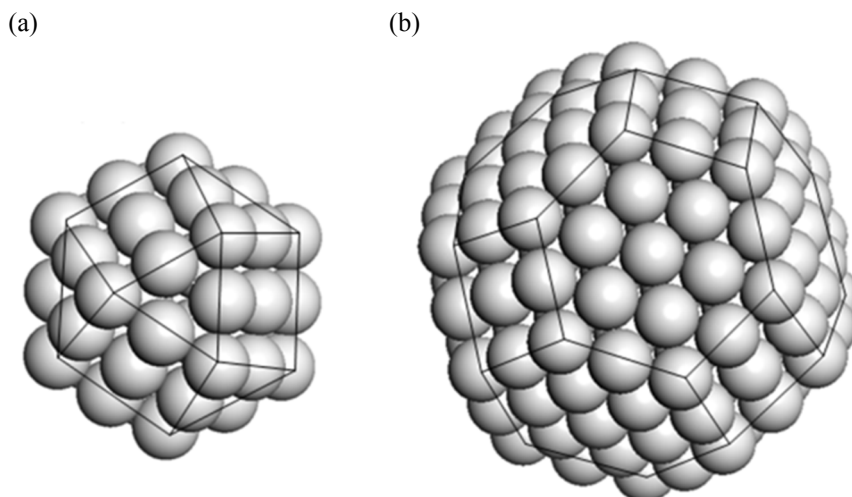


Figure 3.1 Structure of the cubo-octahedral Pt₅₅ cluster (a) and structure of the truncated cubo-octahedral Pt₂₀₁ cluster (b).

A cubo-octahedral Pt₅₅ cluster was used to model a 1.2 nm platinum nanoparticle. Larger platinum particles with diameters of ~ 1.8 nm were modeled by using a truncated cubo-octahedral Pt₂₀₁ cluster. Figure 3.1 shows the structures of these two Pt clusters. The statistics of surface atoms for these two nanoparticles are summarized in Table 3.1. It is worth noting that on the Pt₅₅ cluster all the atoms of the (111)-like facet are actually edge or corner sites with lower coordination numbers than those on extended (111) surfaces, and only the center atom of the (100)-like facet has the same coordination number with (100) single crystal surface. The structures of the Pt clusters were optimized with all the atoms fully relaxed. In the calculations of adsorption energies, only the top two layers of the cluster were relaxed, the rest Pt atoms were kept fixed. The Pt₅₅ and Pt₂₀₁ clusters were kept in unit cells with one of the facets perpendicular to the z-axis; the size of unit cells are $22 \times 22 \times 22 \text{ \AA}^3$ and $28 \times 28 \times 28 \text{ \AA}^3$, respectively. Several tests confirmed the unit cells were large enough to obtain satisfactorily converged energies.

Table 3.1 Summary of the number and percentage of surface atoms on cubo-octahedral Pt₅₅ and truncated cubo-octahedral Pt₂₀₁ clusters.

Pt cluster	Number of surface atoms	corner		edge		(100)-like facet		(111)-like facet	
		count	%	count	%	count	%	count	%
Pt ₅₅	42	12	28.6	24	57.1	6	14.3	0	0.0
Pt ₂₀₁	122	24	19.7	36	29.5	6	4.9	56	45.9

The bare particle models (Figure 3.2a), which represent low surface coverage situation, may not accurately describe the actual catalytic environment, where metal particles are likely covered by co-adsorbed hydrocarbon intermediates and hydrogen. Without loss of generality, we mimic the high coverage of co-adsorbed hydrocarbon species on Pt₂₀₁ by surrounding the adsorbed C₆H_x surface species with benzene molecules (Figure 3.2b), which leads to a surface coverage of about one C₆H_x molecule per four Pt atoms, beyond which multilayer adsorption is observed in experiments [24].

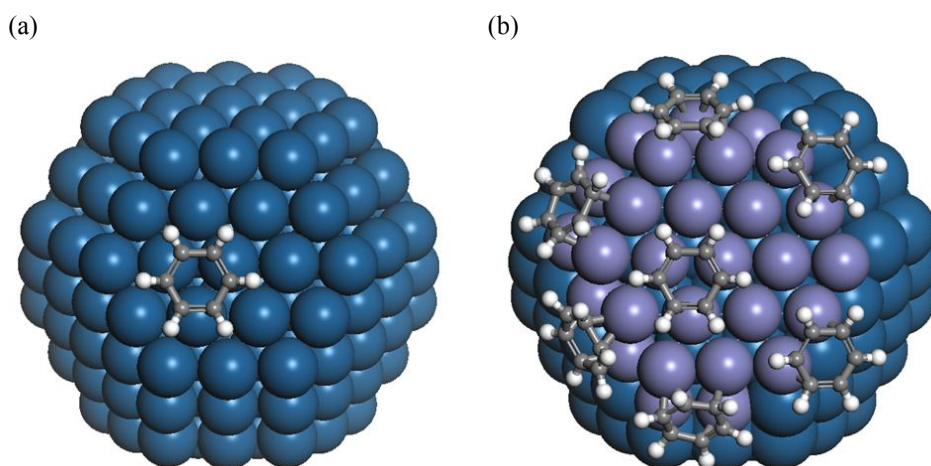


Figure 3.2 Truncated cubo-octahedral cluster models for the adsorption of benzene on: (a) the low coverage bare Pt₂₀₁ particle, and (b) the high coverage Pt₂₀₁ cluster with 6 neighboring benzene molecules (High coverage surface Pt atoms are shown in purple where there is one C₆H_x molecule per four Pt atoms).

The binding energy of adsorbate A on the platinum cluster was determined by the equation

$$E_{\text{ads}}(\text{A}) = E(\text{A}^*) - E(\text{bare cluster}) - E(\text{A, gas phase}) \quad (3.1)$$

The reaction energy for C-H activation, which can be represented as $\text{A}^* \rightarrow \text{B}^* + \text{H}^*$ where A^* , B^* and H^* refer to the adsorbed hydrocarbon intermediate (C_mH_n) and the resulting dehydrogenated hydrocarbon (C_mH_{n-1}) and surface hydrogen (H^*), was calculated as:

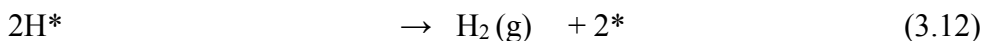
$$E_{\text{rxn}}(\text{A} \rightarrow \text{B}) = E(\text{B}^*) + E_{\text{ads}}(\text{H}) - E(\text{A}^*) \quad (3.2)$$

where $E_{\text{ads}}(\text{H})$ is the adsorption energy of a hydrogen atom.

3.3 Results and Discussion

3.3.1 Plausible reaction paths of *c*-C₆H₁₂ dehydrogenation on bare Pt₅₅ and Pt₂₀₁

DFT calculations were carried out to analyze the reaction pathways involved in the stepwise dehydrogenation of cyclohexane to cyclohexene, cyclohexadiene and benzene shown in Eqns. (3.3-12):



over both Pt₅₅ (~1.2 nm) and Pt₂₀₁ (~1.8 nm) nanoparticles where * refers to a Pt surface site. The lowest energy profile on (111) facets of both Pt₅₅ and Pt₂₀₁ particles are shown in Figure 3.3 (other plausible paths were also explored and are summarized in supplementary Figures 3.8 and 3.9). While the elementary steps over both the Pt₅₅ and Pt₂₀₁ clusters are

the same, the reactions that occur over the (111)-like facets of Pt₅₅ in Path B involve more coordinatively unsaturated Pt sites than those on the (111) terrace of Pt₂₀₁ in Path A. The first step in the activation of cyclohexane involves the activation of an equatorial C-H bond at a Pt site. The axial C-H bond at C2 is subsequently activated at an adjacent Pt site. These two steps result in the formation of cyclohexene adsorbed di- σ on the Pt particle. The C-H bond at the C3 site on cyclohexene can be activated to form the bound 3-cyclohexenyl (c-C₆H₉) which is followed by the subsequent C-H activation to form adsorbed 1,3-cyclohexadiene. The final two C-H activation steps result in the formation of benzene. The energy diagrams in Figure 3.3 clearly show that the C₆H_x surface intermediates are much more strongly bound to the Pt₅₅ cluster than those on Pt₂₀₁ and as such have much lower C-H activation barriers. This suggests that the stepwise dehydrogenation of cyclohexane proceeds further along the C-H bond activation path on smaller Pt nanoparticles than it does on larger nanoparticles thus resulting in higher yields of benzene.

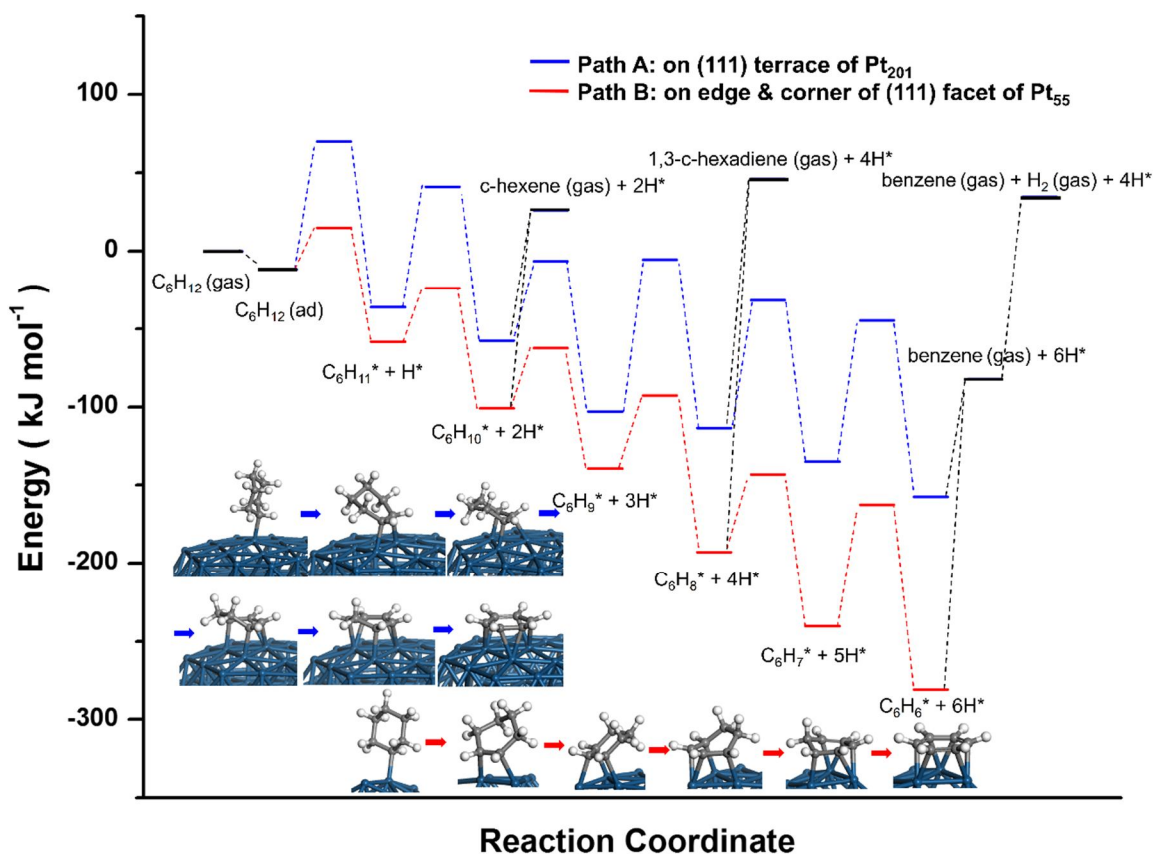


Figure 3.3 DFT-calculated potential energy diagram for plausible reaction pathways involved in the sequential dehydrogenation of cyclohexane to cyclohexene, cyclohexadiene and benzene on the bare Pt_{55} and Pt_{201} particles. In Path A, all the reactions are carried out on the coordinatively saturated Pt sites on the (111) terraces of Pt_{201} . In Path B, all of the C-H activation reactions are carried out on the (111)-type facet of the Pt_{55} cluster which is comprised of one coordinatively saturated terrace site and coordinatively unsaturated edge and corner sites. The zero energy reference for both Pt_{55} and Pt_{201} clusters is the infinitely separated gas-phase cyclohexane plus the Pt particle. In calculation of reaction energies for all dehydrogenation steps, the calculated hydrogen binding energy of $384.3 \text{ kJ mol}^{-1}$ was used.

3.3.2 Statistical sampling of reactions over bare and covered Pt nanoparticles

If we assume that the properties of metal depend only upon the number and arrangement of its nearest neighbors, we can determine the catalytic reactivity of a metal particle of different sizes and shapes as they dictate the distribution of different surface sites comprised of different coordination environments [25]. The collective catalytic properties of the particle can then be determined by counting the fraction of different sites (as shown in the “site count” columns in Tables 3.2 and 3.3). In order to obtain a more quantitative view of the size dependence of cyclohexane dehydrogenation, we calculated the barriers and rate constants for C-H activation at each of the different surface sites (edges, corners, (111) terraces and (100) terraces) over both the Pt₅₅ and Pt₂₀₁ clusters (Figure 3.4) and used these values along with the statistical distribution of different sites on various different sized clusters to examine the cluster size and morphology effects. As an example, we examine the C-H activation steps in the dehydrogenation of adsorbed cyclohexene (c-C₆H₁₀) at different sites at both low and high coverages. Adsorbed cyclohexene, which is a key intermediate in the dehydrogenation of cyclohexane, can either dehydrogenate to form cyclohexadiene/benzene or desorb from the surface. The final product distribution critically depends upon the partitioning of these two competing processes, cyclohexene C-H bond activation and cyclohexene desorption. †

† Here we made two assumptions. The first is that the residence time for these reaction is very short and as such the re-adsorption of the gas phase products is negligible. This simplifies the theoretical analyses so that we can assume that desorption is irreversible. We can also assume that at the reaction temperature of 225 °C, the sequential dehydrogenation of cyclohexane is irreversible. This assumption is supported by previous studies carried out using sum frequency generation (SFG) vibrational spectroscopy at high-pressure reaction conditions, which show that on both of Pt(111) and Pt(100) cyclohexene tend to dehydrogenate at a temperature of about 200 °C, whereas the reverse reaction hydrogenation of cyclohexene is favored at a lower temperature of about 127 °C [26].

By assuming first-order kinetics, the desorption reaction rate of cyclohexene is

$$r_{des} = k_{des} [C_6H_{10}^*], \quad (3.13)$$

where k_{des} is the desorption rate constant and $[C_6H_{10}^*]$ is the surface concentration of cyclohexene.

The reaction rate for the unimolecular dehydrogenation of cyclohexene can then be expressed as:

$$r_{act} = k_{act} [C_6H_{10}^*]. \quad \dagger \quad (3.14)$$

where k_{act} is the C-H bond activation rate constant.

From transition state theory, we can relate the rate constant to barrier via Arrhenius expression

$$k_i = \nu_i e^{-\frac{E_i^\ddagger}{k_B T}}, \quad (3.15)$$

where E_i^\ddagger is the energy difference between transition state and initial state (or the energy barrier of desorption), ν_i is the Arrhenius pre-exponential factor for the elementary step. §

† We assume the unimolecular dehydrogenation of cyclohexene is pseudo-first-order with respect to the surface concentration of cyclohexene and zero-order in the concentration of available active site, which is relatively abundant and keeps constant. This assumption is supported by previous experimental observations. Thermal desorption spectra indicate hydrogen is readily desorbed from Pt(111) surfaces below 127 °C [27]. Therefore, at the reaction temperature of 225 °C, the surface is adsorbed with mostly hydrocarbons but little hydrogen. Due to facile diffusion in the adlayer, once the hydrogen adatom is produced on the Pt surface, it very rapidly finds another of its kind and associatively desorbs as H₂ before hydrocarbons leave the surface. Therefore only a very few free Pt sites need to be present in the adlayer to allow dehydrogenation [28-30].

§ Using Vineyard's formula [31, 32] the pre-exponential factor for cyclohexene dehydrogenation on (111) terrace of bare Pt₂₀₁ cluster was calculated to be 2.7 x 10¹³ s⁻¹, which is in good accordance with the typical pre-exponential factor ($k_B T/h \approx 10^{13}$ s⁻¹) for unimolecular surface decomposition [33]. While the pre-exponential factor for desorption is usually in the order of 10¹⁵ s⁻¹ [24].

Thus the ratio between desorption reaction rate r_{des} and C-H bond activation rate r_{act} at a given surface site can be calculated as

$$\frac{r_{des}}{r_{act}} = \frac{V_{des}}{V_{act}} e^{-\frac{E_{des}-E_{act}}{k_B T}} \quad (3.16)$$

The DFT calculations reported here in Tables 3.2, 3.3 and 3.4 include the C-H activation barrier results carried out at low coverages (bare particle) as well as at high coverages (benzene-covered). As shown in Figure 3.4a and b, all of the different sites on (111) and (100) facets of truncated cubo-octahedral nanoparticle were sampled to provide a statistical average. The calculations of cyclohexene adsorption energies and C-H bond activation barriers involved in the dehydrogenation of cyclohexene were carried out on each of the 12 different sites on bare Pt particles (to simulate the low coverage situation). The activation energies and barriers were also calculated at the high surface coverages as discussed and shown in Figures 3.5 and 3.6. The reaction energies and reaction rates for desorption and dehydrogenation of cyclohexene on different sites on the (111) facet, (100) facet of Pt₂₀₁ and along with those on Pt₅₅ were calculated and summarized in Tables 3.2, 3.3, and 3.4, respectively.

Our results show that on bare Pt particles reaction rates for the desorption of cyclohexene are comparable to or lower than the reaction rates for C-H bond activation, which indicates most of the adsorbed cyclohexene will be further dehydrogenated at low coverage. Cyclohexene binds rather strongly to the coordinate unsaturated Pt sites at low coverages and more readily undergoes C-H activation. At higher surface coverages (modeled here by

adding neighboring benzene species), however, the dehydrogenation of cyclohexene becomes more difficult, whereas the desorption of cyclohexene becomes easier, as a result of the lateral repulsive interaction and the conservation of bond order. The more realistic high surface coverage models depicted in Figure 3.5, thus show that the rate of desorption is more than an order of magnitude higher than the rate for C-H activation on the (111) terrace sites ($r_{\text{des}}/r_{\text{act}} > 10$). The rates for C-H activation at the more coordinatively unsaturated edge and corner sites, however, are higher or comparable to the rates of desorption as the cyclohexene is much more strongly held to the unsaturated edge and corner sites.

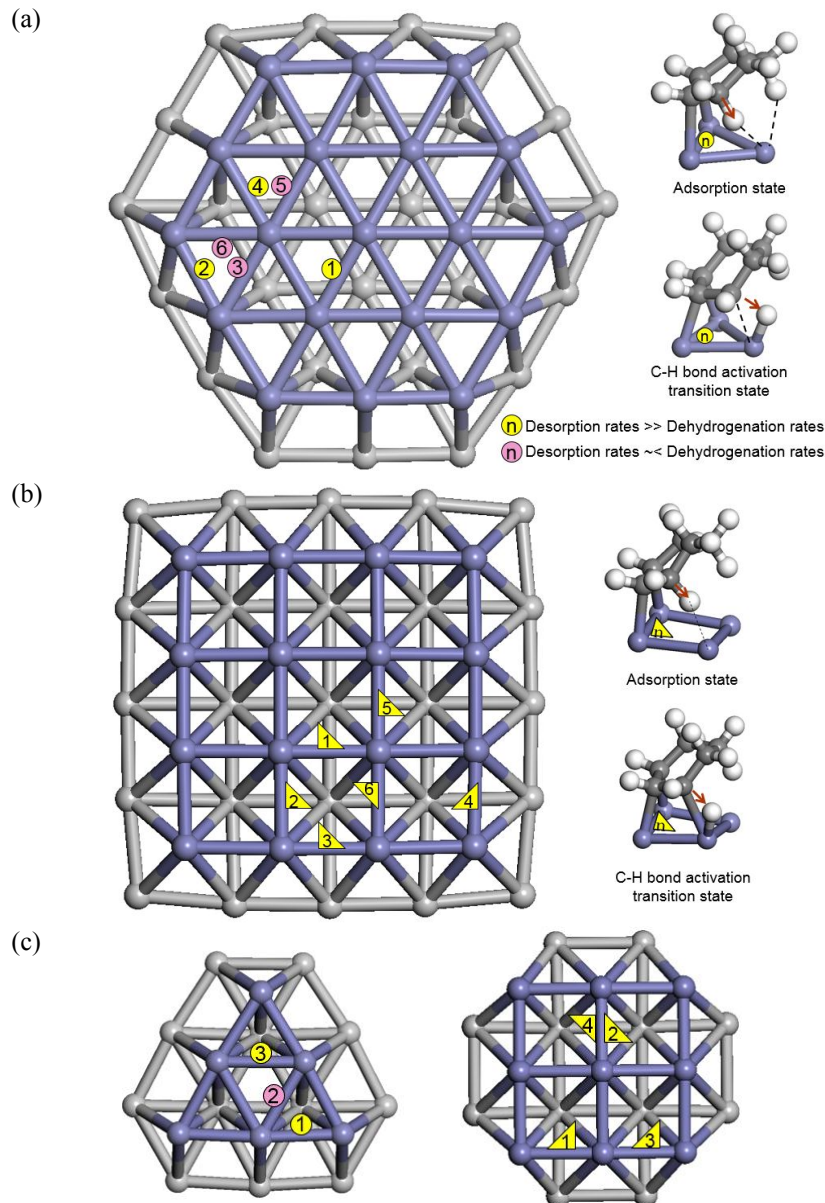


Figure 3.4 Different possible surface site ensembles necessary for the C-H bond activation of adsorbed cyclohexene. Two Pt sites are involved in the di- σ adsorption configuration whereas one additional neighboring Pt site is required to activate the C-H bond. Thus resulting in a three atom triangular Pt site ensemble. (a) On (111) terrace of truncated cubo-octahedral particles (Pt_{201}), the site ensemble is denoted by the number that is circled and placed on the inner side of the Pt-Pt bridge involved in adsorption. At high surface coverages, the rate of cyclohexene desorption is much higher than its rate of C-H activation and dehydrogenation for reactions that occur at the more coordinatively-saturated terrace sites (site ensembles are numbered yellow circle). Otherwise, the site combinations are numbered in purple circles (for details see Table 3.2). (b) On (100) terrace of truncated cubo-octahedral particle (Pt_{586}), a site ensemble is denoted by the number in a triangle placed on the inner side of the Pt-Pt bridge involved in adsorption with one angle pointing to the site for C-H activation. (c) On the (111) and (100) facets of cubo-octahedral particle (Pt_{55}), the site notation follows the convention in (a) and (b).

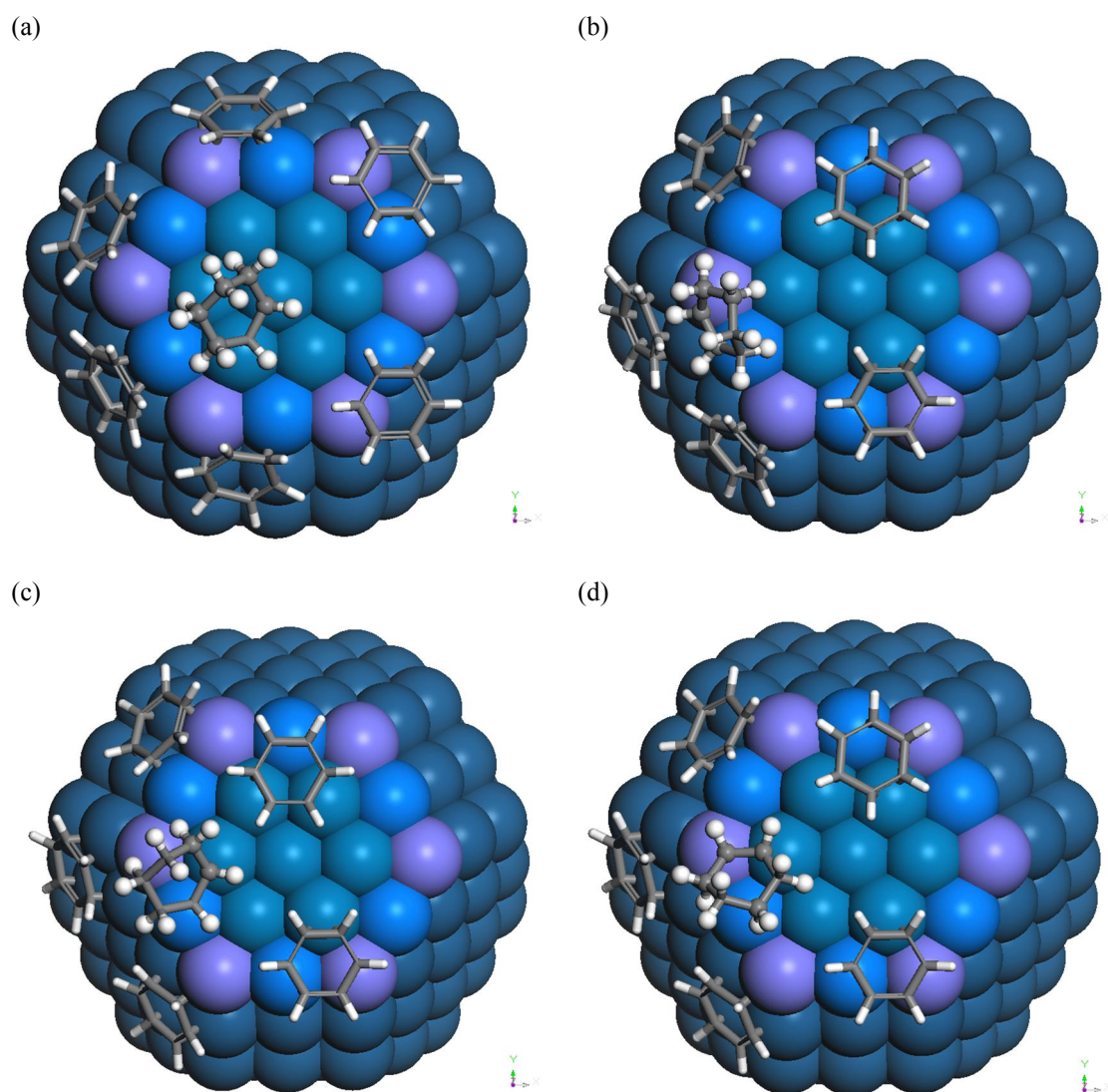


Figure 3.5 Explicit model for the high C_6H_x surface coverages for the reaction of cyclohexene on the (111) facet truncated cubo-octahedral particle Pt_{201} . Surface sites (a) Site 1, (b) Site 2, (c) Site 3 and (d) Site 6 are those as assigned in Figure 3.4a.

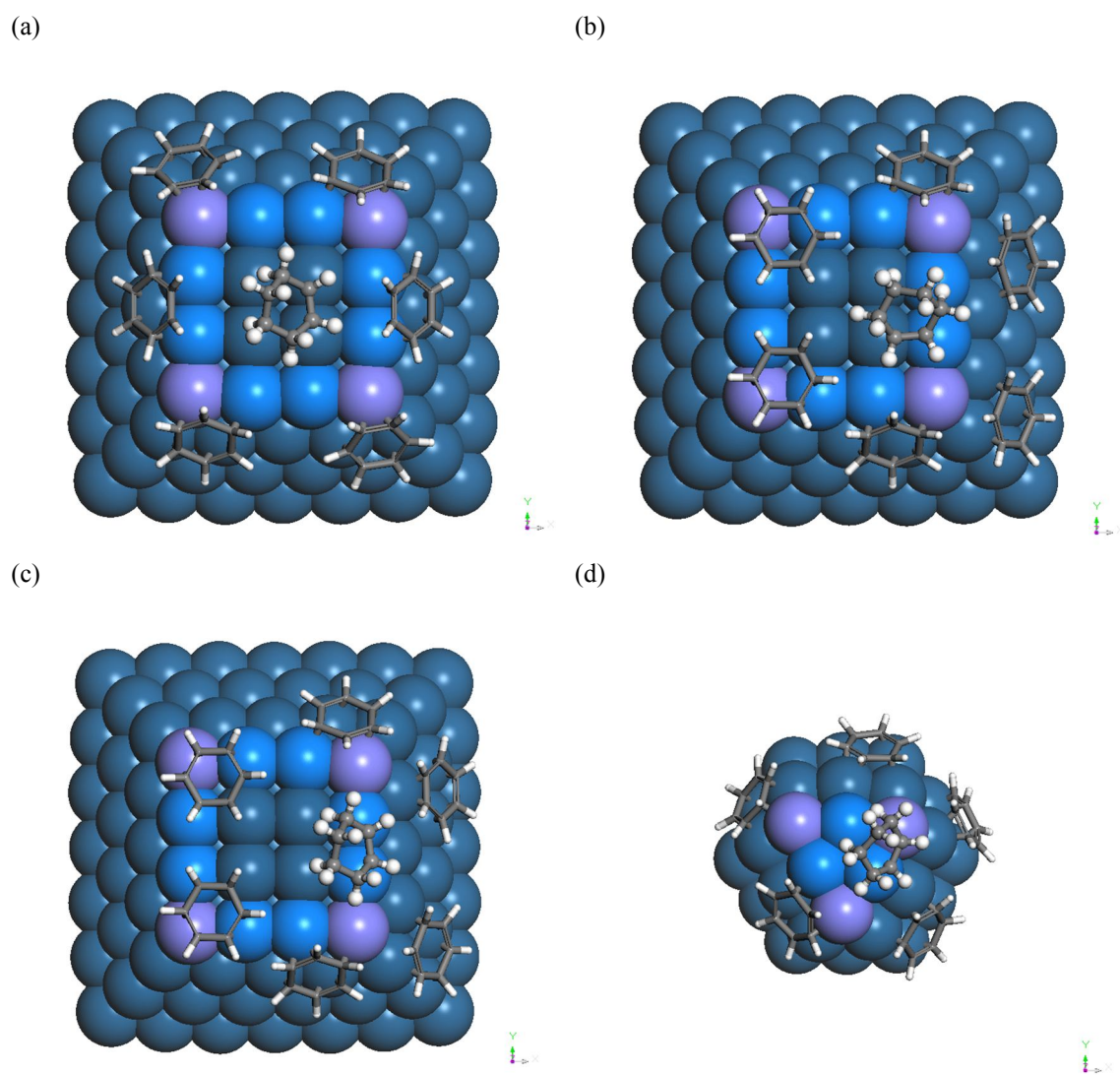


Figure 3.6 Explicit model for the high C_6H_x surface coverages for the reaction of cyclohexene on the (100) facet truncated cubo-octahedral particle Pt_{586} and (111) facet cubo-octahedral particle Pt_{55} . Surface sites (a) Site 1, (b) Site 2, (c) Site 3 are those as assigned in Figure 3.4b, and surface site (111)-1 (d) as in Figure 3.4c.

Table 3.2 DFT-calculated desorption energies, C-H activation energies and reaction rates for desorption and dehydrogenation reactions of cyclohexene with low coverage and high coverage at various surface sites on (111) facet of Pt₂₀₁ particle.

Pt ₂₀₁ particle (111) facet		Cyclohexene desorption energy E _{des} (kJ mol ⁻¹)		Cyclohexene C-H activation energy E _{act} (kJ mol ⁻¹)		Desorp. rate vs. dehydro. rate r_{des}/r_{act} ‡	
surface site*	site count**	low coverage	high coverage †	low coverage	high coverage †	low coverage	high coverage
1 (TT-T)	(<i>m</i> -2) ² ×6×3	83.6	54.1 <i>57.5</i>	64.0	69.4 <i>74.6</i>	0.896	6.10×10 ³
2 (EE(C)-T)	(<i>m</i> -1)×6	108.9	84.4 <i>83.0</i>	80.6	94.4 <i>94.3</i>	0.111	1.53×10 ³
3 (ET-C)	(<i>m</i> -2)×6×2	75.3	52.2 <i>49.2</i>	35.6	39.3 <i>40.8</i>	0.007	13.5
4 (ET-T)	(<i>m</i> -2)×6×2	77.2	<i>51.1</i>	57.1	<i>66.4</i>	0.795	4.00×10 ³
5 (TT-E)	(<i>m</i> -2)×6	84.0	<i>57.9</i>	38.4	<i>44.2</i>	0.002	3.66
6 (TC-E)	2×6	87.8	64.2 <i>61.7</i>	27.2	32.8 <i>30.9</i>	0.000	0.06

* surface sites see Figure 3.4a. (XY-Z) denotes a triangular 3-atom surface site ensemble comprised of two Pt sites involved in the di-σ adsorption of cyclohexene and one Pt site for the activation of the C-H bond. (T - terrace site; E - edge site; C - corner site)

** *m* is the number of atoms lying on an equivalent edge (corner atoms included, and *m*=3 for Pt₂₀₁)

† For the high coverage model (benzene covered particle), 4 sites (numbers in **bold** type) were explicitly modeled at a coverage of about one C₆H_x molecule per four Pt atoms as shown in Figure 3.5, all high coverage energies were then standardized (numbers in *Italic* type) by fitting high coverage energies linearly as in Figures 3.12 and 3.13 to the low coverage energies based on the 7 explicitly calculated high coverage cases on truncated cubo-octahedral particles including cases on (100) facet of Pt₅₈₆ in Table 3.3.

‡ Prefactor for desorption = 10¹⁵ s⁻¹; prefactor for dehydrogenation = 10¹³ s⁻¹; T = 500 K.

Table 3.3 DFT-calculated desorption energies, C-H activation energies and reaction rates for desorption and dehydrogenation reactions of cyclohexene with low coverage and high coverage at various surface sites on (100) facet of Pt₅₈₆ particle (modeled by top 4 layers).

Pt ₅₈₆ particle (100) facet		Cyclohexene desorption energy E _{des} (kJ mol ⁻¹)		Cyclohexene C-H activation energy E _{act} (kJ mol ⁻¹)		Desorp. rate vs. dehydro. rate r_{des}/r_{act} ‡	
surface site*	site count**	low coverage	high coverage †	low coverage	high coverage †	low coverage	high coverage
1 (TT-T)	(m-3) ² ×4	90.7	66.3 <i>64.7</i>	49.7	55.4 <i>57.6</i>	0.005	18.1
2 (TE-E)	(m-2)×2×4/2	94.0	62.0 <i>68.0</i>	40.7	46.0 <i>46.9</i>	0.000	0.62
3 (EE-T)	(m-3)×4+2×4/2	116.7	91.8 <i>90.9</i>	60.8	78.6 <i>70.8</i>	0.000	0.80
4 (EC-E)	2×4/2	112.9	<i>87.0</i>	56.5	<i>65.7</i>	0.000	0.59
5 (TT-E)	(m-3)×4+2×4/2	88.5	<i>62.5</i>	46.0	<i>53.3</i>	0.004	10.9
6 (ET-T)	(m-4)×2×4/2+2×4/2	93.5	<i>67.5</i>	47.4	<i>54.9</i>	0.002	4.78

* surface sites see Figure 3.4b. (XY-Z) denotes a triangular 3-atom surface site ensemble comprised of two Pt sites involved in the di-σ adsorption of cyclohexene and one Pt site for the activation of the C-H bond. (T - terrace site; E - edge site; C - corner site)

** m is the number of atoms lying on an equivalent edge (corner atoms included, and $m=4$ for Pt₅₈₆)

† For the high coverage model (benzene covered particle), 3 sites (numbers in **bold** type) were explicitly modeled at a coverage of about one C₆H_x molecule per four Pt atoms as shown in Figure 3.6, all high coverage energies were then standardized (numbers in *Italic* type) by fitting high coverage energies linearly as in Figures 3.12 and 3.13 to the low coverage energies based on the 7 explicitly calculated high coverage cases on truncated cubo-octahedral particles including cases on (111) facet of Pt₂₀₁ in Table 3.2.

‡ Prefactor for desorption = 10¹⁵ s⁻¹; prefactor for dehydrogenation = 10¹³ s⁻¹; T = 500 K.

Table 3.4 DFT-calculated desorption energies, C-H activation energies and reaction rates for desorption and dehydrogenation reactions of cyclohexene with low coverage and high coverage at various surface sites on (111) and (100) facets of Pt₅₅ particle.

Pt ₅₅ particle		Cyclohexene desorption energy E _{des} (kJ mol ⁻¹)		Cyclohexene C-H activation energy E _{act} (kJ mol ⁻¹)		Desorp. rate vs. dehydro. rate r_{des}/r_{act} ‡	
surface site*	site count	low coverage	high coverage †	low coverage	high coverage †	low coverage	high coverage
(111)-1 (EC-E)	6	126.9	110.3 <i>101.1</i>	34.4	45.4 <i>39.5</i>	0.000	0.00
(111)-2 (EE-E)	3	78.2	<i>52.0</i>	44.3	<i>51.2</i>	0.029	81.9
(111)-3 (EE-C)	3	86.2	<i>60.1</i>	10.9	<i>11.5</i>	0.000	0.00
(100)-1 (CE-T)	4	124.8	<i>99.0</i>	52.6	<i>61.1</i>	0.000	0.01
(100)-2 (ET-E)	4	119.8	<i>94.0</i>	59.8	<i>69.7</i>	0.000	0.28
(100)-3 (EC-E)	4	126.7	<i>101.0</i>	54.2	<i>62.9</i>	0.000	0.01
(100)-4 (TE-C)	4	126.4	<i>100.6</i>	34.0	<i>39.0</i>	0.000	0.00

* surface sites see Figure 3.4c. (XY-Z) denotes a triangular 3-atom surface site ensemble comprised of two Pt sites involved in the di- σ adsorption of cyclohexene and one Pt site for the activation of the C-H bond. (T - terrace site; E - edge site; C - corner site)

** m is the number of atoms lying on an equivalent edge (corner atoms included)

† For the high coverage model (benzene covered particle), 1 site (numbers in **bold** type) was explicitly modeled at a coverage of about one C₆H_x molecule per four Pt atoms as shown in Figure 3.6, all high coverage energies were then standardized (numbers in *italic* type) by fitting high coverage energies linearly as in Figures 3.12 and 3.13 to the low coverage energies based on the 7 explicitly calculated high coverage cases on truncated cubo-octahedral particles (see Tables 3.2 and 3.3).

‡ Prefactor for desorption = 10¹⁵ s⁻¹; prefactor for dehydrogenation = 10¹³ s⁻¹; T = 500 K.

3.3.3 Selectivity of cyclohexane dehydrogenation

In order to provide a more direct comparison with the experimental results, we calculated the selectivity, i.e. the rate of cyclohexene desorption versus the rate of cyclohexene dehydrogenation $r_{des} / (r_{des} + r_{act})$, as a function of specific Pt particle size by multiplying the number average weights (n_i) for N types of sites with specific coordination environment (i.e. corner, edge, (111) terrace, (100) terrace) by their intrinsic rates for desorption (r_i^{des}) and intrinsic rates for C-H activation (r_i^{act}) as shown in the following equation:

$$selectivity = \frac{r_{des}}{r_{des} + r_{act}} = \frac{\sum_{i=1}^N n_i r_i^{des}}{\sum_{i=1}^N n_i r_i^{des} + \sum_{i=1}^N n_i r_i^{act}}. \quad (3.17)$$

We calculated the rates at the 12 different representative surface sites on truncated cubo-octahedral particles (Tables 3.2 and 3.3) and we calculated the numbers of these surface sites on various sizes of particles as illustrated in Table 3.5. The selectivity of cyclohexene reactions can be scaled up from Pt₂₀₁ to larger truncated cubo-octahedral particles (Figure 3.7) by assuming that the intrinsic adsorption energies and activation barriers for the different surface species at Pt sites with the identical coordination numbers do not change as we change particle sizes. This assumption may not hold as one moves to Pt clusters less than about 50 atoms [34] as there are distinct changes in the electronic structure for clusters of this size. We therefore extrapolate the curve for particles less than Pt₂₀₁ by a dashed line. To ensure the consistency of the results for the Pt₅₅ clusters we explicitly calculated these on the Pt₅₅ atom cluster to compare with the values extrapolated from the larger cluster.

The selectivity of cyclohexene from the dehydrogenation of cyclohexane was calculated from the DFT simulations to be 0.682 on the 1.8 nm Pt₂₀₁ particle and 0.007 on the 1.2 nm Pt₅₅ at high C₆H_x surface coverages. These results are in very good agreement with experimental results [9] which report selectivities for the formation of cyclohexene of 0.667 and 0.030 on the 2.2 and 1.3 nm average Pt particle sizes, respectively. There appears to be a distinct cross-over in product selectivities as shown in Figure 3.7, where particles smaller than ~1.5 nm result in higher selectivities to cyclohexadiene and benzene, whereas particles larger than ~1.5 nm result in higher selectivities to cyclohexene.

Table 3.5 Distribution of different surface sites for various size truncated cubo-octahedral Pt particles.

Truncated cubo-octahedron <i>m</i> value *	Average Diameter (nm)	Particle Size (atoms)	Number of Sites											
			(111) terrace †						(100) terrace ‡					
			1	2	3	4	5	6	1	2	3	4	5	6
3	1.8	201	18	12	12	12	6	12	0	4	4	4	4	0
4	2.6	586	72	18	24	24	12	12	4	8	8	4	8	4
5	3.3	1289	162	24	36	36	18	12	16	12	12	4	12	8
6	4.1	2406	288	30	48	48	24	12	36	16	16	4	16	12
7	4.9	4033	450	36	60	60	30	12	64	20	20	4	20	16
8	5.7	6266	648	42	72	72	36	12	100	24	24	4	24	20
9	6.4	9201	882	48	84	84	42	12	144	28	28	4	28	24
10	7.2	12934	1152	54	96	96	48	12	196	32	32	4	32	28
...

* *m* is the number of atoms lying on an equivalent edge (corner atoms included)

† Site numbers are as assigned in Figure 3.4a, site count formulas can be found in Table 3.2

‡ Site numbers are as assigned in Figure 3.4b, site count formulas can be found in Table 3.3

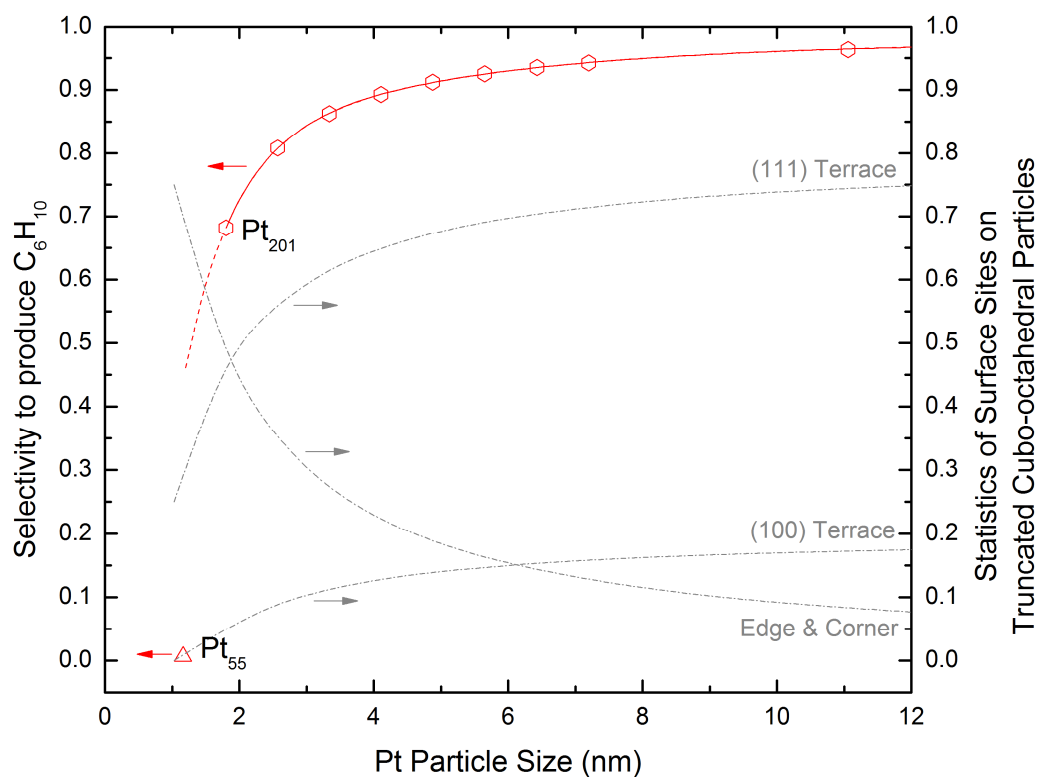


Figure 3.7 DFT-derived selectivity to cyclohexene vs. Pt nanoparticle size. The selectivity is calculated as $r_{\text{des}} / (r_{\text{des}} + r_{\text{act}})$ of cyclohexene surface intermediates. Grey curves indicate the fraction of surfaces atoms with different coordination numbers on truncated cubo-octahedral Pt particles.

3.4 Summary

First-principles density functional theoretical calculations carried out over well-defined cubo-octahedral Pt particles clearly demonstrate a direct dependence of selectivity in cyclohexane dehydrogenation with Pt particle size. The reaction energy diagram for the sequential activation of C-H bonds involved in the dehydrogenation of cyclohexane over Pt₅₅ is clearly lower in energy than the path for the dehydrogenation of cyclohexane over Pt₂₀₁ particle thus indicating that the dehydrogenation occurs much more rapidly for these strongly bound C₆H_x species on Pt₅₅ than over the more weakly held C₆H_x species on the Pt₂₀₁ particles. The calculation of collective rates of cyclohexene dehydrogenation and desorption reactions at different surface sites all over a truncated cubo-octahedral particle with high surface coverage shows smaller particles favor cyclohexene dehydrogenation towards benzene while larger particles favor desorption of cyclohexene. The size effect is especially significant when the particle size is within a few nanometers.

Supplementary Materials

The initial calculations were carried out on a cubo-octahedral Pt₅₅ cluster anchored at a defect site within the outer wall of the CNT(8,8) as is shown in Figure 3.10a to provide a representative model of supported Pt clusters. The same calculations were also carried out over the unsupported Pt₅₅ cluster in order to establish the effects of the support. The adsorption energies, activation barriers and the reaction energies were calculated for the series of elementary C-H bond activation steps for the model reaction of propane to propylene on the (111) and (100) terrace, edge and corner sites on the supported and unsupported Pt₅₅ clusters. The results shown in Figure 3.11 indicate that the differences between the supported and unsupported cluster are very small (generally < 10%). The only exceptions are for the Pt sites near the Pt-C interface, where the propane C-H bond activation energy is about 10 kJ mol⁻¹ (35%) higher. This is likely due to steric hindrance at the Pt center from the CNT support and charge transfer that occurs from the CNT to the Pt. The latter is consistent with the results from a Bader [35] charge analysis which shows 0.14 electrons are transferred from defect CNT support to the Pt₅₅ cluster. The changes that occur upon anchoring the Pt₅₅ cluster to the inside wall of the defect CNT(14,14) were also analyzed for comparison with those where Pt is anchored outside. Bader charge analysis results shown in Figure 3.10b indicate that 0.4 electrons are transferred from the support to the Pt₅₅ cluster inside which is slightly higher than 0.14 electrons when Pt₅₅ is anchored outside of the CNT. The increase in charge transfer results in a higher barrier to activate the C-H bond. This is consistent with recent experimental and other theoretical results that suggest that the clusters inside of nanotubes are less reactive than those outside [36-38] and results that show that small negatively charged Pt clusters are less active than neutral

clusters in C-H bond activation of methane [39]. Since the reactivity of the Pt clusters inside of the CNT is lower than those anchored to the outside and since the difference between the externally supported and unsupported Pt clusters were very small, we simplified all of the subsequent calculations and analyzed only the unsupported Pt clusters. In addition, we extend the initial model computational studies on the activation of propane to the dehydrogenation of cyclohexane.

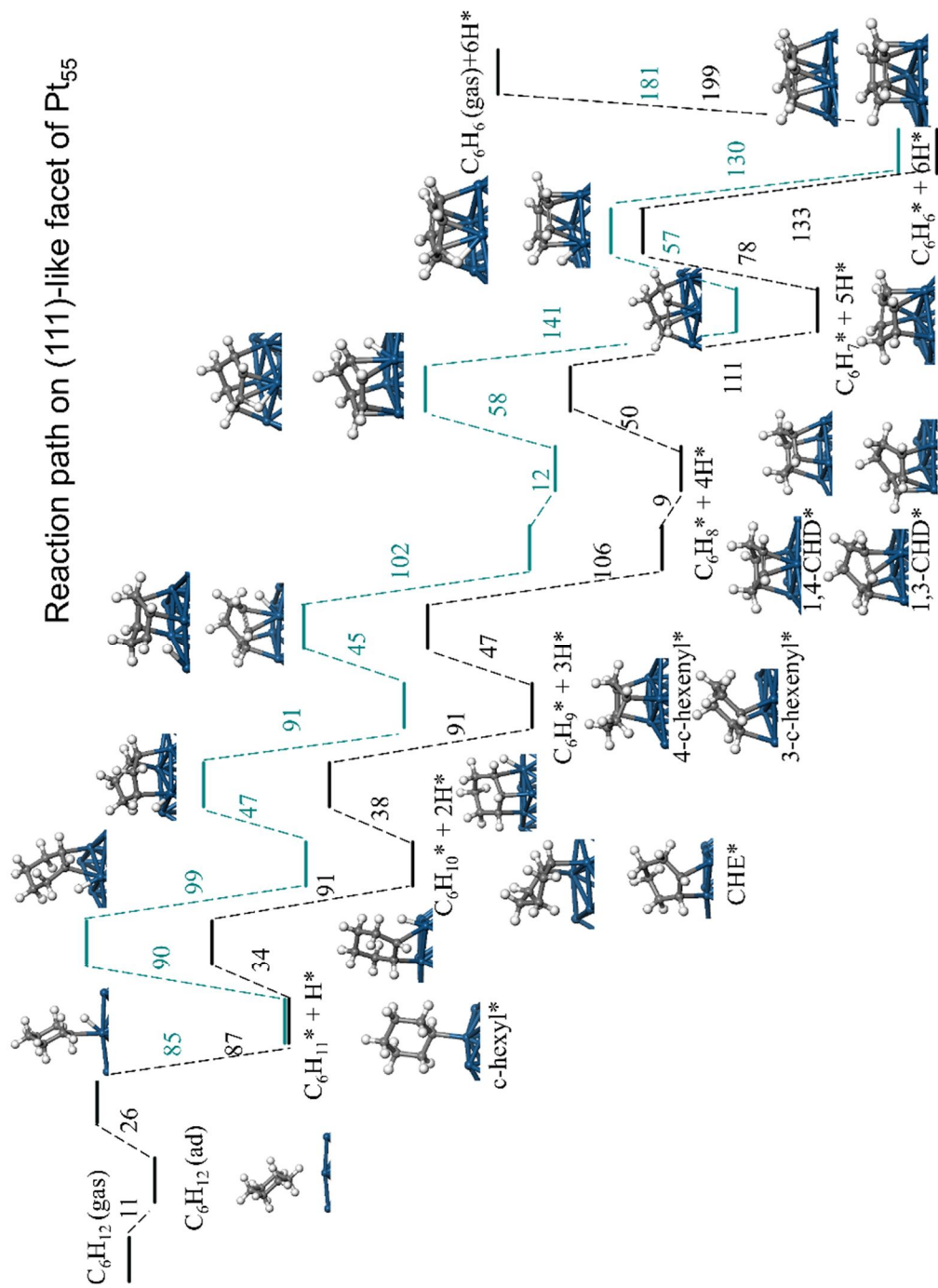


Figure 3.8 DFT calculated potential energy diagram for cyclohexane sequential dehydrogenation over (111)-like facet of Pt₅₅ cluster. (Energy / kJ mol⁻¹)

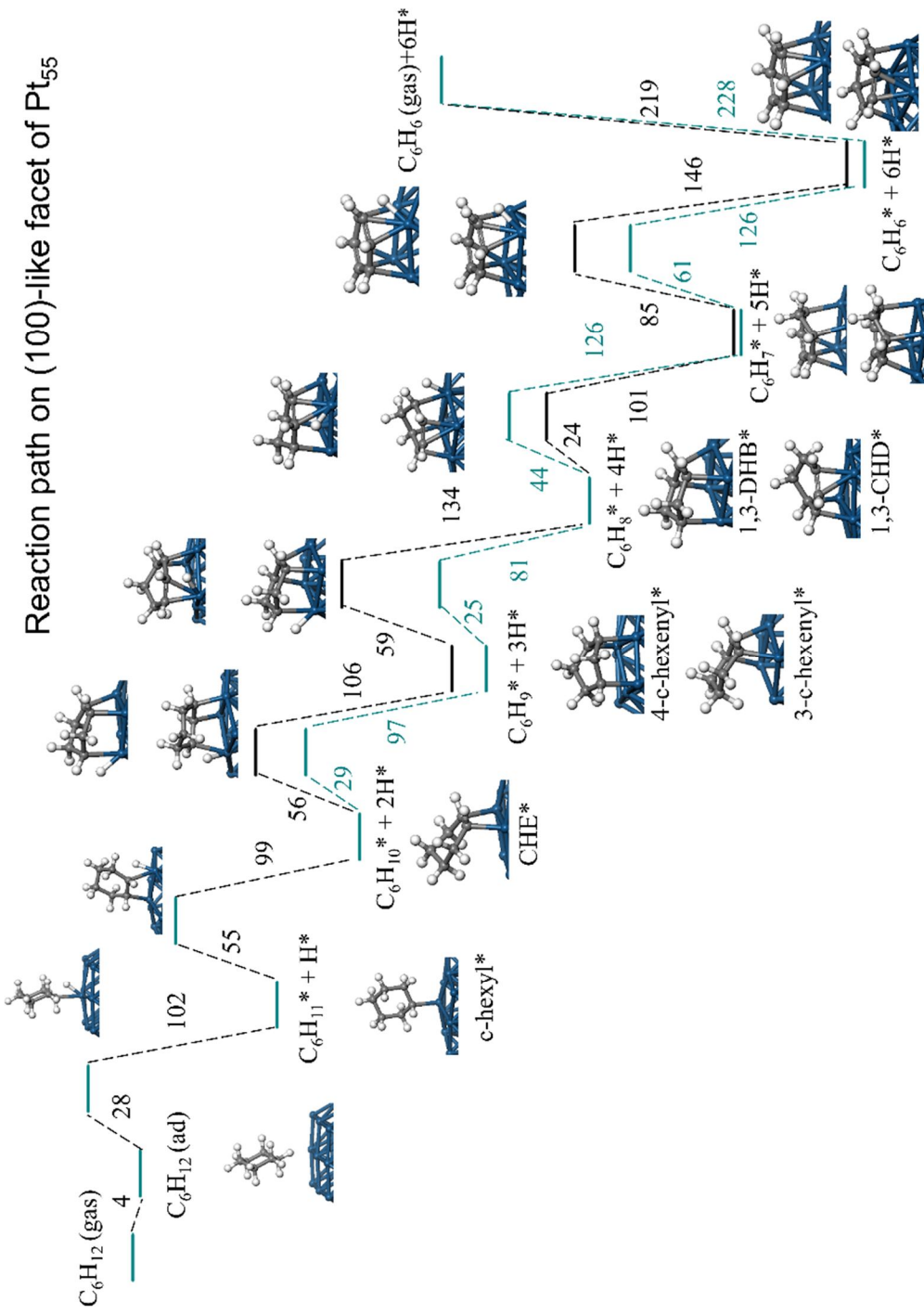


Figure 3.9 DFT calculated potential energy diagram for cyclohexane sequential dehydrogenation over (100)-like facet of bare Pt₅₅ cluster. (Energy / kJ mol⁻¹)

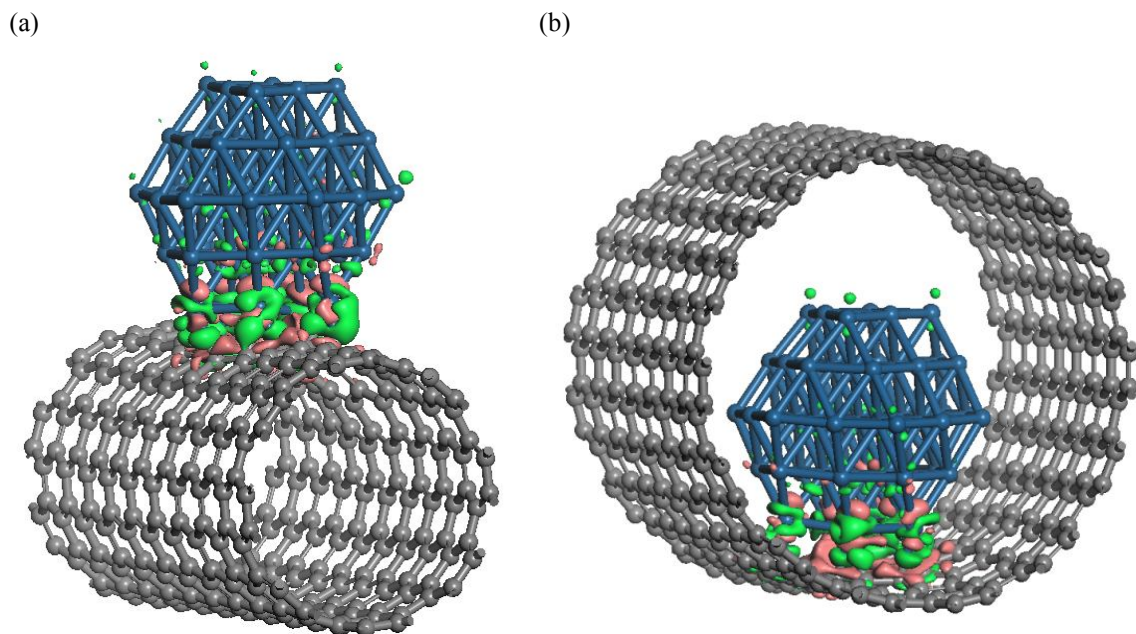


Figure 3.10 The charge density difference maps for the Pt_{55} cluster bound: (a) outside of the CNT(8,8) with a carbon defect and (b) inside a CNT(14,14) with a carbon defect for isovalues of $\pm 0.02 e/\text{\AA}^3$. The green color denotes an accumulation of electron density whereas the red color denotes depletion of electron density, with respect to the free-standing Pt particle and CNT.

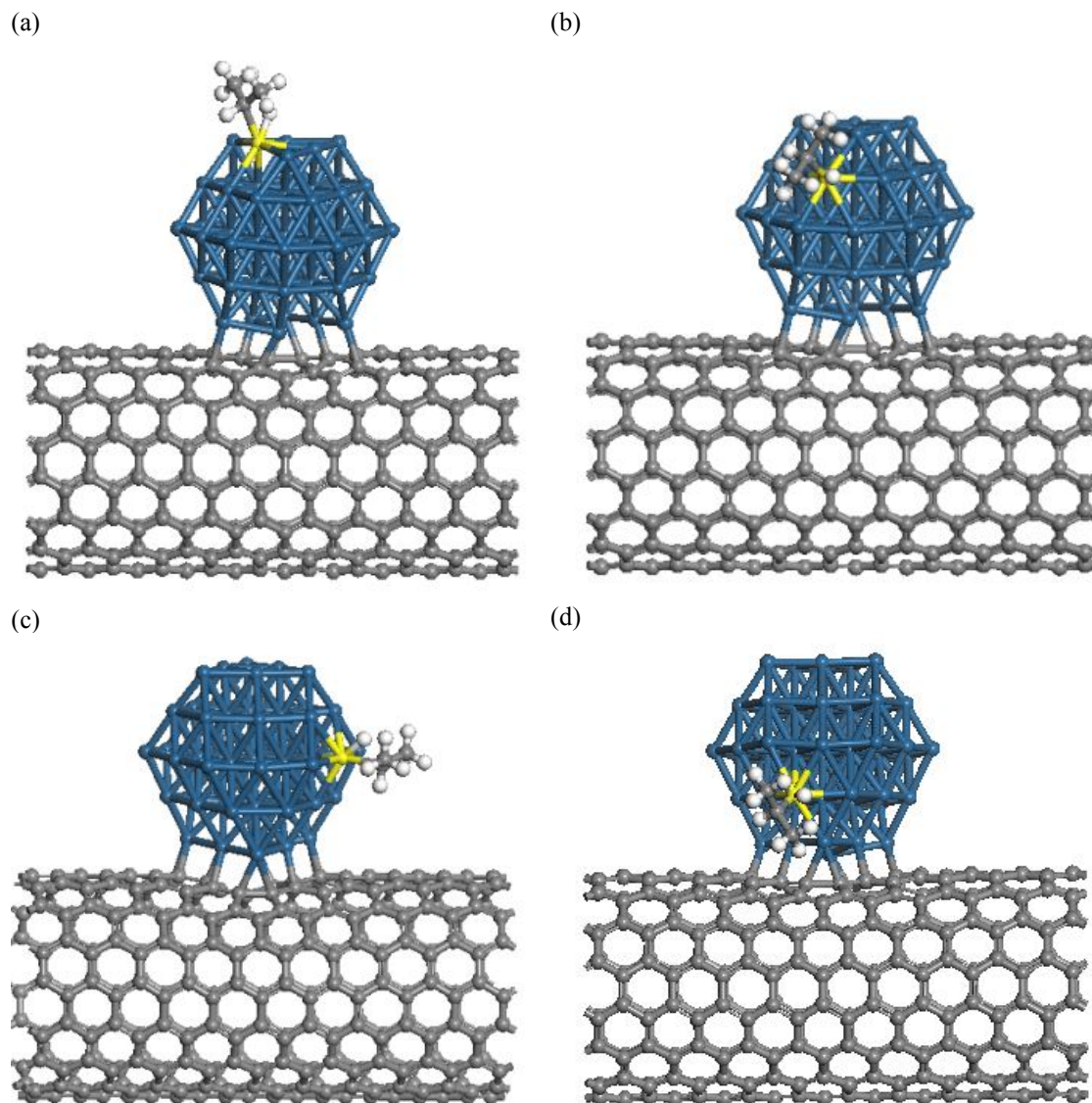


Figure 3.11 C-H bond activation of propane at different edge sites of Pt₅₅ supported on the outside wall of CNT(8,8) with defects. (a) edge site at Layer 1, $E_{\text{act}} = 33 \text{ kJ mol}^{-1}$; (b) edge site at Layer 2, $E_{\text{act}} = 29 \text{ kJ mol}^{-1}$; (c) edge site at Layer 3, $E_{\text{act}} = 31 \text{ kJ mol}^{-1}$; (d) edge site at Layer 4, $E_{\text{act}} = 40 \text{ kJ mol}^{-1}$. (The propane activation energy at an edge site of a free-standing Pt₅₅ cluster is 30 kJ mol^{-1} .)

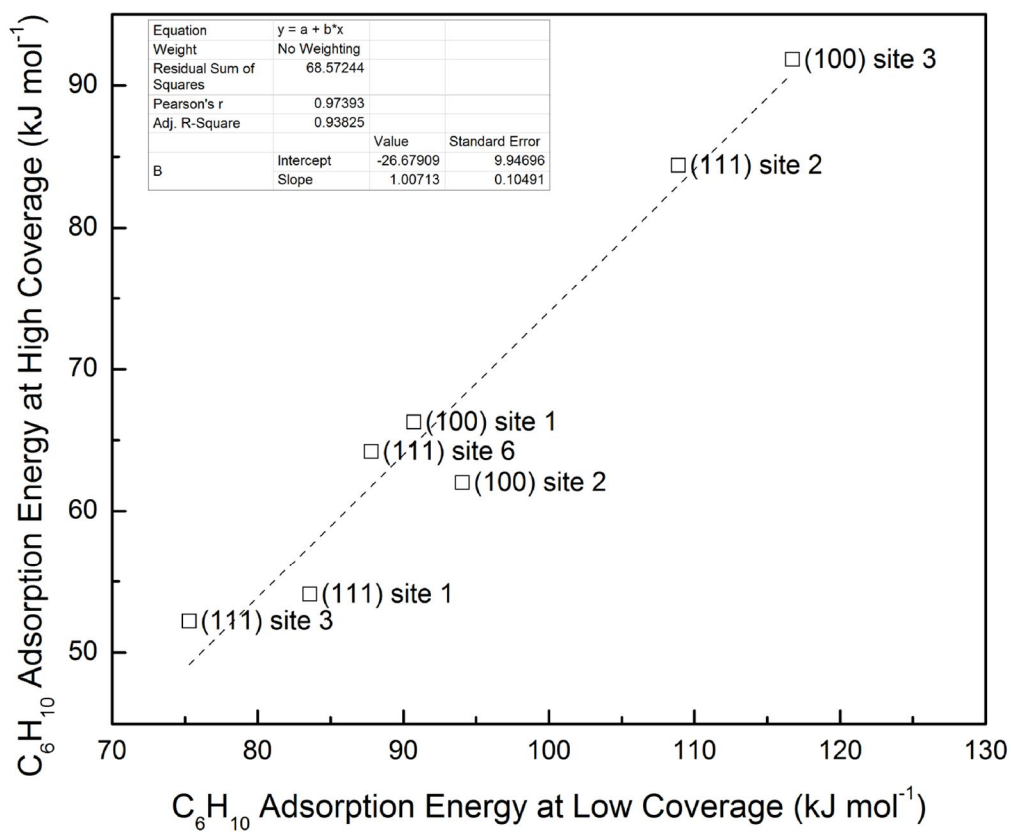


Figure 3.12 Cyclohexene adsorption energy at high surface coverage vs. the adsorption energy on same site at low surface coverage over truncated cubo-octahedral Pt particles. The high coverage scenarios are simulated by surrounding cyclohexene with benzene at a coverage of about one C_6H_x molecule per four Pt atoms. The low coverage scenarios are simulated by adsorption of cyclohexene on a bare Pt particle. Linear prediction was used to further standardize all the high coverage adsorption energy.

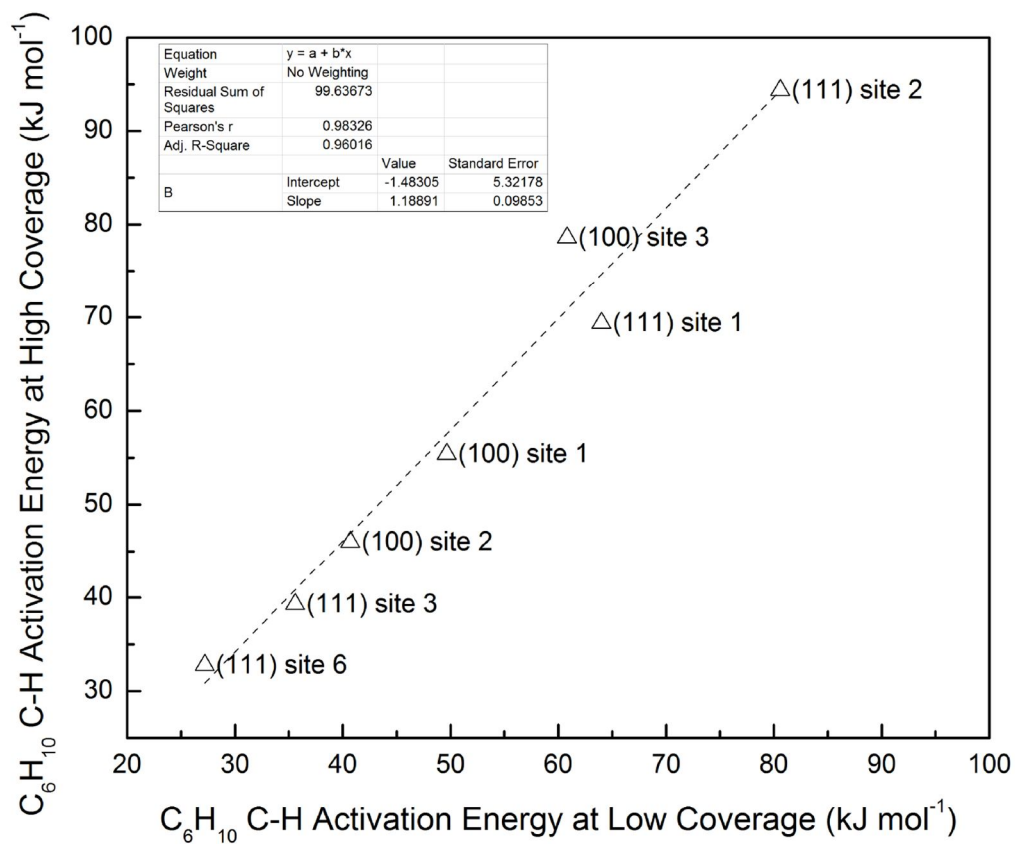


Figure 3.13 Cyclohexene C-H bond activation energy at high surface coverage vs. the activation energy on same site at low surface coverage over truncated cubo-octahedral Pt particles. The high coverage scenarios are simulated by surrounding cyclohexene with benzene at a coverage of about one C₆H_x molecule per four Pt atoms. The low coverage scenarios are simulated on a bare Pt particle. Linear prediction was used to further standardize all the high coverage C-H activation energy.

References

1. S. Vajda, M.J. Pellin, J.P. Greeley, C.L. Marshall, L.A. Curtiss, G.A. Ballentine, J.W. Elam, S. Catillon-Mucherie, P.C. Redfern, F. Mehmood, and P. Zapol, *Subnanometre platinum clusters as highly active and selective catalysts for the oxidative dehydrogenation of propane*. *Nature Materials*, 2009. **8**(3): p. 213-216.
2. Y. Lei, F. Mehmood, S. Lee, J. Greeley, B. Lee, S. Seifert, R.E. Winans, J.W. Elam, R.J. Meyer, P.C. Redfern, D. Teschner, R. Schlögl, M.J. Pellin, L.A. Curtiss, and S. Vajda, *Increased Silver Activity for Direct Propylene Epoxidation via Subnanometer Size Effects*. *Science*, 2010. **328**(5975): p. 224-228.
3. I.X. Green, W. Tang, M. Neurock, and J.T. Yates, *Spectroscopic Observation of Dual Catalytic Sites During Oxidation of CO on a Au/TiO₂ Catalyst*. *Science*, 2011. **333**(6043): p. 736-739.
4. R. Narayanan and M.A. El-Sayed, *Shape-Dependent Catalytic Activity of Platinum Nanoparticles in Colloidal Solution*. *Nano Letters*, 2004. **4**(7): p. 1343-1348.
5. F. Maillard, M. Eikerling, O.V. Cherstiouk, S. Schreier, E. Savinova, and U. Stimming, *Size effects on reactivity of Pt nanoparticles in CO monolayer oxidation: The role of surface mobility*. *Faraday Discussions*, 2004. **125**: p. 357-377.
6. D.C. Meier and D.W. Goodman, *The Influence of Metal Cluster Size on Adsorption Energies: CO Adsorbed on Au Clusters Supported on TiO₂*. *Journal of the American Chemical Society*, 2004. **126**(6): p. 1892-1899.
7. J.L. Carter, J.A. Cusumano, and J.H. Sinfelt, *Catalysis over Supported Metals. V. The Effect of Crystallite Size on the Catalytic Activity of Nickel*. *The Journal of Physical Chemistry*, 1966. **70**(7): p. 2257-2263.
8. K.J.J. Mayrhofer, B.B. Blizanac, M. Arenz, V.R. Stamenkovic, P.N. Ross, and N.M. Markovic, *The Impact of Geometric and Surface Electronic Properties of Pt-Catalysts on the Particle Size Effect in Electrocatalysis*. *The Journal of Physical Chemistry B*, 2005. **109**(30): p. 14433-14440.
9. S. Vajda, S. Lee, M. Di Vece, B. Lee, S. Seifert, R.E. Winans, G.A. Ferguson, L.A. Curtiss, J.P. Greeley, Q. Qian, M. Neurock, S. Goergen, R. Si, M. Stephanopoulos, X. Wang, G.L. Haller, and L.A. Pfefferle. *Size-and composition optimized sub-nanometer and nm size catalysts for low-temperature jet-fuel activation*. in *241st ACS National Meeting & Exposition*. 2011. Anaheim, CA: American Chemical Society.
10. W. G. Dukek, ed. *Kirk-Othmer Encyclopedia of Chemical Technology*. 1991, Wiley: New York.
11. D.W. Blakely and G.A. Somorjai, *Dehydrogenation and Hydrogenolysis of Cyclohexane and Cyclohexene on Stepped (High Miller Index) Platinum Surfaces*. *Journal of Catalysis*, 1976. **42**(2): p. 181-196.
12. M. Che and C.O. Bennett, *The Influence of Particle-Size on the Catalytic Properties of Supported Metals*. *Advances in Catalysis*, 1989. **36**: p. 55-172.
13. R.M. Rioux, B.B. Hsu, M.E. Grass, H. Song, and G.A. Somorjai, *Influence of Particle Size on Reaction Selectivity in Cyclohexene Hydrogenation and Dehydrogenation over Silica-Supported Monodisperse Pt Particles*. *Catalysis Letters*, 2008. **126**(1): p. 10-19.
14. G. Kresse and J. Hafner, *Ab initio molecular dynamics for liquid metals*. *Phys. Rev. B*, 1993. **47**: p. 558.
15. G. Kresse and J. Hafner, *Ab initio molecular-dynamics simulation of the liquid-metal-amorphous-semiconductor transition in germanium*. *Phys. Rev. B*, 1994. **49**: p. 14251.
16. G. Kresse and J. Furthmüller, *Efficiency of ab-initio total energy calculations for metals and semiconductors using a plane-wave basis set*. *Comput. Mat. Sci.*, 1996. **6**: p. 15.
17. G. Kresse and J. Furthmüller, *Efficient iterative schemes for ab initio total-energy calculations using a plane-wave basis set*. *Phys. Rev. B*, 1996. **54**: p. 11169.
18. J.P. Perdew, K. Burke, and M. Ernzerhof, *Generalized Gradient Approximation Made Simple*. *Phys. Rev. Lett.*, 1996. **77**: p. 3865.
19. J.P. Perdew, K. Burke, and M. Ernzerhof, *Erratum: Generalized Gradient Approximation Made Simple*. *Phys. Rev. Lett.*, 1997. **78**: p. 1396.
20. P.E. Blöchl, *Projector augmented-wave method*. *Phys. Rev. B*, 1994. **50**: p. 17953.

21. G. Kresse and D. Joubert, *From ultrasoft pseudopotentials to the projector augmented-wave method*. Phys. Rev. B, 1999. **59**: p. 1758.
22. H. Jónsson, G. Mills, and K.W. Jacobsen, *Nudged Elastic Band Method for Finding Minimum Energy Paths of Transitions*, in *Classical and Quantum Dynamics in Condensed Phase Simulations*, B.J. Berne, G. Ciccotti, and D.F. Coker, Editors. 1998, World Scientific. p. 385-404.
23. H. Graeme and J. Hannes, *A dimer method for finding saddle points on high dimensional potential surfaces using only first derivatives*. The Journal of Chemical Physics, 1999. **111**(15): p. 7010-7022.
24. O. Lytken, W. Lew, J.J.W. Harris, E.K. Vestergaard, J.M. Gottfried, and C.T. Campbell, *Energetics of Cyclohexene Adsorption and Reaction on Pt(111) by Low-Temperature Microcalorimetry*. Journal of the American Chemical Society, 2008. **130**(31): p. 10247-10257.
25. R. Van Hardeveld and F. Hartog, *The statistics of surface atoms and surface sites on metal crystals*. Surface Science, 1969. **15**(2): p. 189-230.
26. K.R. McCrea and G.A. Somorjai, *SFG-surface vibrational spectroscopy studies of structure sensitivity and insensitivity in catalytic reactions: cyclohexene dehydrogenation and ethylene hydrogenation on Pt (1 1 1) and Pt (1 0 0) crystal surfaces*. Journal of Molecular Catalysis A: Chemical, 2000. **163**(1-2): p. 43-53.
27. B. Poelsema, K. Lenz, and G. Comsa, *The dissociative adsorption of hydrogen on Pt(111): Actuation and acceleration by atomic defects*. Journal of Chemical Physics, 2011. **134**(7): p. 074703.
28. M.B. Hugenschmidt, A.L. Diaz, and C.T. Campbell, *Interaction of cyclohexadiene with platinum(111) studied by BPTDS and HREELS*. The Journal of Physical Chemistry, 1992. **96**(14): p. 5974-5978.
29. J.M. Campbell, S. Seimanides, and C.T. Campbell, *Probing ensemble effects in surface reactions. 2. Benzene adsorption on clean and bismuth-covered platinum(111)*. The Journal of Physical Chemistry, 1989. **93**(2): p. 815-826.
30. C.T. Campbell, J.M. Campbell, P.J. Dalton, F.C. Henn, J.A. Rodriguez, and S.G. Seimanides, *Probing ensemble effects in surface reactions. 1. Site-size requirements for the dehydrogenation of cyclic hydrocarbons on platinum(111) revealed by bismuth site blocking*. The Journal of Physical Chemistry, 1989. **93**(2): p. 806-814.
31. G.H. Vineyard, *Frequency factors and isotope effects in solid state rate processes*. Journal of Physics and Chemistry of Solids, 1957. **3**(1-2): p. 121-127.
32. C. Wert and C. Zener, *Interstitial Atomic Diffusion Coefficients*. Physical Review, 1949. **76**(8): p. 1169.
33. M. Boudart and G. Djega-Mariadassou, *Kinetics of Heterogeneous Catalytic Reactions*. 1984, Princeton, NJ: Princeton University Press.
34. A.H. Larsen, J. Kleis, K.S. Thygesen, J.K. Nørskov, and K.W. Jacobsen, *Electronic shell structure and chemisorption on gold nanoparticles*. Physical Review B, 2011. **84**(24): p. 245429.
35. G. Henkelman, A. Arnaldsson, and H. Jónsson, *A fast and robust algorithm for Bader decomposition of charge density*. Computational Materials Science, 2006. **36**(3): p. 354-360.
36. X. Pan and X. Bao, *The Effects of Confinement inside Carbon Nanotubes on Catalysis*. Accounts of Chemical Research, 2011. **44**(8): p. 553-562.
37. Z. Li, Z.-X. Chen, G.-J. Kang, and X. He, *Does confinement effect always enhance catalytic activity? A theoretical study of H₂ dissociation on CNT supported gold clusters*. Catalysis Today, 2011. **165**(1): p. 25-31.
38. D.H. Ess, R.J. Nielsen, W.A. Goddard III, and R.A. Periana, *Transition-State Charge Transfer Reveals Electrophilic, Ambiphilic, and Nucleophilic Carbon-Hydrogen Bond Activation*. Journal of the American Chemical Society, 2009. **131**(33): p. 11686-11688.
39. U. Achatz, C. Berg, S. Joos, B.S. Fox, M.K. Beyer, G. Niedner-Schatteburg, and V.E. Bondybey, *Methane activation by platinum cluster ions in the gas phase: effects of cluster charge on the Pt₄ tetramer*. Chemical Physics Letters, 2000. **320**(1-2): p. 53-58.

Chapter 4 Oxidative Dehydrogenation of Cyclohexane on Au/Co₃O₄

4.1 Introduction

The selective dehydrogenation and oxidation of cyclohexane are key steps in the production of adipic acid, a key intermediate in the synthesis of nylon [1]. The catalytic dehydrogenation of cyclohexane is also important in the commercial production of benzene via hydrocarbon reforming where significant amounts of cyclohexane that remain in the product stream as impurities must be removed [2]. Compared to non-oxidative dehydrogenation, oxidative dehydrogenation (ODH) has lower capital costs and higher operational efficiencies as the reaction temperature for ODH is lower than the non-oxidative dehydrogenation and decoking shutdowns are eliminated. Oxygen is often used as the co-reagent in the ODH to enhance dehydrogenation and regenerate surface oxygen species.

Cobalt oxide (Co₃O₄) is recognized as one of the most active catalysts for oxidation of light hydrocarbons [3], CO [4] and NO_x [5]. For example, it was found the rate of propene oxidation over a number of metal oxides follow the order [6]: AgO₂ > Co₃O₄ > CuO > MnO₂ > Cr₂O₃ > CdO > V₂O₅ > NiO > CeO₂ > Al₂O₃. Similarly, methane oxidation over various metal oxides [7] has different catalytic activity: Co₃O₄ > CuO > NiO > Mn₂O₃ > Cr₂O₃. The catalytic properties of Co₃O₄ are generally attributed to the weak metal-oxygen bond and the rapid oxygen exchange rates between gas phase and lattice oxygen [6, 8]. While Co₃O₄ alone is active in the oxidative dehydrogenation, the addition of Au nanometer particles has been shown to improve the activity in both selective and total

oxidation of hydrocarbons. For example, Au/Co₃O₄ was found to be active for catalytic oxidation of methane [9] at 250 °C, and ethylene [10] at 0 °C. In previous collaborative work with Vajda et al. [11] we showed that Co₃O₄ nanoparticles alone were active for the oxidative dehydrogenation of cyclohexane at 300 °C. In the present work, we examine the influence on catalytic activity by doping Co₃O₄ with Au nanoparticles.

For catalytic oxidation reactions, the metal oxide support plays an important role in the Au/metal-oxide system. Studies [12, 13] of different Au/metal-oxide catalysts with similar Au loadings (Au/TiO₂, Au/ZrO₂, Au/ZnO, Au/Al₂O₃) show that the catalytic activity for CO oxidation can be directly correlated with the oxygen storage capacity and the reducibility of the oxide support. The morphology of the metal oxide support can also significantly influence the catalytic oxidation activity. Au/Co₃O₄-nanorods were found to be catalytically more active than nanopolyhedra and nanocubes in ethylene complete oxidation [14].

Experimental studies carried out by our collaborators at Argonne National Laboratory and Tufts University have shown that Co₃O₄ is active in the oxidative dehydrogenation of cyclohexane [11]. By doping Co₃O₄ with Au they [15] were able to increase the catalytic activity by roughly an order of magnitude and form C₆H₆, C₆H₈, C₆H₁₀, and CO₂ products. In addition, the significant deactivation that occurred over the bare 12 nm Co₃O₄ particles alone was not observed for the Au doped 12 nm Co₃O₄ particles.

We carried out first-principles density functional theory calculations in order to elucidate the differences in the catalytic reactivity of Au/Co₃O₄ and pure Co₃O₄ surfaces. More specifically we examine in detail the activation barriers and the reaction energetics for C-H bond activation and O₂ activation, which both appear to readily proceed at the interfacial sites at the Au-Co₃O₄ interface. In addition, the Au-Co₃O₄ interface promotes oxygen vacancy formation and thus increases the reducibility of the oxide support. The computational results presented herein are in good agreement with the experimental observation that oxidative dehydrogenation of cyclohexane proceeds faster on Au/Co₃O₄ than on Co₃O₄.

4.2 Method

All the calculations reported herein were carried out by using density functional theory with correction for on-site Coulomb interactions (DFT+U) as implemented in Vienna *ab initio* Simulation Package (VASP) [16-20]. Spin-polarized generalized gradient approximation (SGGA) in the form of Perdew-Burke-Ernzerhof (PBE) [21, 22] was used to account for exchange and correlation effects. The Projector Augmented Wave method (PAW) [23, 24] was used to describe the electron-ion interaction. The kinetic-energy cutoff for plane wave basis set was fixed at 400 eV. Geometry optimizations were considered to be converged when the displacement forces on each of the atoms were less than 0.05 eV/Å. The Brillouin zones were sampled using the Γ -centered Monkhorst-Pack scheme [25]. The correction of on-site Coulomb repulsion in the form of Dudarev's rotational invariant approach [26] was applied to the Co 3*d* electrons. The Hubbard *U* term was set equal to 3 eV as it correctly predicts band gap of Co₃O₄ according to our electronic band structure calculations [11], where the computed band gap of 1.47 eV (Figure 4.1) is in good agreement with experimental observations of the direct optical transition at 1.44 - 1.52 eV [27-30]. An initial magnetic moment was specified for each atom to help the system converge to anti-ferromagnetic configuration for the Co₃O₄ support [31]. The minimum energy path (MEP) was calculated by the nudged elastic band (NEB) method [32] until the forces on each of the atom were less than 0.2 eV/Å. The two highest energy structures along the NEB path were subsequently used to further isolate the transition state with the Dimer method [33]. The transition states were located by the Dimer method until the forces were less than 0.05 eV/Å. All of the reaction energies and activation barriers for the initial

activation of cyclohexane were calculated with respect to gas phase cyclohexane as reference.

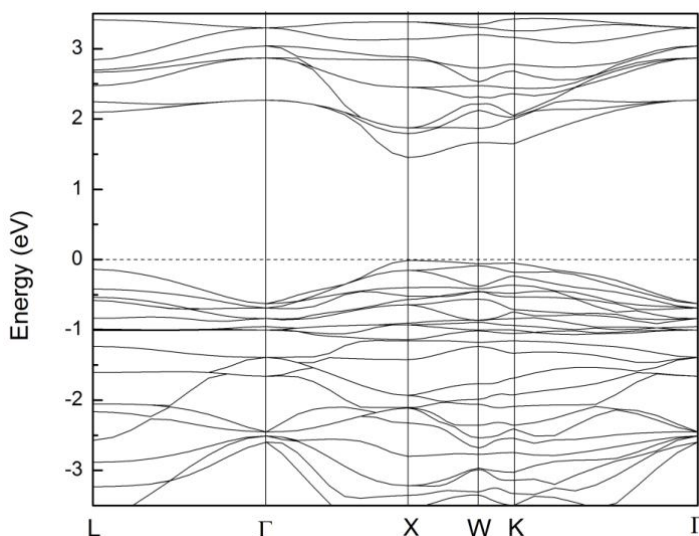


Figure 4.1 DFT+ U ($U=3$) calculated electronic band structure near the Fermi level of Co_3O_4 bulk structure along several high symmetry lines in the FCC Brillouin zone.

At room temperature, Co_3O_4 adopts a normal spinel structure $\text{A}[\text{B}_2]\text{O}_4$ (Figure 4.2a), with its tetrahedral sites (A) occupied by high-spin Co^{2+} (d^7) and octahedral sites (B) occupied by low-spin Co^{3+} (d^6) ions [34]. Natural Co_3O_4 predominantly exposes (111) and (110) surfaces [35]. Previous calculations [11, 36, 37] indicate Co_3O_4 (110) surface with Type B termination (Figure 4.2b) is thermodynamically most stable under moderate oxygen partial pressures and relatively more reactive than the (111) surface. Experiments of CH_4 [38] and CO [39] oxidation demonstrated that Co_3O_4 nanoparticles that predominantly expose (110) facets are more active than those that predominantly expose (111) facets under same reaction conditions. We therefore chose the Type B (110) surface of Co_3O_4 ($\text{Co}_3\text{O}_4(110)$ for short) as the model support for gold. Our first several trials show small Au nanoparticles significantly restructure on the oxide support, and expose a number of coordinatively

unsaturated Au atoms which will likely bias the calculations on catalytic reactivity. Instead of using these small Au nanoparticles, we adopt a more well-defined Au-nanorod model that has been used in other previous studies for Au/TiO₂ [40]. The model as presented in Figure 4.5a contains a 24-atom Au-nanorod in a periodic 2×2 supercell of a 5-atomic-layer Co₃O₄(110) slab model (using 3×3×1 **k**-point mesh, a=16.29 Å, b=11.52 Å, c=22.00 Å). The bottom two layers of the Co₃O₄ slab are fixed, while all other atoms are allowed to relax. The Au-Au distance (2.88 Å) in bulk gold is very close to the O-O distance (2.89 Å) on the Co₃O₄(110) surface, which leads to a good lattice alignment for this Au-nanorod/Co₃O₄ model. One- and two-atom Au clusters supported on 2×2 Co₃O₄(110) were also explored.

The charge density difference on the Co₃O₄ surface before and after Au deposition was calculated with the equation:

$$\rho_{diff} = \rho(\text{Au/Co}_3\text{O}_4) - \rho(\text{Co}_3\text{O}_4) - \rho(\text{Au}). \quad (4.1)$$

The oxygen vacancy formation energy was calculated using the equation:

$$E_f(\text{O-vacancy}) = E(\text{slab with O-vacancy}) + \frac{1}{2}E(\text{O}_2) - E(\text{slab}). \quad (4.2)$$

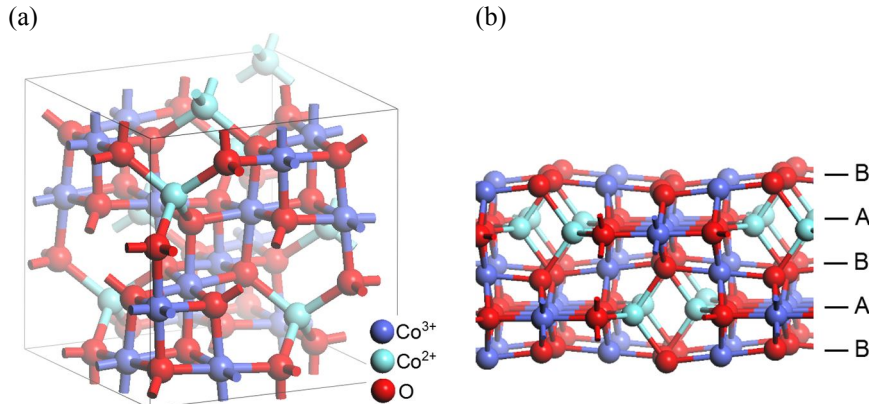


Figure 4.2 (a) Co₃O₄ normal spinel structure, (b) side view of Co₃O₄ (110) surface.

4.3 Results and Discussion

Our efforts are focused on the reactivity of sites on Au and Co_3O_4 at the Au- Co_3O_4 interface. A calculation of the complete catalytic cycle of alkane oxidative dehydrogenation to alkene over Co_3O_4 surfaces with a smaller unit cell can be found in our previous work [11]. In this study, we examine in detail several of the critical elementary steps and surface properties important in the activation of cyclohexane but do not examine all of the possible intermediates and reaction pathways. The calculations of initial C-H activation, O_2 activation, and oxygen vacancy formation, readily provide valuable insights into the mechanism and the influence of Au on the oxidative dehydrogenation reactivity on Au/ Co_3O_4 as compared to that on pure Co_3O_4 .

4.3.1 C-H bond activation of cyclohexane

The initial C-H bond activation is generally considered the rate-determining step in the activation and oxidation of most alkanes. This is supported by kinetic measurements [41], isotopic substitution experiments [42], and theoretical calculations [43-45]. Once the first C-H bond is activated, the subsequent reactions that produce alkenes, CO_2 and H_2O are thought to be relatively easy because of more favorable enthalpies and entropies [46]. The entropic penalty associated with the loss of translational and rotational degrees of freedom in initially activating gas phase alkane is typically quite high. The initial C-H bond activation of cyclohexane over Au/ Co_3O_4 can proceed via three different mechanisms including hydrogen abstraction by oxygen (O^*) sites or species, σ -bond metathesis over the $\text{Co}^*\text{-O}^*$ pairs, and oxidative addition on Au sites. The C-H activation of cyclohexane on Au sites are clearly unfavorable, as shown in Figure 4.3c, which has an activation barrier

as high as 105 kJ mol^{-1} . The equatorial C-H bond can also be activated over the Co^*-O^* site pairs to form the $\text{Co}^*-\text{C}_6\text{H}_{11}$ and O^*-H products via the reaction $\text{C}_6\text{H}_{12} + \text{Co}^*-\text{O}^* \rightarrow \text{Co}^*-\text{C}_6\text{H}_{11} + \text{O}^*-\text{H}$ over pure $\text{Co}_3\text{O}_4(110)$ surface as is shown in Figure 4.3a. The reaction proceeds via σ -bond metathesis with an activation barrier of 75 kJ mol^{-1} . The same reaction over the $\text{Co}^*-\text{O}^{2f*}$ pair on $\text{Au}/\text{Co}_3\text{O}_4(110)$ surface (Figure 4.3b) results in a very similar activation barrier (73 kJ mol^{-1}). The charge density difference map in Figure 4.5c shows little change in the electronic structures of the corresponding Co^* and O^{2f*} sites before or after the adsorption of Au nanorod as the $\text{Co}^*-\text{O}^{2f*}$ pair is not directly connected to perimeter sites of the $\text{Au}-\text{Co}_3\text{O}_4$ interface. These observations suggest that the influence of gold on Co_3O_4 would need to be more local and specifically involve O, Au or Co atoms directly at the interface.

The stronger bond between O-H over C-H makes it possible that the oxygen sites on the metal oxide directly abstract a hydrogen atom from the alkane to form an O-H bond and an weakly coordinated alkyl radical-like species in the transition state [47]. Hydrogen abstraction proceeds at the 2-fold lattice O^{2f*} sites of pure $\text{Co}_3\text{O}_4(110)$ surface via $\text{C}_6\text{H}_{12} + 2\text{O}^* \rightarrow \text{O}^*-\text{C}_6\text{H}_{11} + \text{O}^*-\text{H}$ as is shown in Figure 4.4a and results in an activation barrier of 36 kJ mol^{-1} . The radical-like C_6H_{11} species that formed in the transition state readily rebounds to a second oxygen at the surface as the reaction proceeds. Figure 4.4b and c present the same reactions on O^{2f*} sites at the $\text{Au}-\text{Co}_3\text{O}_4(110)$ interface; the difference is that in Figure 4.4c the H-abstracting O^{2f*} is on the perimeter of the $\text{Au}-\text{Co}_3\text{O}_4$ interface, which results in a slightly lower activation barrier (30 kJ mol^{-1}) for cyclohexane activation. Bader [48, 49] charge analysis indicates a net electron transfer from the Au nanorod to the

Co₃O₄ support. Increased electron density is observed on the Co³⁺ at the gold-metal oxide interface (Figure 4.5d), which weakens the Co-O^{2f} bond and thus increases the hydrogen affinity of the interfacial O^{2f*} site by 16 kJ mol⁻¹. We showed previously [11] that increases in hydrogen affinity of oxygen sites result in lower C-H bond activation barrier at this oxygen site.

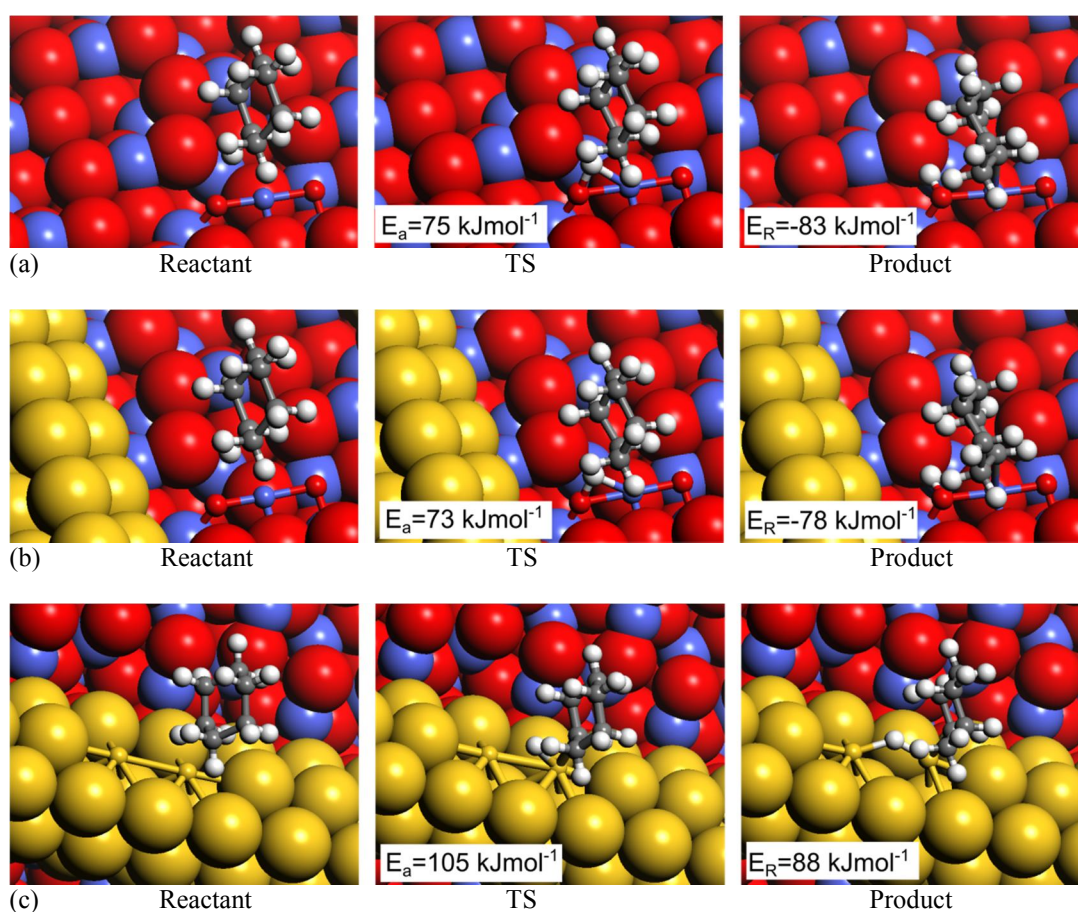


Figure 4.3 DFT-calculated reactant, transition and product state structures along with the activation energies and reaction energies for the initial C-H activation of cyclohexane at (a) Co^{*}-O^{2f*} pair on the bare Co₃O₄(110) surface, (b) Co^{*}-O^{2f*} pair on the Au/Co₃O₄ surface, and (c) Au site on the Au/Co₃O₄ surface.

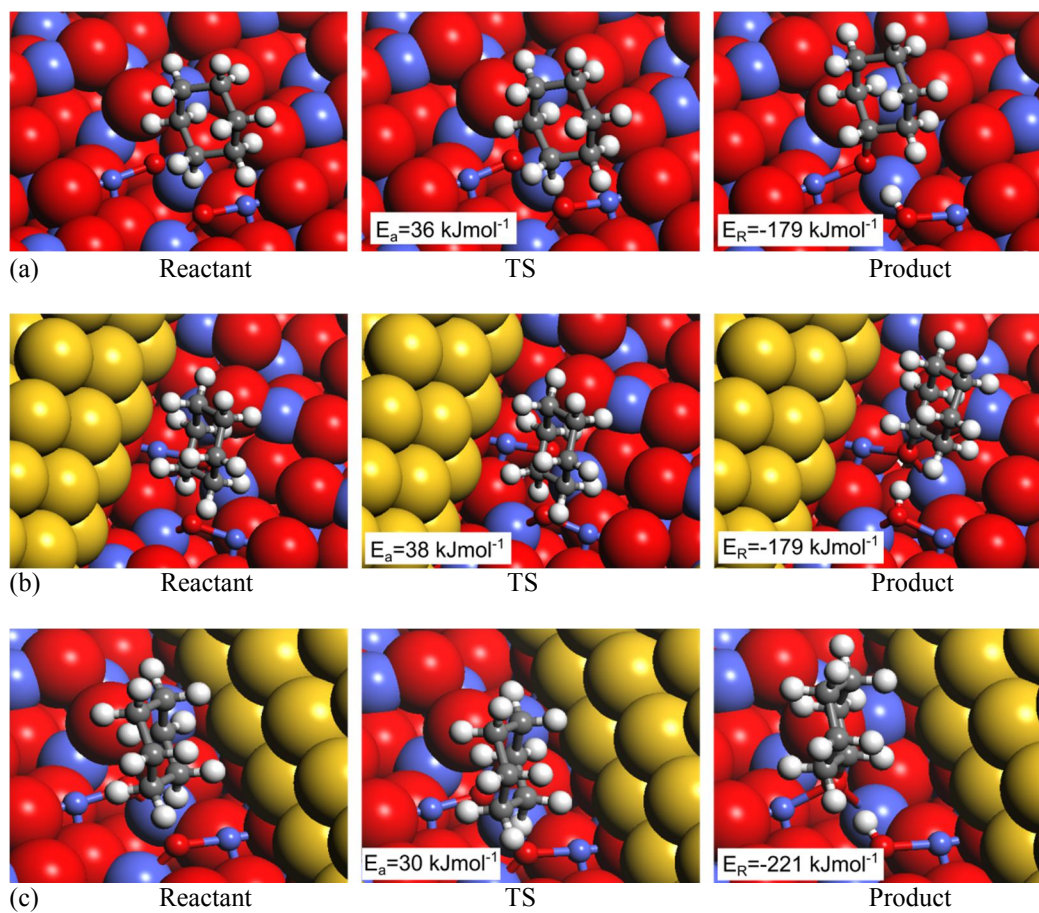


Figure 4.4 DFT-calculated reactant, transition and product state structures along with the activation energies and reaction energies for the initial C-H activation of cyclohexane at (a) O^{2f*} site on the bare $\text{Co}_3\text{O}_4(110)$ surface, (b) non-interfacial O^{2f*} site on the Au/ Co_3O_4 surface, and (c) O^{2f*} site near the Au/ Co_3O_4 interface.

4.3.2 O₂ activation

Many hydrocarbon and alkane oxidation reactions that occur on metal oxides tend to follow a Mars-van Krevelen-like (redox) mechanism, which involves the activation of hydrocarbon by lattice or surface oxygen, the formation of oxygenates, CO₂ and H₂O and the subsequent replenishment of surface oxygen species by the activation of O₂. The active lattice or surface oxygen that carries out C-H activation is ultimately removed via reaction and must be replenished via the activation of O₂. Three possible surface sites, including O^{2f}-vacancy site, Co-Au dual perimeter site and Au-Au site, are probed for the catalytic activity of O₂ adsorption and activation. The desorption of oxidation products leads to the formation of surface oxygen vacancies, among which the O^{2f}-vacancy is likely the most abundant compared to O^{3f}-vacancies. The removal of a 2-fold O^{2f} lattice oxygen exposes a surface Co^{octa} site and a sublayer Co^{tetr} site. The O₂ molecule exothermically adsorbs in the vacancy and dissociates at the Co^{octa} site, thus regenerating the O^{2f} lattice oxygen site and providing a surface oxygen anion (Figure 4.6a and b). The activation of O₂ at the perimeter Co^{octa} site of Au-Co₃O₄ interface (19 kJ mol⁻¹) occurs much more readily than the activation of O₂ at the non-interfacial Co^{octa} site (40 kJ mol⁻¹). The activation of O₂ molecule at oxide surface requires the alignment of unoccupied molecular orbitals of O₂ with the top of valence band, from where electron density can be transferred into the activated O₂ state [50]. Bader charge analyses show that the increased electron density at the interfacial Co^{octa} site upon the addition of the Au nanorod, which can be donated to the anti-bonding orbitals of O₂ molecule in favor of its dissociation. Direct O₂ activation at Au sites, however, does not appear to occur as the barrier is too high. It requires an energy barrier of 94 kJ mol⁻¹ to

dissociate O_2 molecule on the edge sites of the Au nanorod; and an energy barrier of 130 kJ mol^{-1} on a Co-Au dual perimeter site.

The theoretical results presented here in Figure 4.6 indicate that O_2 activation occurs much more readily at the vacancy sites of metal oxide surface rather than on the Au nanoparticle. This is consistent with previous experimental observations. Isotopic studies show that O_2 adsorb molecularly on Au particle of (2.9 nm) Au/ Fe_2O_3 (298 K) [51], (2-3 nm) Au/ TiO_2 (353 K) [52], and (3.5 nm) Au/ Al_2O_3 (300 K) [53].

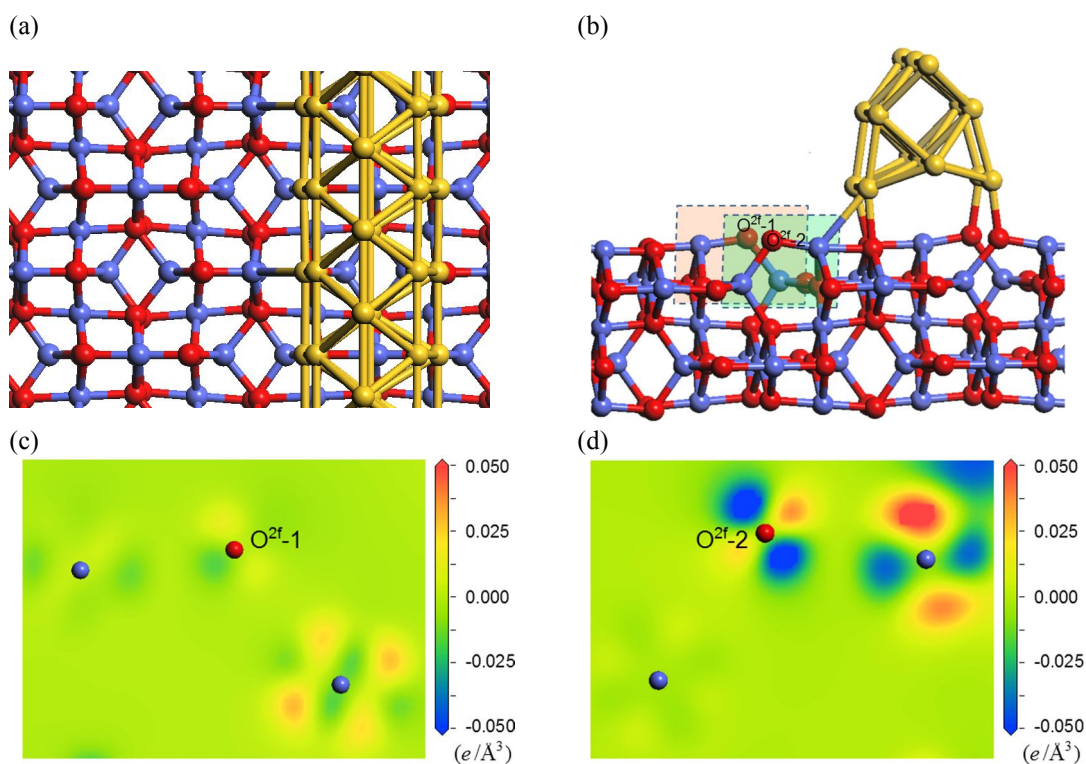


Figure 4.5 DFT-calculated charge analysis for the Au/ Co_3O_4 . (a) The top view of the Au/ Co_3O_4 (110) model, (b) side view of the Au/ Co_3O_4 (110) model, and (c,d) local charge density difference maps of the Co_3O_4 support before and after Au deposition. (c) is corresponding to the red slice in (b), and (d) is corresponding to the green slice in (b). Blue region denotes accumulation of negative charge (electron) densities.

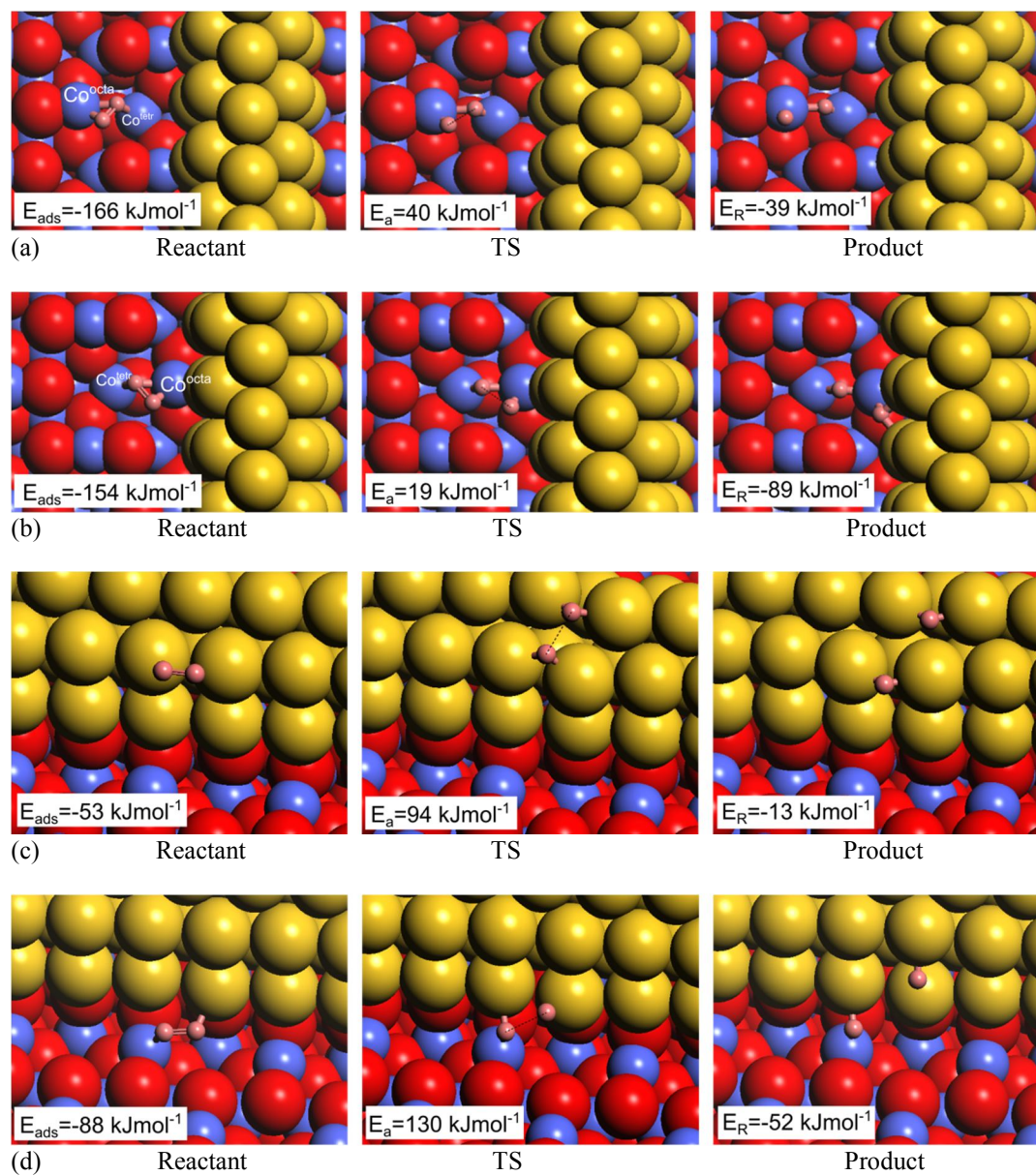


Figure 4.6 O_2 dissociation at (a) non-interfacial $\text{O}^{2\text{f}}$ -vacancy, (b) interfacial $\text{O}^{2\text{f}}$ -vacancy, (c) edge sites of Au nanorod, and (d) Co-Au dual perimeter site.

4.3.3 Reducibility of the oxide surface

The desorption of H₂O, CO₂ and other oxygenate products that form likely involve the removal of lattice oxygen [11]. The desorption energy of these molecules can therefore be correlated to the reducibility of the metal oxide catalyst. Previous experimental studies suggest that the increased oxidative dehydrogenation reactivity of an oxide in the presence of Au is ascribed to the improved reducibility of the oxide support, rather than the catalytic activity of gold particles themselves. Oxygen temperature-programmed desorption (O₂-TPD) profiles [10, 14, 54] show that Au/Co₃O₄ sample has more surface-active oxygen species than Co₃O₄ sample. Temperature programmed reduction (H₂-TPR) of Co₃O₄ and Au/Co₃O₄ show that the bands that arise from reduction are shifted towards lower temperatures, which indicate improved reducibility of Co₃O₄ in the presence of Au [55, 56], assuming that the Au particles themselves are inert to H₂ dissociation. It is still under debate whether this shift in the reduction band is due to H spillover or weakened metal-oxygen bonds. CO-TPR reactions carried out over CeO₂ also demonstrate improved reducibility in the presence of Au. Electronic charge redistribution between Au cluster and ceria is thought to weaken the Ce-O bond [57]. More detailed temporal analysis of products (TAP) studies of CO oxidation over CuMnO_x and Au/CuMnO_x [58] indicate that gold-doping promotes the Mars van Krevelen routes of reaction by increasing the amount of active surface O* sites.

Herein we use oxygen vacancy formation energy as a descriptor of the reducibility of the oxide. The results are summarized in Table 4.1. We are able to show that the binding of the Au nanorod to the Co₃O₄(110) surface reduced the binding energy of the interfacial lattice

oxygen (O^{2f}) sites thus making them easier to remove. The 2-fold interfacial oxygen vacancy formation energy was found to decrease from 161 kJ mol⁻¹ on the Au-nanorod to 160 kJ mol⁻¹ on Au₂ and 150 kJ mol⁻¹ on Au₁ supported on Co₃O₄(110) as reported in Table 4.1 and shown in Figure 4.7. These values are all lower than the vacancy energies reported on the bare Co₃O₄(110) surfaces (173 kJ mol⁻¹) thus pointing to the improved reducibility of the Co₃O₄ in the presence of Au.

Table 4.1 DFT-calculated 2-fold surface lattice oxygen vacancy formation energies (kJ mol⁻¹) for Co₃O₄(110), Au-nanorod/Co₃O₄(110), and Au_n/Co₃O₄(110) n=1,2 (oxygen sites are labeled as in Figure 4.7)

2-fold lattice oxygen O^{2f}	O-vacancy formation energy (kJ mol ⁻¹)
O^{2f} on bare Co ₃ O ₄ (110)	173
$O^{2f}(Au_{rod})$	161
$O^{2f}(Au_1)$	150
$O^{2f}(Au_2)$	160

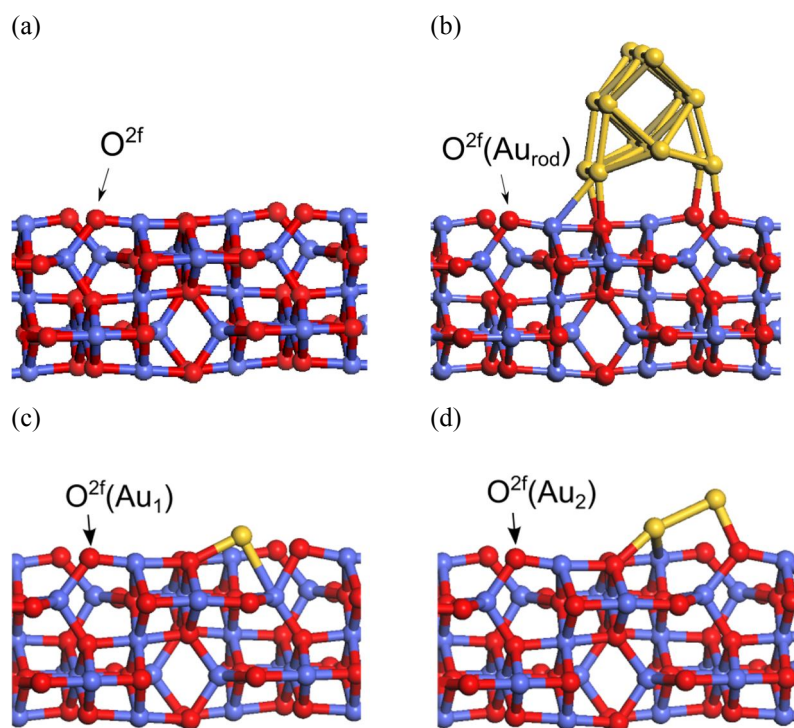


Figure 4.7 DFT-optimized structures of (a) bare Co₃O₄(110) surface and (b) Au-nanorod, (c) Au₁ and (d) Au₂ on the Co₃O₄(110) surface.

4.4 Summary

Density functional theory calculations have been carried out to compare the catalytic activity of Au/Co₃O₄ with that of pure Co₃O₄ surfaces. The Au nanoparticle transfers electrons to the Co₃O₄ support upon its adsorption and the charge is localized near the gold-oxide interface. The increased electron density at the interfacial Co^{octa} cations weakens the Co-O bond and increases the hydrogen affinity of the O site. This increase in hydrogen affinity in interfacial O site result in a lower activation barrier for the initial C-H bond activation of cyclohexane at Au-Co₃O₄ interface. The partially reduced Co^{octa} cation at the interfacial O-vacancy also enhances the binding and dissociation of molecular O₂ at this site thus resulting in the formation of a reactive mono-oxygen surface species. These results help to provide a fundamental understanding of the experimentally observed reactivity increases in the oxidative dehydrogenation of cyclohexane over Au/Co₃O₄ as compared to that on pure Co₃O₄ surfaces.

References

1. K. Weissermel and H.-J. Arpe, in *Industrial Organic Chemistry*. 1997, VCH: Weinheim. p. 240.
2. N.F. Dummer, S. Bawaked, J. Hayward, R. Jenkins, and G.J. Hutchings, *Oxidative dehydrogenation of cyclohexane and cyclohexene over supported gold, palladium and gold-palladium catalysts*. *Catalysis Today*, 2010. **154**(1–2): p. 2-6.
3. G. Busca, E. Finocchio, V. Lorenzelli, G. Ramis, and M. Baldi, *IR studies on the activation of C-H hydrocarbon bonds on oxidation catalysts*. *Catalysis Today*, 1999. **49**(4): p. 453-465.
4. J. Jansson, *Low-Temperature CO Oxidation over $\text{Co}_3\text{O}_4/\text{Al}_2\text{O}_3$* . *Journal of Catalysis*, 2000. **194**(1): p. 55-60.
5. M.F. Irfan, J.H. Goo, and S.D. Kim, *Co_3O_4 based catalysts for NO oxidation and NOx reduction in fast SCR process*. *Applied Catalysis B: Environmental*, 2008. **78**(3-4): p. 267-274.
6. Y. Morooka and A. Ozaki, *Regularities in catalytic properties of metal oxides in propylene oxidation*. *Journal of Catalysis*, 1966. **5**(1): p. 116-124.
7. J. G. McCarthy, Y. -F. Chang, V. L. Wong, and M.E. Johansson, *Kinetics of high temperature methane combustion by metal oxide catalysts*. Preprints, American Chemical Society, Division of Fuel Chemistry, 1997. **42**(1): p. 158-162.
8. V.A. Sazonov, V.V. Popovskii, and G.K. Borekov, *A Mass-Spectrometric Method for Determining the Volatility of Oxygen over Oxide Catalysts*. *Kinetika i Kataliz*, 1968. **9**: p. 312.
9. R.D. Waters, J.J. Weimer, and J.E. Smith, *An investigation of the activity of coprecipitated gold catalysts for methane oxidation*. *Catalysis Letters*, 1994. **30**(1): p. 181-188.
10. C.Y. Ma, Z. Mu, J.J. Li, Y.G. Jin, J. Cheng, G.Q. Lu, Z.P. Hao, and S.Z. Qiao, *Mesoporous Co_3O_4 and Au/ Co_3O_4 Catalysts for Low-Temperature Oxidation of Trace Ethylene*. *Journal of the American Chemical Society*, 2010. **132**(8): p. 2608-2613.
11. E.C. Tyo, C. Yin, M. Di Vece, Q. Qian, G. Kwan, S. Lee, B. Lee, J.E. DeBartolo, S. Seifert, R.E. Winans, R. Si, B. Ricks, S. Goergen, M. Rutter, B. Zugic, M. Fly, Z. Wang, R.E. Palmer, M. Neurock, and S. Vajda, *Oxidative Dehydrogenation of Cyclohexane on Cobalt Oxide (Co_3O_4) Nanoparticles: The Effect of Particle Size on Activity and Selectivity*. *ACS Catalysis*, 2012. **2**(11): p. 2409-2423.
12. A. Wolf and F. Schüth, *A systematic study of the synthesis conditions for the preparation of highly active gold catalysts*. *Applied catalysis A: General*, 2002. **226**(1–2): p. 1-13.
13. D. Widmann, Y. Liu, F. Schüth, and R.J. Behm, *Support effects in the Au-catalyzed CO oxidation – Correlation between activity, oxygen storage capacity, and support reducibility*. *Journal of Catalysis*, 2010. **276**(2): p. 292-305.
14. W.J. Xue, Y.F. Wang, P. Li, Z.-T. Liu, Z.P. Hao, and C.Y. Ma, *Morphology effects of Co_3O_4 on the catalytic activity of Au/ Co_3O_4 catalysts for complete oxidation of trace ethylene*. *Catalysis Communications*, 2011. **12**(13): p. 1265-1268.
15. E.C. Tyo, C. Yin, M. Di Vece, Q. Qian, R. Si, M. Flytzani-Stephanopoulos, S. Lee, B. Lee, S. Seifert, R.E. Winans, Z.W. Wang, R.E. Palmer, M. Neurock, and S. Vajda, *Gold doped cobalt oxide nanocatalysts: An in-situ- investigation using synchrotron radiation*. in *245th ACS National Meeting & Exposition*. 2013. New Orleans, LA: American Chemical Society.
16. G. Kresse and J. Hafner, *Ab initio molecular dynamics for liquid metals*. *Phys. Rev. B*, 1993. **47**: p. 558.
17. G. Kresse and J. Hafner, *Ab initio molecular-dynamics simulation of the liquid-metal-amorphous-semiconductor transition in germanium*. *Phys. Rev. B*, 1994. **49**: p. 14251.
18. G. Kresse and J. Furthmüller, *Efficient iterative schemes for ab initio total-energy calculations using a plane-wave basis set*. *Phys. Rev. B*, 1996. **54**: p. 11169.
19. A. Rohrbach, J. Hafner, and G. Kresse, *Electronic correlation effects in transition-metal sulfides*. *Journal of Physics: Condensed Matter*, 2003. **15**(6).
20. O. Bengone, M. Alouani, B. Iouml, P. chl, and J. Hugel, *Implementation of the projector augmented-wave LDA+U method: Application to the electronic structure of NiO*. *Physical Review B*, 2000. **62**(24): p. 16392.
21. J.P. Perdew, K. Burke, and M. Ernzerhof, *Generalized Gradient Approximation Made Simple*. *Phys. Rev. Lett.*, 1996. **77**: p. 3865.

22. J.P. Perdew, K. Burke, and M. Ernzerhof, *Erratum: Generalized Gradient Approximation Made Simple*. Phys. Rev. Lett., 1997. **78**: p. 1396.
23. P.E. Blöchl, *Projector augmented-wave method*. Phys. Rev. B, 1994. **50**: p. 17953.
24. G. Kresse and D. Joubert, *From ultrasoft pseudopotentials to the projector augmented-wave method*. Phys. Rev. B, 1999. **59**: p. 1758.
25. H.J. Monkhorst and J.D. Pack, *Special points for Brillouin-zone integrations*. Physical Review B, 1976. **13**(12): p. 5188-5192.
26. S.L. Dudarev, G.A. Botton, S.Y. Savrasov, C.J. Humphreys, and A.P. Sutton, *Electron-energy-loss spectra and the structural stability of nickel oxide: An LSDA+U study*. Physical Review B, 1998. **57**(3): p. 1505.
27. A. Gulino and I. Fragalà, *Cobalt hexafluoroacetylacetonate polyether adducts for thin films of cobalt oxides*. Inorganica Chimica Acta, 2005. **358**(15): p. 4466-4472.
28. D. Barreca, C. Massignan, S. Daolio, M. Fabrizio, C. Piccirillo, L. Armelao, and E. Tondello, *Composition and Microstructure of Cobalt Oxide Thin Films Obtained from a Novel Cobalt(II) Precursor by Chemical Vapor Deposition*. Chemistry of Materials, 2001. **13**(2): p. 588-593.
29. C.-S. Cheng, M. Serizawa, H. Sakata, and T. Hirayama, *Electrical conductivity of Co₃O₄ films prepared by chemical vapour deposition*. Materials Chemistry and Physics, 1998. **53**(3): p. 225-230.
30. P.S. Patil, L.D. Kadam, and C.D. Lokhande, *Preparation and characterization of spray pyrolysed cobalt oxide thin films*. Thin Solid Films, 1996. **272**(1): p. 29-32.
31. W.L. Roth, *The magnetic structure of Co₃O₄*. Journal of Physics and Chemistry of Solids, 1964. **25**(1): p. 1-10.
32. H. Jónsson, G. Mills, and K.W. Jacobsen, *Nudged Elastic Band Method for Finding Minimum Energy Paths of Transitions*, in *Classical and Quantum Dynamics in Condensed Phase Simulations*, B.J. Berne, G. Ciccotti, and D.F. Coker, Editors. 1998, World Scientific. p. 385-404.
33. H. Graeme and J. Hannes, *A dimer method for finding saddle points on high dimensional potential surfaces using only first derivatives*. The Journal of Chemical Physics, 1999. **111**(15): p. 7010-7022.
34. W.L. Smith and A.D. Hobson, *The structure of cobalt oxide, Co₃O₄*. Acta Crystallographica Section B, 1973. **29**(2): p. 362-363.
35. V.E. Henrich and P.A. Cox, *The surface science of metal oxide*. 1996: Cambridge University Press.
36. A. Montoya and B.S. Haynes, *Periodic density functional study of Co₃O₄ surfaces*. Chemical Physics Letters, 2011. **502**(1-3): p. 63-68.
37. Q. Qian, *Mechanistic Insights into the Catalytic Oxidative Dehydrogenation of Propane over Cobalt Oxide Derived from First Principles Density Functional Theory Calculations*, Master's Thesis in Department of Chemical Engineering. 2012, University of Virginia: Charlottesville, VA.
38. X. Tang, J. Li, and J. Hao, *Synthesis and characterization of spinel Co₃O₄ octahedra enclosed by the {1 1 1} facets*. Materials Research Bulletin, 2008. **43**(11): p. 2912-2918.
39. X. Xie, Y. Li, Z.-Q. Liu, M. Haruta, and W. Shen, *Low-temperature oxidation of CO catalysed by Co₃O₄ nanorods*. Nature, 2009. **458**(7239): p. 746-749.
40. I.X. Green, W. Tang, M. Neurock, and J.T. Yates, *Spectroscopic Observation of Dual Catalytic Sites During Oxidation of CO on a Au/TiO₂ Catalyst*. Science, 2011. **333**(6043): p. 736-739.
41. J. Wei and E. Iglesia, *Isotopic and kinetic assessment of the mechanism of methane reforming and decomposition reactions on supported iridium catalysts*. Physical Chemistry Chemical Physics, 2004. **6**(13): p. 3754-3759.
42. N.W. Cant, C.A. Lukey, P.F. Nelson, and R.J. Tyler, *The rate controlling step in the oxidative coupling of methane over a lithium-promoted magnesium oxide catalyst*. Journal of the Chemical Society, Chemical Communications, 1988(12): p. 766-768.
43. Y.-H. Chin, C. Buda, M. Neurock, and E. Iglesia, *Selectivity of chemisorbed oxygen in C-H bond activation and CO oxidation and kinetic consequences for CH₄-O₂ catalysis on Pt and Rh clusters*. Journal of Catalysis, 2011. **283**(1): p. 10-24.
44. Y.-H. Chin, C. Buda, M. Neurock, and E. Iglesia, *Reactivity of Chemisorbed Oxygen Atoms and Their Catalytic Consequences during CH₄-O₂ Catalysis on Supported Pt Clusters*. Journal of the American Chemical Society, 2011. **133**(40): p. 15958-15978.
45. G. Jones, J.G. Jakobsen, S.S. Shim, J. Kleis, M.P. Andersson, J. Rossmeisl, F. Abild-Pedersen, T. Bligaard, S. Helveg, B. Hinnemann, J.R. Rostrup-Nielsen, I. Chorkendorff, J. Sehested, and J.K. Nørskov, *First principles calculations and experimental insight into methane steam reforming over transition metal catalysts*. Journal of Catalysis, 2008. **259**(1): p. 147-160.

46. R. Burch, D.J. Crittle, and M.J. Hayes, *C-H bond activation in hydrocarbon oxidation on heterogeneous catalysts*. *Catalysis Today*, 1999. **47**(1-4): p. 229-234.
47. D.J. Driscoll and J.H. Lunsford, *Gas-phase radical formation during the reactions of methane, ethane, ethylene, and propylene over selected oxide catalysts*. *The Journal of Physical Chemistry*, 1985. **89**(21): p. 4415-4418.
48. G. Henkelman, A. Arnaldsson, and H. Jónsson, *A fast and robust algorithm for Bader decomposition of charge density*. *Computational Materials Science*, 2006. **36**(3): p. 354-360.
49. W. Tang, E. Sanville, and G. Henkelman, *A grid-based Bader analysis algorithm without lattice bias*. *Journal of Physics: Condensed Matter*, 2009. **21**(8): p. 084204.
50. J. Haber and M. Witko, *Oxidation catalysis—electronic theory revisited*. *Journal of Catalysis*, 2003. **216**(1-2): p. 416-424.
51. H. Liu, A. I. Kozlov, A. P. Kozlova, T. Shido, and Y. Iwasawa, *Active oxygen species and reaction mechanism for low-temperature CO oxidation on an Fe₂O₃-supported Au catalyst prepared from Au(PPh₃)(NO₃) and as-precipitated iron hydroxide*. *Physical Chemistry Chemical Physics*, 1999. **1**(11).
52. B. Schumacher, Y. Denkwitz, V. Plzak, M. Kinne, and R.J. Behm, *Kinetics, mechanism, and the influence of H₂ on the CO oxidation reaction on a Au/TiO₂ catalyst*. *Journal of Catalysis*, 2004. **224**(2): p. 449-462.
53. M. Ojeda, B.-Z. Zhan, and E. Iglesia, *Mechanistic interpretation of CO oxidation turnover rates on supported Au clusters*. *Journal of Catalysis*, 2012. **285**(1): p. 92-102.
54. M. Iwamoto, Y. Yoda, N. Yamazoe, and T. Seiyama, *Study of metal oxide catalysts by temperature programmed desorption. 4. Oxygen adsorption on various metal oxides*. *The Journal of Physical Chemistry*, 1978. **82**(24): p. 2564-2570.
55. B. Solsona, E. Aylón, R. Murillo, A.M. Mastral, A. Monzonís, S. Agouram, T.E. Davies, S.H. Taylor, and T. Garcia, *Deep oxidation of pollutants using gold deposited on a high surface area cobalt oxide prepared by a nanocasting route*. *Journal of Hazardous Materials*, 2011. **187**(1-3): p. 544-552.
56. S. Xie, H. Dai, J. Deng, Y. Liu, H. Yang, Y. Jiang, W. Tan, A. Ao, and G. Guo, *Au/3DOM Co₃O₄: highly active nanocatalysts for the oxidation of carbon monoxide and toluene*. *Nanoscale*, 2013. **5**(22): p. 11207-11219.
57. Q. Fu, H. Saltsburg, and M. Flytzani-Stephanopoulos, *Active Nonmetallic Au and Pt Species on Ceria-Based Water-Gas Shift Catalysts*. *Science*, 2003. **301**(5635): p. 935-938.
58. K. Morgan, K.J. Cole, A. Goguet, C. Hardacre, G.J. Hutchings, N. Maguire, S.O. Shekhtman, and S.H. Taylor, *TAP studies of CO oxidation over CuMnO_x and Au/CuMnO_x catalysts*. *Journal of Catalysis*, 2010. **276**(1): p. 38-48.

Chapter 5 Catalytic Cracking of Hydrocarbons on Solid Acid Catalysts

5.1 Introduction

Hydrocarbon cracking is an important endothermic reaction that can be used to increase the heat sink of jet fuel thus allowing it to act as a coolant for hypersonic propulsion systems. Solid acid catalysts have been shown to catalyze this reaction effectively through elementary steps involving carbonium and carbenium ion intermediates [1]. Catalytic cracking is also carried out commercially in petroleum refining, using zeolites which are highly active and selective in converting gas oils to gasoline. Zeolites, however, can rapidly deactivate as a result of the formation of carbonaceous deposits (coking) that block the openings of micropores and also poison the active sites inside [2-4]. Zeolites are often regenerated *in-situ* by oxidizing the coke intermediates off. It is, however, impractical to introduce such catalyst regeneration units in hypersonic vehicles, where any unnecessary increase in system complexity and total weight should be avoided. The active cooling of the fuel via catalytic cracking will require high catalytic activities over prolonged periods of time. In addition, the catalyst will need to be able to withstand the high operating temperatures in the jet engines. Non-porous and thermally stable metal oxide acid catalysts may prove to be more suitable catalysts than zeolites. Sulfated zirconia and tungstated zirconia show some promise as both materials demonstrate strong Brønsted acidity and are active in catalyzing a range of different solid acid reactions such as the isomerization of hydrocarbons [5, 6], which presumably require similar active sites as those for hydrocarbon cracking. While sulfated zirconia is more active than tungstated zirconia it is not thermally stable [7].

Previous experimental studies by different groups have shown that the catalytic performance of WO_x/ZrO_2 as a solid acid is very sensitive to the loading of tungstate on the zirconia surface [6, 8]. It is generally believed that there is an optimal loading of WO_x with surface densities of 5–8 W atoms nm^{-2} which result in the highest catalytic activities. Some researchers speculate that the Brønsted acid sites are the result of the *in-situ* partial reduction of W^{6+} in the tungstate cluster, which creates a charge imbalance in the nanocluster [8, 9]. Previous DFT calculations [10] showed that increasing the size of the tungstate nanocluster domain on ZrO_2 , from monomer to dimer to trimer, systematically increases the Brønsted acidity (measured by deprotonation energy). The increased acidity can be explained by an increase in the delocalization of the negative charge that forms on the conjugate base upon the deprotonation of the acid.

The detailed atomic structure of the active surface species is still unclear. Recent high-angle annular dark-field imaging (HAADF) and catalytic activity measurements [11] indicate that the most active species are ~ 1 nm three-dimensional WO_x clusters incorporated with Zr cations [12]. Earlier studies [13, 14] have proposed three-dimensional Zr^{4+} exposed tungstate polyoxometalates (POMs) networks with similar structures to that of heteropolyacids (HPAs) as the active species. POMs have been examined in some detail both experimentally [15] and theoretically [16] as their well-defined structures make them as ideal model solid acid catalysts. Zr-containing POMs, as such, are promising analogs of tungstated zirconia catalysts [17].

While solid acids catalyze cracking, they also catalyze oligomerization as well as dehydrogenation pathways that ultimately lead to the formation of coke precursors which can deactivate the catalyst. The high-temperatures and pressures at which these reactions are run can also result in unstable polycyclic aromatic hydrocarbons (PAH) as well as aryl radical intermediates that readily promote coke formation [18-25]. Previous studies on zeolites revealed that coke formation involves a complex network of elementary steps that depend on temperature as well as catalyst composition and pore structure [26, 27]. At low temperatures, coke predominantly involves oligomerization reactions, while at high temperatures, cyclization, alkylation, and hydrogen transfer become important and can result in different coke precursors [28]. Coke formation rates have also been directly correlated with the strength and density of acid sites [29]. Little, however, is known about the mechanisms responsible for coke formation or how to limit the coke formation on WO_x/ZrO_2 .

Herein we examine the mechanistic details and the role of solid acidity on the cracking of butane which is used as a very simple surrogate for the higher molecular weight alkanes found in jet fuel.

5.2 Method

5.2.1 Computational Details

All the results reported herein were carried out using periodic plane wave density functional theory (DFT) calculations as implemented in Vienna ab initio Simulation Package (VASP) [30-33]. The generalized gradient approximation (GGA), in the form of Perdew-Burke-Ernzerhof (PBE) [34, 35] was used to model the exchange and correlation effects. The interactions between the valence electrons and the core were described with the projector augmented wave method (PAW) [36, 37], and the kinetic-energy cutoff for plane wave basis set was set at 400 eV. The nudged elastic band (NEB) [38] method was used to find the initial identity of the transition state. The results were used together with the dimer [39] methods in order to isolate the transition state. All of the structural optimizations and transition state searches were converged to the point where all of the forces on the atoms were found to be less than 0.05 eV/Å.

Tungsten polyoxometalate clusters with well-defined structures, especially Keggin type polyoxotungstates ($H_{8-n}X_nW_{12}O_{40}$, X=Zr, Al, Si, P) [40] were used in the calculations. A cubic unit cell with a lattice parameter $a = 20 \text{ \AA}$ was chosen, which is large enough to neglect the interactions between the metal cluster and its periodic images. A $1 \times 1 \times 1$ Monkhorst-Pack [41] mesh was used to sample the first Brillouin zone. A $12.8 \times 14.6 \times 22.5 \text{ \AA}^3$ surface cell of t-ZrO₂(101) with six atomic layers was used to model the WO_x clusters supported on the ideal ZrO₂ surface. The Brillouin zone was sampled using a $3 \times 3 \times 1$ \mathbf{k} -point mesh with Monkhorst-Pack scheme. The three bottom atomic layers of the slab were fixed during geometry optimization.

5.2.2 Measurement of Acid Strength

A wide range of experimental methods, including infrared spectroscopy, temperature-programmed desorption of adsorbed base molecules [42], microcalorimetry [43], and solid-state ^1H NMR spectroscopy [44] have been used to probe the properties of solid acid catalysts but to date there are no known methods to quantitatively [45] determine the intrinsic solid acidity. The intrinsic Brønsted acidity, however, can be directly calculated as the energy required to remove a proton (H^+) from the acid (BH) to form an anionic conjugate base (B^-), $\text{BH} \rightarrow \text{B}^- + \text{H}^+$, which is known as the deprotonation energy (DPE) [46-49]. The smaller the DPE of a solid acid the easier it is to deprotonate and thus the stronger its Brønsted acidity.

Calculating the deprotonation energy requires calculating charged systems, namely that of the separated conjugate base and that of the proton. For periodic systems, the addition of net charge requires an equal but opposite charge be applied to the background in order to maintain an overall charge neutrality across the unit cell. The background charge can vary with the size of unit cell [50] and this can lead to small differences for systems comprised of different cell sizes as we will find later in Figure 5.7. These challenges are not present in modeling Lewis acid sites. The Lewis acidity can be probed by examining the lowest unoccupied molecular orbital (LUMO) energy which involves vacant orbitals on the Lewis acid center that can accept electrons from the reactant [51-53]. A lower energy for the LUMO indicates stronger Lewis acidity.

In addition to the values of the deprotonation energy, we examine the adsorption energies for various basic probe molecules, such as ammonia, to the Brønsted acid site to provide a simple qualitative measure of acidity. A Born-Haber cycle can be used to analyze the elementary steps for the adsorption of a base onto the Brønsted solid acid. This involves the energy to deprotonate the acid (DPE), the proton affinity of the gas phase base (PA), and the interaction of the protonated base onto the conjugate base of the solid acid (Figure 5.10 in supplementary materials). This indicates that the proton is bound to two competing bases - the probe molecule and the conjugate base of the original Brønsted acid. The DFT results for the adsorption of a series of different molecules with increasing basicities (PA) onto a series heteropolyacid structures with increasing Brønsted acidities indicate that the more basic the molecule the more sensitive it is to the changes in the acidity of the solid acid (DPE) as shown in Figure 5.1. For weak base molecules (Figure 5.11 in supplementary materials), such as methanol (CH_3OH), acetonitrile (CH_3CN) and acetone ($(\text{CH}_3)_2\text{CO}$), the proton remains bound to the oxygen of the solid acid, as the O-H bond is only weakly elongated and is not ruptured. The adsorption energies for these weak bases are not very sensitive to DPE as the solid acid is not actually deprotonated via the adsorption of these weak basic probe molecules. For stronger basic molecules (Figure 5.12 in supplementary materials), such as ammonia (NH_3), pyridine ($\text{C}_5\text{H}_5\text{N}$) and dimethylamine ($(\text{CH}_3)_2\text{NH}$), the proton can be abstracted from the Brønsted acid site to form a protonated base. Ammonia, although less basic, is significantly smaller in size than pyridine or dimethylamine and exhibits little steric hindrance to adsorption.

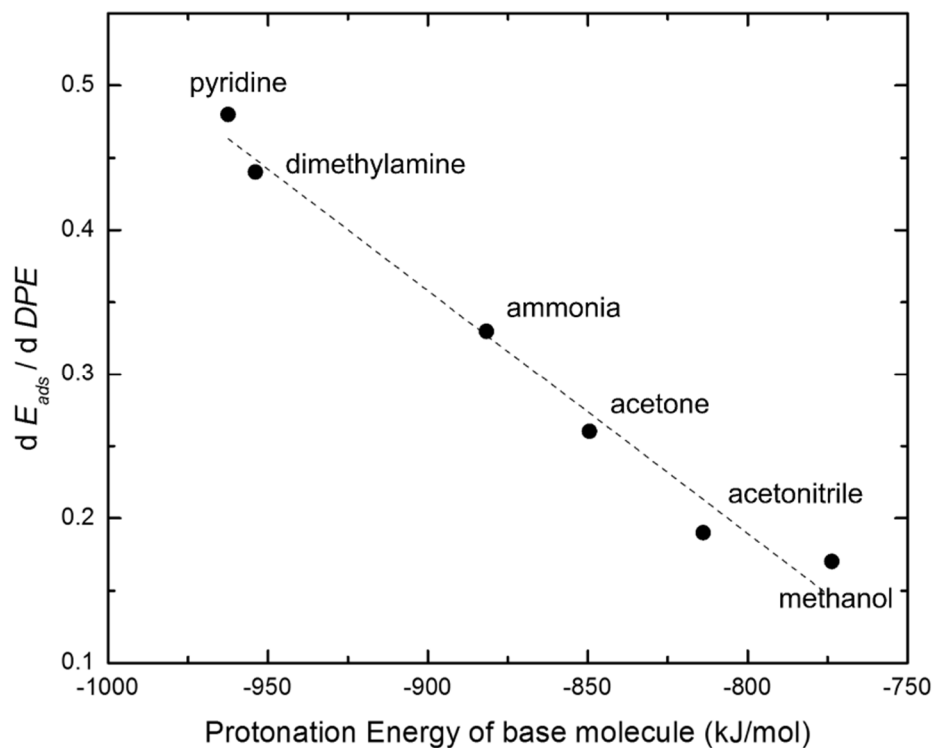


Figure 5.1 The sensitivity of adsorption energy (E_{ads}) for different basic probe molecules onto the Brønsted acid sites of a series of different HPAs with different solid acidities to the change in deprotonation energy (DPE) of acid sites is correlated with the basicity (measured as protonation energy) of probe molecules.

5.3 Results and Discussion

5.3.1 Monomolecular and bimolecular cracking

The catalytic cracking of alkanes and other hydrocarbons is thought to proceed by monomolecular reaction at high temperature and low reactant partial pressures [1, 54] involving either a direct insertion of the proton from the Brønsted acid site into a specific C-C bond or via a concerted proton addition from the Brønsted acid to a specific carbon site (C1) and hydride transfer from that site to a neighboring carbon site (C2). At low temperature and higher partial pressures [1, 54], catalytic cracking is thought to occur via a bimolecular path involving a hydride transfer from the gas phase reactant molecule to a bound alkoxide which is rapidly followed by the subsequent β -scission of secondary carbenium ion to form the gas phase product and a bound alkoxide. First-principles density functional theory calculations were carried out to examine both the mono- and bi-molecular paths and their corresponding energies and mechanisms for the catalytic cracking of butane over several solid acid catalysts.

The monomolecular mechanism (protolytic cracking) [1] proceeds via proton transfer from the surface WO-H Brønsted acid site into the center of the secondary C2-C3 bond of butane C_4H_{10} to form a $C_2H_{11}^+$ carbonium ion transition state that collapses thus resulting in the formation of ethane C_2H_6 and a $C_2H_5^+$ carbenium ion which readily rebounds to the WO site as an ethoxide or deprotonates to reform the acid site WO-H and a gas phase ethylene (C_2H_4) molecule (see Figure 5.2). The direct deprotonation of the $C_2H_5^+$ to form ethylene and regenerate WO-H site was calculated to be 27 kJ mol^{-1} more favorable. The monomolecular cracking of butane to form ethane and ethylene molecules and regenerate the

Brønsted acid site was calculated to have an overall apparent activation barrier of 185 kJ mol⁻¹.

The bimolecular mechanism [55], which is regarded as the classical cracking mechanism, involves hydride transfer from a gas phase butane C₄H₁₀ to surface ethoxide WO-C₂H₅ and results in the formation of a C₄H₉⁺ carbenium ion and gas phase ethane C₂H₆ product. The C₄H₉⁺ carbenium ion then undergoes β-scission to form ethene C₂H₄ and a C₂H₅⁺ carbenium ion that rebounds to the surface WO⁻ site (Figure 5.3). The bimolecular path has an overall apparent activation barrier of 211 kJ mol⁻¹ which is 26 kJ mol⁻¹ higher than that calculated for the monomolecular path.

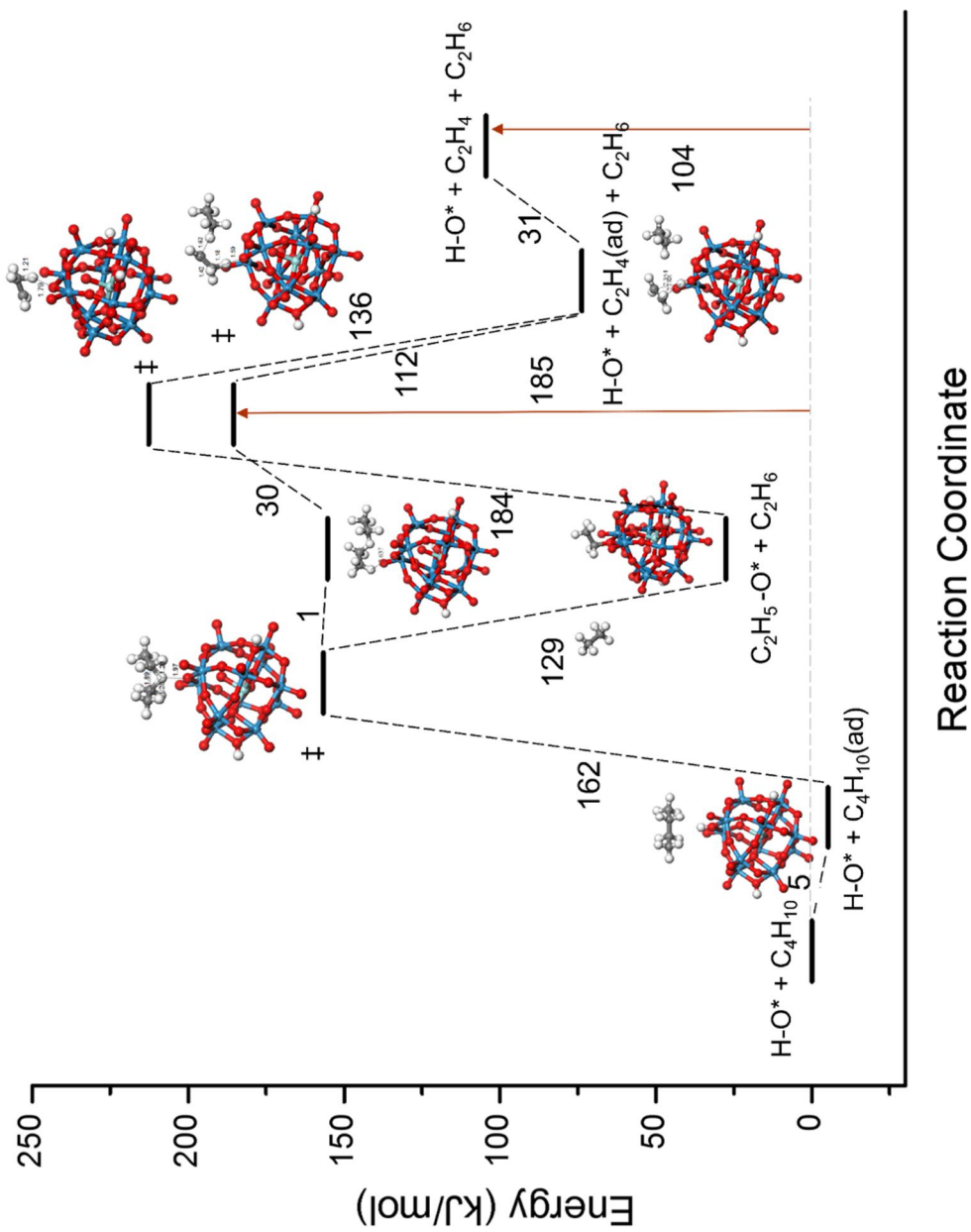


Figure 5.2 DFT-calculated catalytic monomolecular cracking of butane at a Brønsted acid site on one of the Keggin type of Zr-polyoxotungstates ($\text{H}_4\text{ZrW}_{12}\text{O}_{40}$), which starts with proton attaching the internal C-C bond of butane resulting in the formation of a carbonium ion which collapse into ethane and ethyl carbenium ion that deprotonates and forms ethylene.

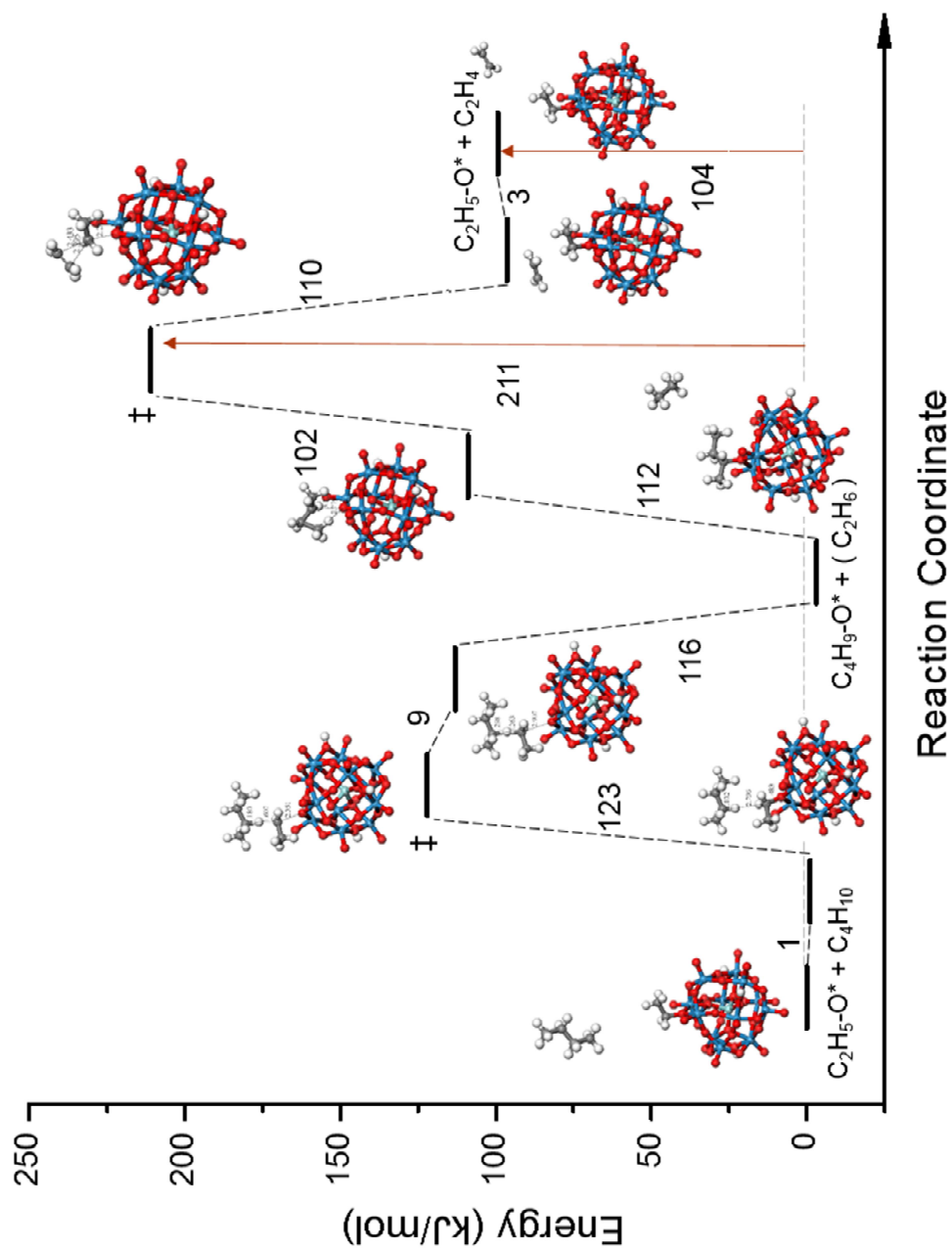


Figure 5.3 DFT-calculated catalytic bimolecular cracking of butane at a Brønsted acid site on one of the Keggin type of Zr-polyoxotungstates ($H_4ZrW_{12}O_{40}$), which starts with a butane transferring hydride to ethoxide resulting in the formation of ethane and butyl carbenium ion which undergoes β -scission and forms ethylene and ethoxide.

5.3.2 More discussion on monomolecular cracking

Monomolecular cracking has been studied in some detail in the literature over model zeolite catalysts [56-58] and there are at least two different proposed mechanisms [59] depending upon how the C-C bond is activated and cleaved. The two paths are illustrated in Figures 5.4 and 5.5 for the cracking of the central C2-C3 bond of n-butane over the Keggin-type heteropolyacid (HPA). The first path (Figure 5.4a) involves a direct proton attack and scission of the central C2-C3 bond whereas the second path (Figure 5.5a) involves a simultaneous proton attack at single carbon center (C2) together with an intramolecular H-transfer to the second carbon site (C3).

In addition to the differences in the different mechanisms, cracking can also occur at different sites on the molecule. While we have discussed the activation of internal C-C bonds with secondary carbon centers, cracking can also readily occur at internal secondary-tertiary and tertiary-tertiary C-C bonds as well as at terminal primary-secondary and primary-tertiary C-C bonds. To extend our results on the activation of the internal secondary-secondary C-C bond of butane, we examined the cracking at the terminal-secondary C-C bond of butane as well as the secondary-tertiary C-C bond of isopentane. The results are shown in Figures 5.4 and 5.5.

All of the reaction paths outlined in Figures 5.4 and 5.5 were carried out over four different HPA structures with different central atoms ($X = \text{P, Si, Zr, Al}$) to examine the influence of Brønsted acidity on the cracking mechanisms and pathways. In plotting the activation barriers for each of these C-C bond cracking reactions versus their deprotonation energies

(DPE), we found a direct linear relationship between acidity and activity as the stronger acids (lower DPE values) had the lower activation barriers. The direct H^+ insertion at C-C bond (Figure 5.6a) was calculated to be slightly easier than concerted H^+ attack-hydride transfer (Figure 5.6c). The C-C bond activation was calculated to be easier at more substituted tertiary-secondary carbons (Figure 5.6b) than secondary-secondary carbons (Figure 5.6a). Similarly, the C-C bond activation is found to be easier at a secondary carbon (Figure 5.6c) than a primary carbon (Figure 5.6d). Our results indicate that unimolecular cracking of hydrocarbons occur via a proton attacking at a C-C bond, and that a more substituted carbon leads to a lower activation barrier.

It is worth to note that our calculations are based on non-porous tungstate POM models, however central C-C bonds do not always crack faster than terminal C-C bonds over microporous zeolites where solvation effects (strong attractive van der Waals interactions between the hydrocarbon and the confining void structure) and entropy can play an important role [60, 61] and in some cases (e.g. n-alkane cracking in the partial confinement of 8-MR pockets in MOR [62]) result in dominant cracking at the terminal C-C bonds.

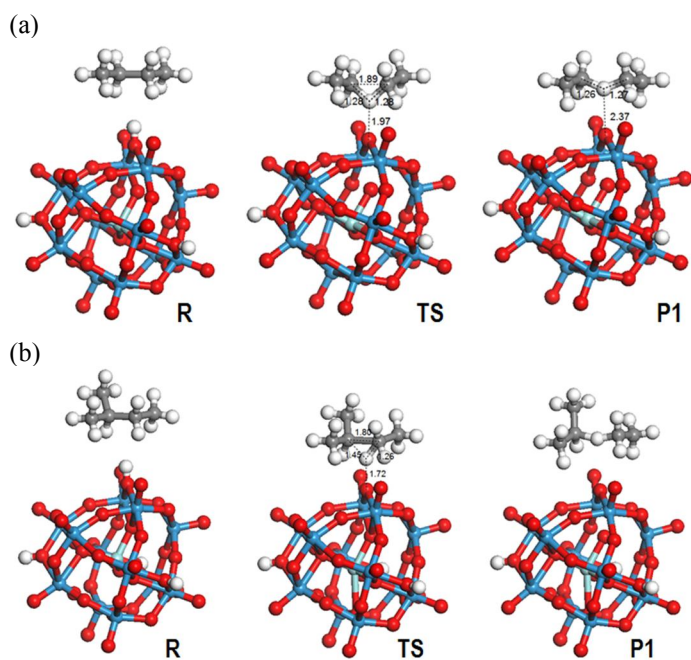


Figure 5.4 Monomolecular cracking of butane and isopentane with direct H^+ insertion at the secondary-secondary carbon bond (a) and the secondary-tertiary carbon bond (b) over different HPAs with Keggin structures, $\text{XM}_{12}\text{O}_{40}^{n-}$, $\text{X}=\text{Al}, \text{Si}, \text{P}, \text{Zr}$; $\text{M}=\text{W}$.

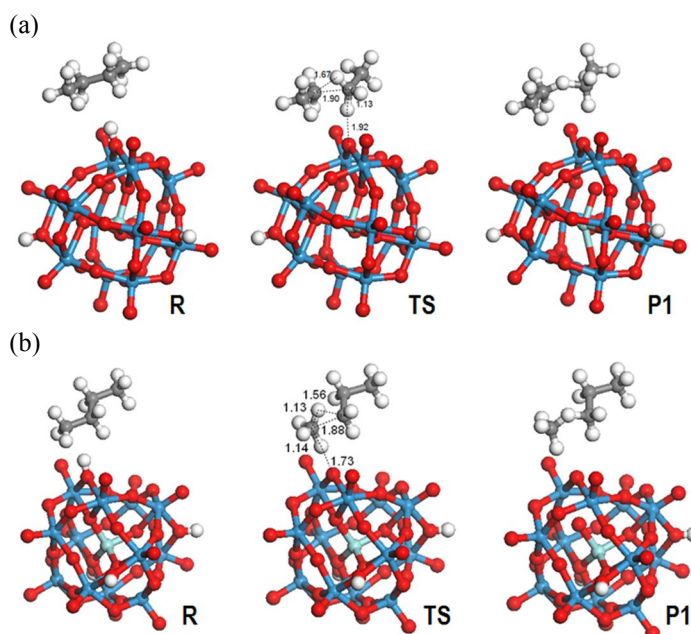


Figure 5.5 Monomolecular cracking of butane with concerted H^+ attack-hydride transfer at the secondary carbon (a) and primary carbon (b) over different HPAs with Keggin structures, $\text{XM}_{12}\text{O}_{40}^{n-}$, $\text{X}=\text{Al}, \text{Si}, \text{P}, \text{Zr}$; $\text{M}=\text{W}$.

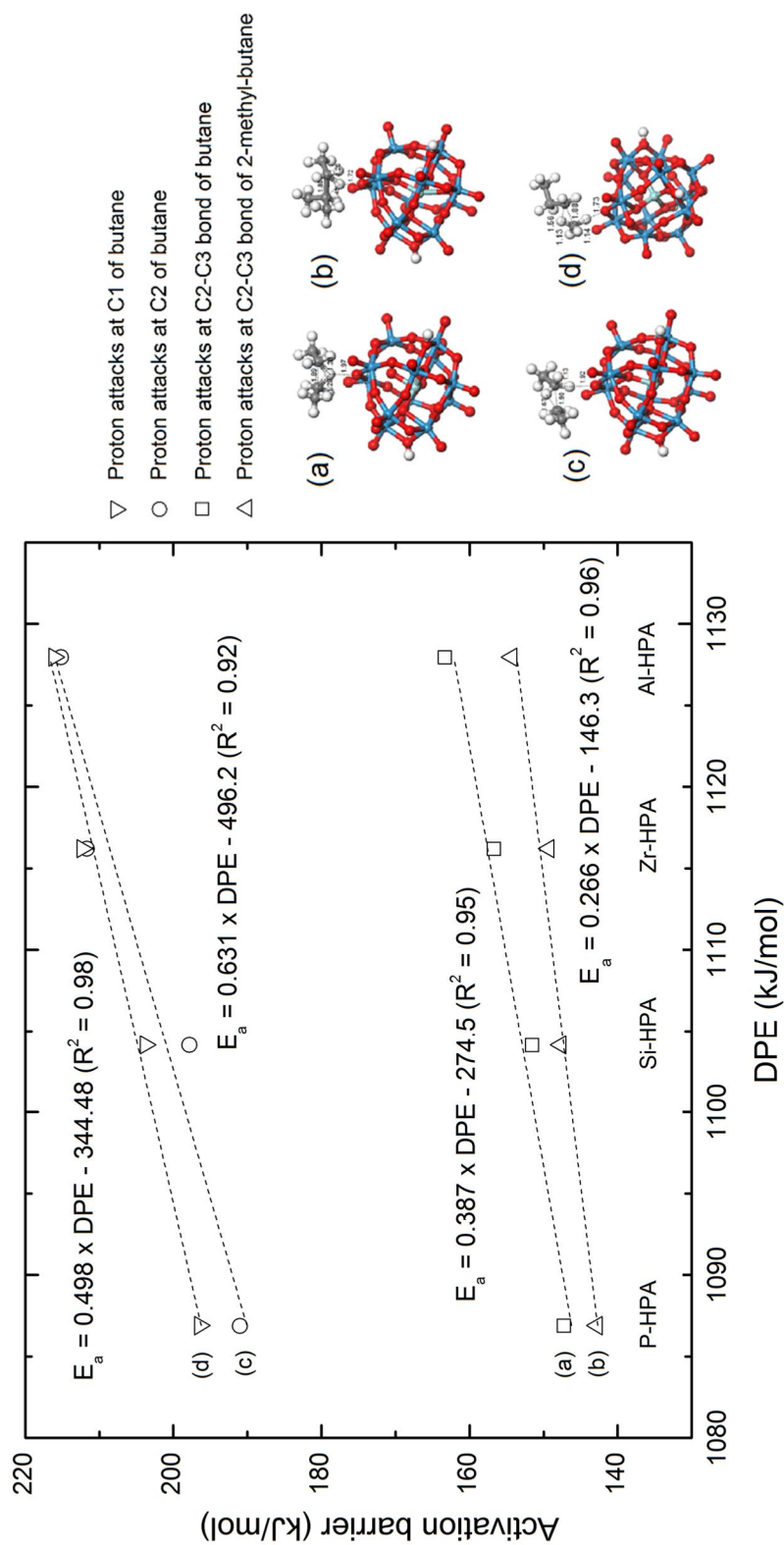


Figure 5.6 Correlations of the activation barrier of monomolecular C-C bond cracking with the acidity effect represented by deprotonation energies (DPE) of a series of different heteropolyacids (HPAs), including (a) proton attack at C2-C3 of butane, (b) proton attack at C2-C3 of isopentane, (c) concerted proton attack at C2 of butane and hydride transfer, and (d) concerted proton attack at C1 of butane and hydride transfer. The slope of a fitting line represents the sensitivity of the activation barrier to the change in Brønsted acidity.

5.3.3 Structure-reactivity relationships

In an effort to begin to understand the influence of catalyst structure on cracking, we extended our analyses of unimolecular activation of the internal C-C bond of butane on the model HPA structures to small tungstate clusters (monomer, dimer, and trimer) supported on model t-ZrO₂(101) surfaces. These two-dimensional tungstate clusters, however, were found to be less active than the Keggin-type heteropolyacids (HPAs). The results shown in Figure 5.7 indicate that the three-dimensional HPA structures report barriers between 147-163 kJ mol⁻¹, whereas the two-dimensional tungstate clusters supported on zirconia had significantly higher barriers ranging from 188-225 kJ mol⁻¹. The much lower barriers on the HPAs can be attributed to their much higher Brønsted acidity (lower deprotonation energies) of the HPA as compared to the two-dimensional tungstate clusters on zirconia. This can be seen quite clearly in the Figure 5.7 which show direct linear relationships between the activation barriers and the deprotonation energies for the HPAs and tungstated zirconia structures. The abrupt jump in moving from the Keggin structures to the tungstated clusters is due to the challenge of calculating the charge unit cell systems as was discussed earlier.

The higher activity of Zr-polyoxotungstate (Zr-POW) structures over zirconia supported tungstate clusters reported in Figure 5.7 is consistent with experimental results by Wachs et al. that indicate the three-dimensional Zr-containing polyoxotungstate clusters are the active species for acid catalyzed isomerization [11-14]. In addition to the Keggin structures, we also examined various other three-dimensional polyoxometalate (Figure 5.8) clusters including the Lindqvist (H₂W₅O₁₈Zr-H₂O and H₆(W₅O₁₈Zr-OH)₂) type [17] and the

Dawson ($\text{H}_8\text{W}_{18}\text{O}_{62}\text{Zr}_2$) type [63] structures and found the acid strength either measured by DPE or NH_3 adsorption energy increases with the size of the cluster. The increased acidity can be explained by an increase in the delocalization [10] of the negative charge on the deprotonated conjugate base as shown in Table 5.1. The increase in the activity with increasing cluster size is somewhat offset however by the decreasing thermal stability of the larger Zr-POW structures which is shown by the increasing exothermicity of the Zr-POW decomposition energies as reported in Table 5.1.

Table 5.1 DFT-calculated decomposition energy of Zr-containing polyoxotungstates and Bader charges on their deprotonated conjugate bases of corresponding Brønsted acid sites (as in Figure 5.8).

Zr-containing Polyoxotungstates	ΔE_{decomp} (kJ mol ⁻¹) *	Bader charge on deprotonated conjugate base O ⁻ (e)
$\text{H}_8\text{W}_{18}\text{O}_{62}\text{Zr}_2$ (Dawson)	-669	-0.906
$\text{H}_4\text{W}_{12}\text{O}_{40}\text{Zr}$ (Keggin)	-364	-0.921
$\text{H}_6(\text{W}_5\text{O}_{18}\text{Zr-OH})_2$ (Lindqvist)	-296	-0.941
$\text{H}_2\text{W}_5\text{O}_{18}\text{Zr-H}_2\text{O}$ (Lindqvist)	-239	-0.981

* $\Delta E_{decomp} = aE_{\text{WO}_3} + bE_{\text{H}_2\text{O}} + cE_{\text{ZrO}_2} - E_{\text{H}_2\text{bW}_a\text{O}_{3a+b+2c}\text{Zr}_c}$, which is the DFT-calculated enthalpy change of the decomposition reaction $\text{H}_2\text{bW}_a\text{O}_{3a+b+2c}\text{Zr}_c \rightarrow a\text{WO}_3 + b\text{H}_2\text{O} + c\text{ZrO}_2$ as an indication of thermal stability.

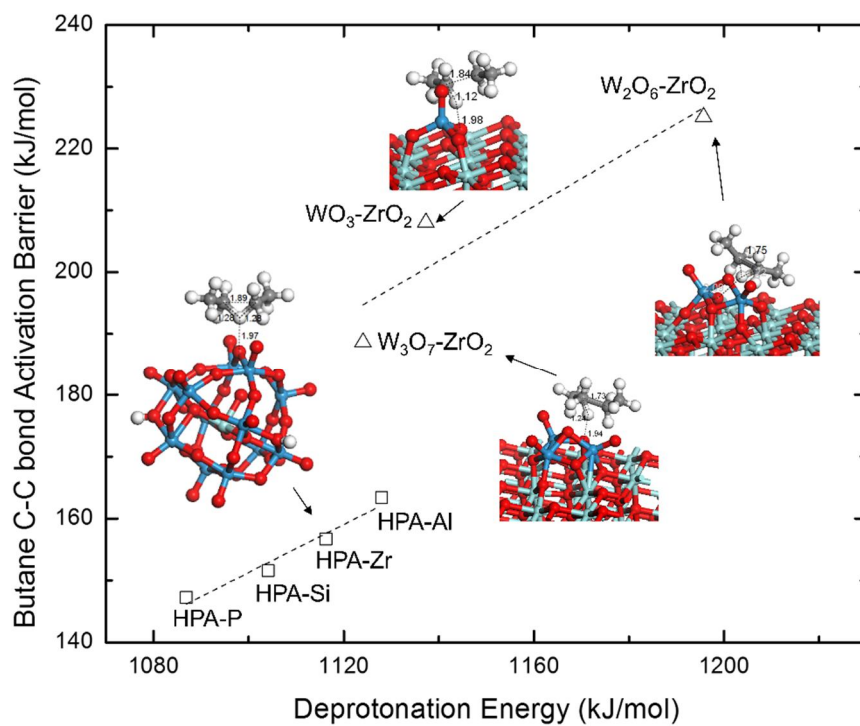


Figure 5.7 Correlations of the C-C bond activation barrier of n-butane (proton attacks C2-C3 bond) with the Brønsted acidity represented by deprotonation energy (DPE) over different solid acid model systems (including tungstated zirconia and Keggin-type HPAs).

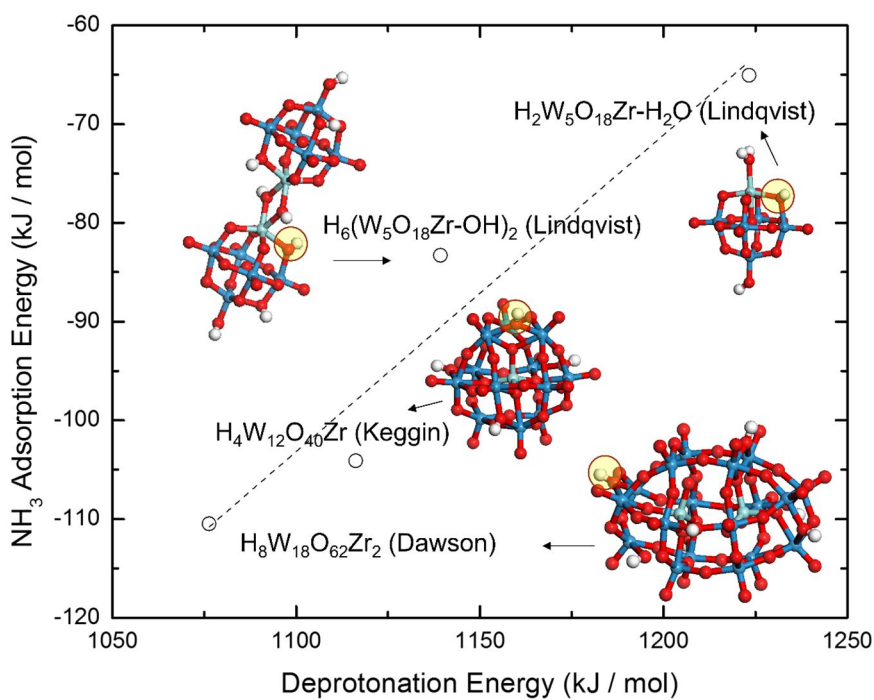


Figure 5.8 Brønsted acidity measured by NH₃ Adsorption energy and DPE of four types of Zr-containing polyoxotungstates (on circled Brønsted acid sites).

5.3.4 Reactions related to coke formation

It is widely accepted that the formation of the “first aromatic ring” is the first step towards soot formation from non-aromatic hydrocarbons [64]. The presence of Brønsted acid sites will not only catalyze cracking of alkanes but can also catalyze alkane dehydrogenation to form olefins and dienes, oligomerization and cyclization pathways that can ultimately lead to formation of aromatics (see plausible reaction pathway of oligomerization of C_2H_x 's to form cyclohexane in supplementary Figure 5.13). Among these reactions, dehydrogenation is one of the most critical steps leading to the formation of coke or coke precursors. We carried out DFT calculations herein to examine the dehydrogenation of butane at the Brønsted acid sites of HPAs. The reaction proceeds by the proton-coupled electron transfer where the proton on the HPA (H^+) adds to the hydride (H^-) of the alkane to form H_2 and corresponding $C_4H_9^+$ carbenium ion, which readily rebounds to the WO^- and forms butoxide. The rates of dehydrogenation are known to increase with acidity. This can be clearly seen by the linear relationship between the calculated activation barriers for the dehydrogenation of butane to butoxide for different heteropolyacids as shown in Figure 5.9. The results suggest that the increase in acidity which would increase the rates of cracking would also concomitantly increase the rates of dehydrogenation and as such lead to precursors to form aromatics and coke precursors.

Our calculations (Figure 5.9) suggest that dehydrogenation has a much higher sensitivity to acid site strength (0.522), as measured by the change in the activation barrier to the change in deprotonation energy, than cracking (0.387) or oligomerization (0.392). As such there should be an optimal acid strength that promotes cracking reactions while minimizing

coke precursor formation. The number of Brønsted acid sites can also play an important role in coke formation. There may be an optimal density of sites that reduces the adsorption and condensation of coke molecules/precursors while maintaining a reasonable level of cracking activity. The detailed exploration of the effects of catalyst structure, acidity and operating conditions on the individual elementary steps is an interesting and important topic for future studies.

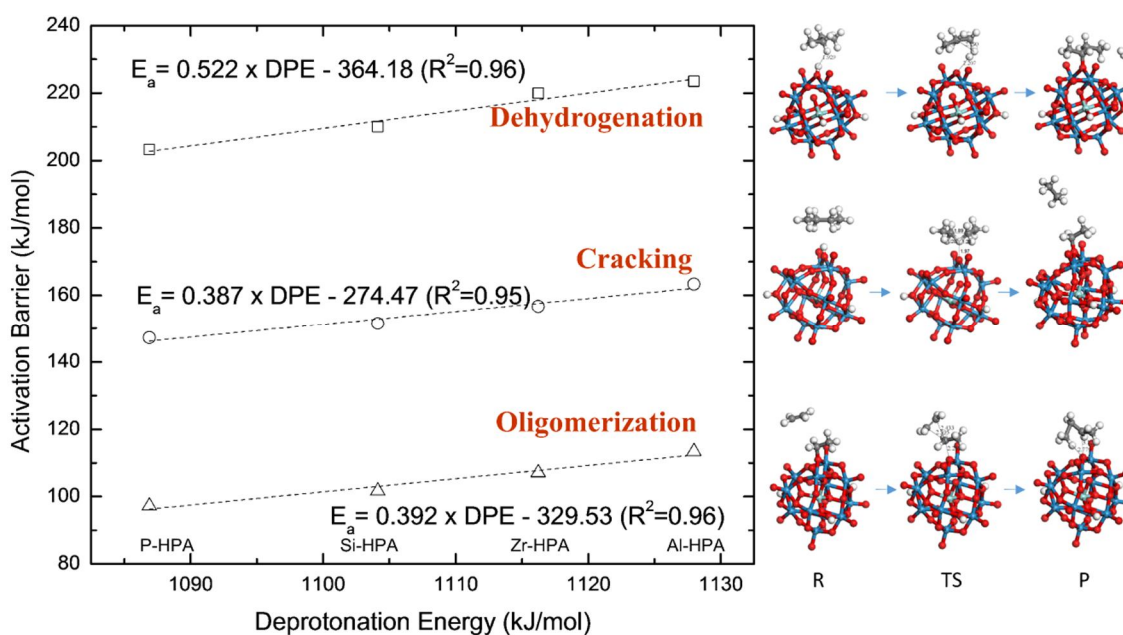


Figure 5.9 Correlation of the activation barriers of butane dehydrogenation (hollow squares), butane monomolecular cracking (hollow circles) and C_2H_x oligomerization (hollow triangles) with deprotonation energy (DPE) at Brønsted acid sites of different heteropolyacids (HPAs). The slope of a fitting line represents the sensitivity of the activation barrier to the change in Brønsted acidity.

5.4 Summary

First-principles density functional theory calculations were carried out to examine the elementary steps and their corresponding energies for different mechanisms suggested in the catalytic cracking and dehydrogenation of butane over several solid acid catalysts. The Brønsted acidity of different sites was measured by calculating the deprotonation energy of the solid acid. Zr-containing polyoxotungstates with a variety of three-dimensional structures were found to be more acidic (lower values of DPE) than two-dimensional surface tungstate clusters supported on ZrO_2 . The rates of these reactions were all directly correlated to the acidity of the catalyst. However the sensitivity of activation barrier to the change in DPE are different in different reactions, which may help to guide the rational design of a solid acid catalyst that can promote cracking and minimize coking.

Supplementary Materials

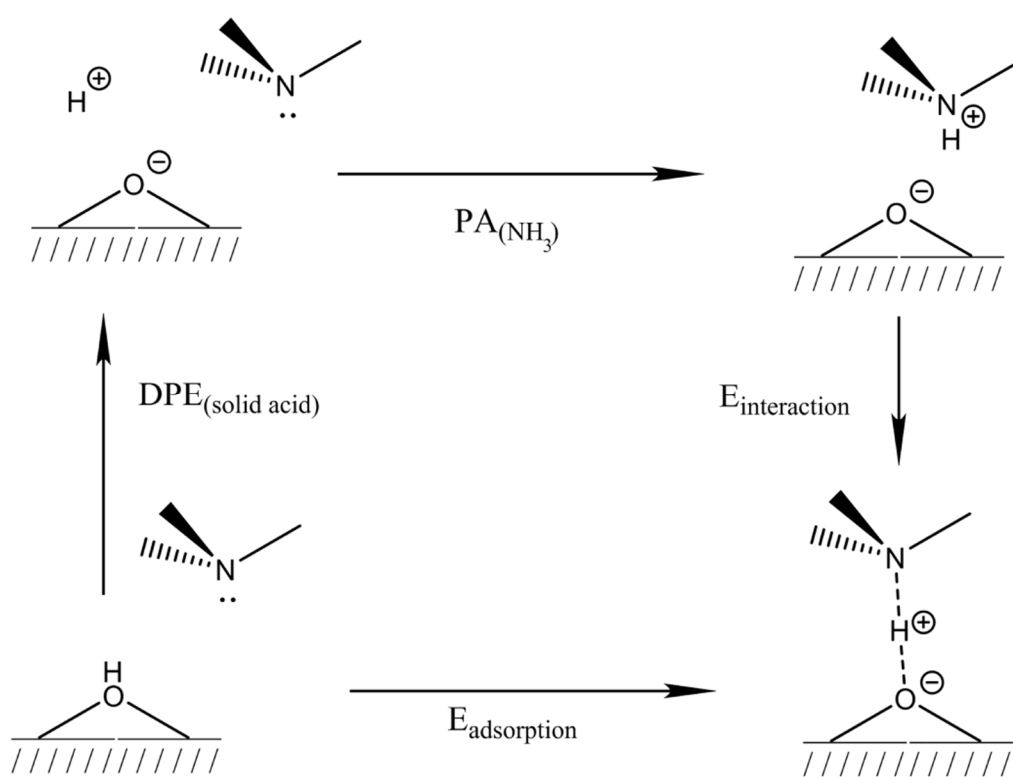


Figure 5.10 Energy decomposition for the adsorption of a probe base molecule on a Brønsted acid site. This involves the deprotonation of the acid, the gas phase protonation of the base and the interaction of the protonated base onto the conjugate base.

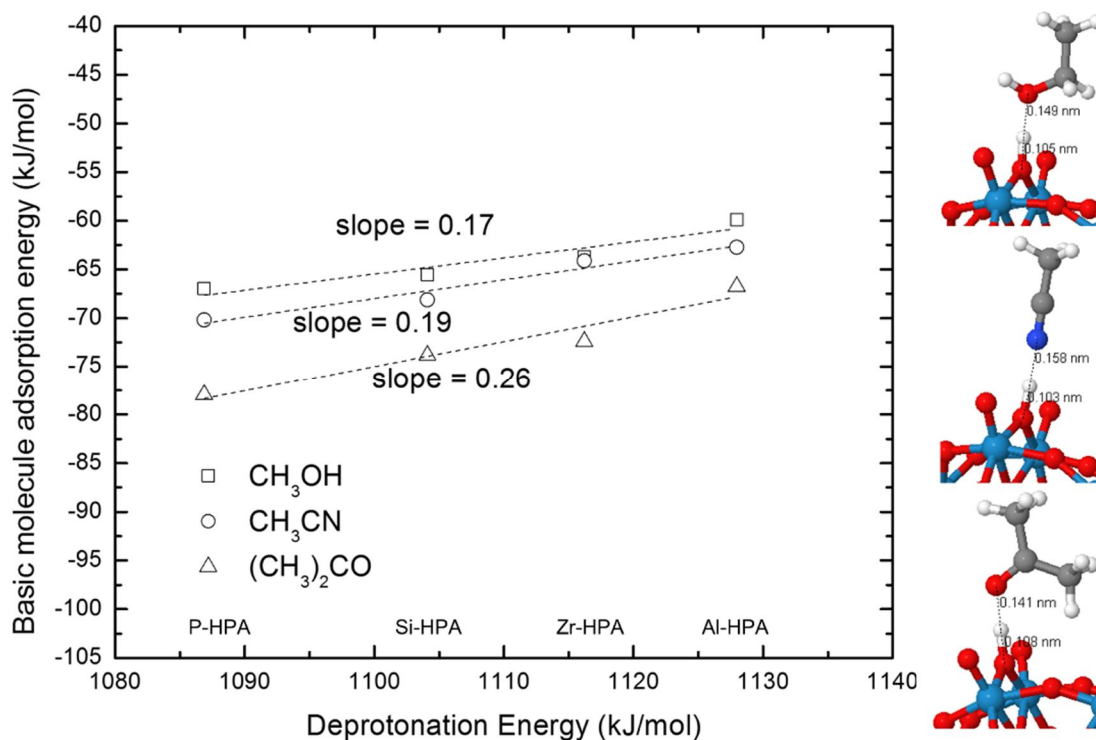


Figure 5.11 DFT-calculated adsorption energies for a series of basic probe molecules (methanol (square), acetonitrile (circle), and acetone (triangle)) as a function of the acid strength of different Keggin HPAs.

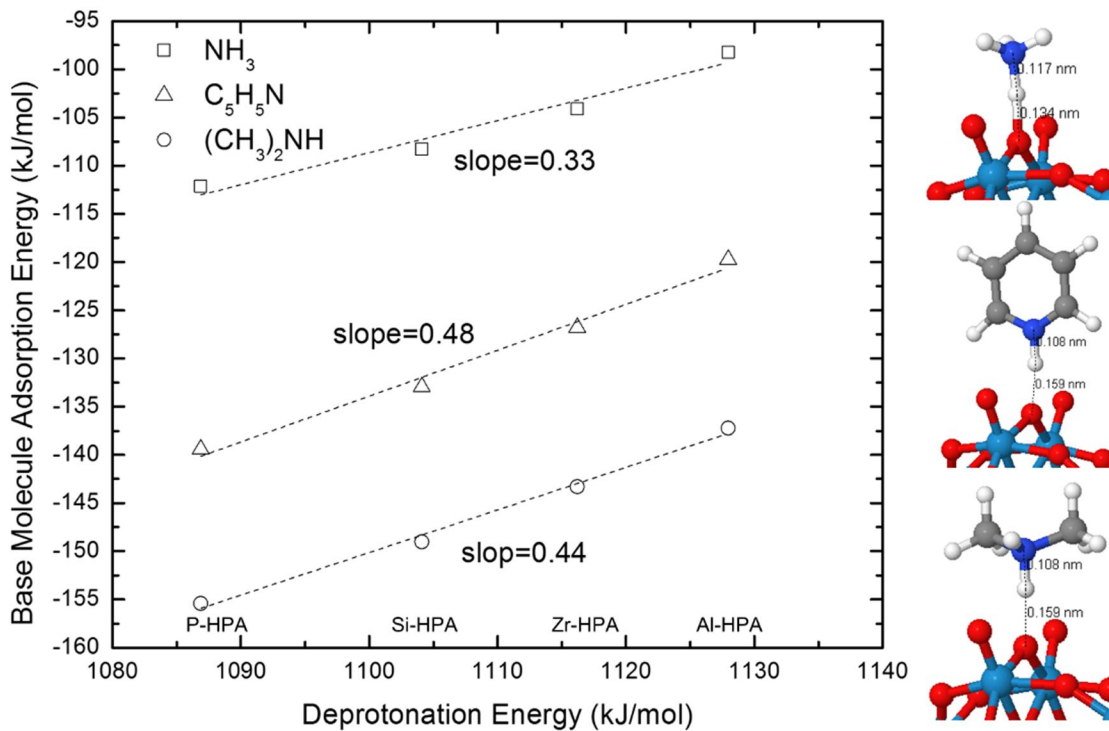


Figure 5.12 DFT-calculated adsorption energies for a series of basic probe molecules (ammonia (square), pyridine (triangle), and dimethylamine (circle)) as a function of the acid strength of different Keggin HPAs.

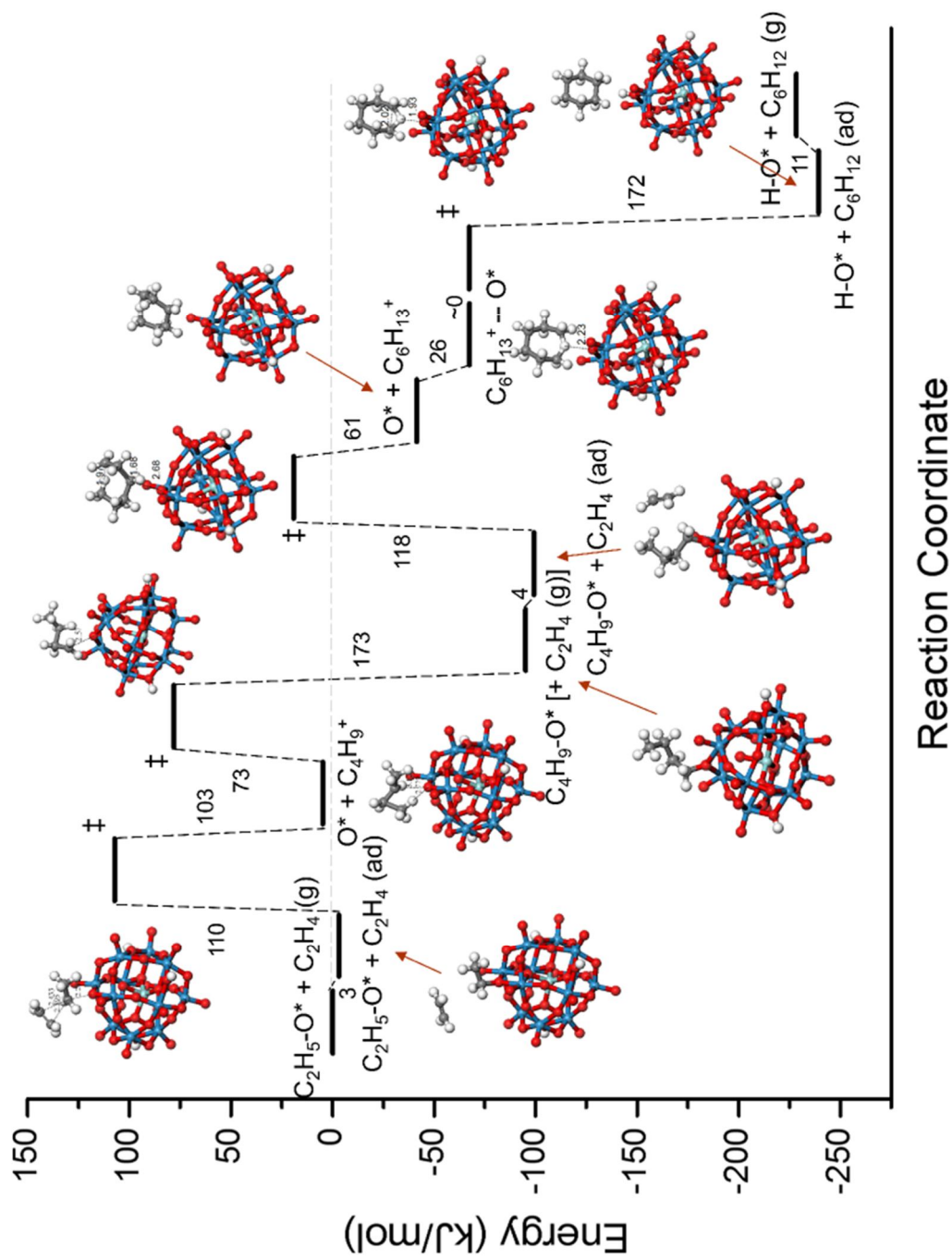


Figure 5.13 DFT-calculated plausible reaction path for the oligomerization of ethylene and ethoxide to form cyclohexane over one of the Keggin type of Zr- polyoxotungstates ($H_4ZrW_{12}O_{40}$).

References

1. W.O. Haag and R.M. Dessau. *Duality of Mechanism in Acid Catalyzed Paraffin Cracking*. in *8th International Congress on Catalysis*. 1984. Berlin, Germany.
2. M. Guisnet and P. Magnoux, *Deactivation by coking of zeolite catalysts. Prevention of deactivation. Optimal conditions for regeneration*. *Catalysis Today*, 1997. **36**(4): p. 477-483.
3. P. Magnoux, P. Cartraud, S. Mignard, and M. Guisnet, *Coking, aging, and regeneration of zeolites: II. Deactivation of HY zeolite during n-heptane cracking*. *Journal of Catalysis*, 1987. **106**(1): p. 235-241.
4. P. Magnoux, P. Cartraud, S. Mignard, and M. Guisnet, *Coking, aging, and regeneration of zeolites: III. Comparison of the deactivation modes of H-mordenite, HZSM-5, and HY during n-Heptane cracking*. *Journal of Catalysis*, 1987. **106**(1): p. 242-250.
5. R.D. Wilson, D.G. Barton, C.D. Baertsch, and E. Iglesia, *Reaction and Deactivation Pathways in Xylene Isomerization on Zirconia Modified by Tungsten Oxide*. *Journal of Catalysis*, 2000. **194**(2): p. 175-187.
6. N. Soultanidis, W. Zhou, A.C. Psarras, A.J. Gonzalez, E.F. Iliopoulou, C.J. Kiely, I.E. Wachs, and M.S. Wong, *Relating n-Pentane Isomerization Activity to the Tungsten Surface Density of WO_x/ZrO_2* . *Journal of the American Chemical Society*, 2010. **132**(38): p. 13462-13471.
7. Y.-H. Chin, W.E. Alvarez, and D.E. Resasco, *Sulfated zirconia and tungstated zirconia as effective supports for Pd-based SCR catalysts*. *Catalysis Today*, 2000. **62**(2-3): p. 159-165.
8. D. Barton, S. Soled, and E. Iglesia, *Solid acid catalysts based on supported tungsten oxides*. *Topics in Catalysis*, 1998. **6**(1-4): p. 87-99.
9. D.G. Barton, S.L. Soled, G.D. Meitzner, G.A. Fuentes, and E. Iglesia, *Structural and Catalytic Characterization of Solid Acids Based on Zirconia Modified by Tungsten Oxide*. *Journal of Catalysis*, 1999. **181**(1): p. 57-72.
10. H. Xu, *A First Principles Analysis of Tungstate Domain Size Effects on the Acidity and Reactivity of WO_x/ZrO_2 Catalysts*, Master's Thesis in Department of Chemical Engineering. 2011, University of Virginia: Charlottesville, VA.
11. W. Zhou, E.I. Ross-Medgaarden, W.V. Knowles, M.S. Wong, I.E. Wachs, and C.J. Kiely, *Identification of active Zr- WO_x clusters on a ZrO_2 support for solid acid catalysts*. *Nature Chemistry*, 2009. **1**(9): p. 722-728.
12. E.I. Ross-Medgaarden, W.V. Knowles, T. Kim, M.S. Wong, W. Zhou, C.J. Kiely, and I.E. Wachs, *New insights into the nature of the acidic catalytic active sites present in ZrO_2 -supported tungsten oxide catalysts*. *Journal of Catalysis*, 2008. **256**(1): p. 108-125.
13. M. Scheithauer, R.K. Grasselli, and H. Knözinger, *Genesis and Structure of WO_x/ZrO_2 Solid Acid Catalysts*. *Langmuir*, 1998. **14**(11): p. 3019-3029.
14. M. Scheithauer, T.K. Cheung, R.E. Jentoft, R.K. Grasselli, B.C. Gates, and H. Knözinger, *Characterization of WO_x/ZrO_2 by Vibrational Spectroscopy and n-Pentane Isomerization Catalysis*. *Journal of Catalysis*, 1998. **180**(1): p. 1-13.
15. H.N. Miras, J. Yan, D.-L. Long, and L. Cronin, *Engineering polyoxometalates with emergent properties*. *Chemical Society Reviews*, 2012. **41**(22): p. 7403-7430.
16. X. Lopez, J.J. Carbo, C. Bo, and J.M. Poblet, *Structure, properties and reactivity of polyoxometalates: a theoretical perspective*. *Chemical Society Reviews*, 2012. **41**(22): p. 7537-7571.
17. R. Villanneau, H. Carabineiro, X. Carrier, R. Thouvenot, P. Herson, F. Lemos, F. Ramôa Ribeiro, and M. Che, *Synthesis and Characterization of Zr(IV) Polyoxotungstates as Molecular Analogues of Zirconia-Supported Tungsten Catalysts*. *The Journal of Physical Chemistry B*, 2004. **108**(33): p. 12465-12471.
18. T. Edwards and L. Maurice, *HyTech Fuels/Fuel System Research AIAA 98-1562*, in *36th Aerospace Sciences Meeting & Exhibit*. 1998: Reno, NV.
19. T. Edwards and S. Zabarnick, *Supercritical fuel deposition mechanisms*. *Industrial & Engineering Chemistry Research*, 1993. **32**(12): p. 3117-3122.
20. D.T. Wickham, G.O. Alptekin, J.R. Engel, and M.E. Karpuk, *Additives to Reduce Coking in Endothermic Fuel Heat Exchangers AIAA 99-2215*, in *35th AIAA/ASME/SAE/ASEE Joint Propulsion Conference*. 1999: Los Angeles, CA.

21. H. Huang, D.R. Sobel, and L.J. Spadaccini, *Endothermic Heat-Sink of Hydrocarbon Fuels for Scramjet Cooling AIAA 2002-3871*, in *38th AIAA/ASME/SAE/ASEE Joint Propulsion Conference*. 2002: Indianapolis, IA.
22. T. Edwards, *Cracking and Deposition Behavior of Supercritical Hydrocarbon Aviation Fuels*. Combustion Science and Technology, 2006. **178**(1-3): p. 307-334.
23. N. Gascoïn, G. Abraham, and P. Gillard, *Synthetic and jet fuels pyrolysis for cooling and combustion applications*. Journal of Analytical and Applied Pyrolysis, 2010. **89**(2): p. 294-306.
24. F. Meng, G. Liu, S. Qu, L. Wang, X. Zhang, and Z. Mi, *Catalytic Cracking and Coking of Supercritical n-Dodecane in Microchannel Coated with HZSM-5 Zeolites*. Industrial & Engineering Chemistry Research, 2010. **49**(19): p. 8977-8983.
25. R. Jiang, G. Liu, Z. You, M. Luo, X. Wang, L. Wang, and X. Zhang, *On the Critical Points of Thermally Cracked Hydrocarbon Fuels under High Pressure*. Industrial & Engineering Chemistry Research, 2011. **50**(15): p. 9456-9465.
26. B. Dimon, P. Cartraud, P. Magnoux, and M. Guisnet, *Coking, aging and regeneration of zeolites: XIV. Kinetic study of the formation of coke from propene over USHY and H-ZSM-5*. Applied Catalysis A: General, 1993. **101**(2): p. 351-369.
27. K. Moljord, P. Magnoux, and M. Guisnet, *Coking, aging and regeneration of zeolites XV. Influence of the composition of HY zeolites on the mode of formation of coke from propene at 450°C*. Applied Catalysis A: General, 1995. **122**(1): p. 21-32.
28. M. Guisnet and P. Magnoux, *Composition of the Carbonaceous Compounds Responsible for Zeolite Deactivation. Modes of Formation*, in *Zeolite Microporous Solids: Synthesis, Structure, and Reactivity*, E. Derouane, F. Lemos, C. Naccache, and F. Ribeiro, Editors. 1992, Springer Netherlands. p. 437-456.
29. M. Guisnet and P. Magnoux, *Deactivation of Zeolites by Coking. Prevention of Deactivation and Regeneration*, in *Zeolite Microporous Solids: Synthesis, Structure, and Reactivity*, E. Derouane, F. Lemos, C. Naccache, and F. Ribeiro, Editors. 1992, Springer Netherlands. p. 457-474.
30. G. Kresse and J. Hafner, *Ab initio molecular dynamics for liquid metals*. Phys. Rev. B, 1993. **47**: p. 558.
31. G. Kresse and J. Hafner, *Ab initio molecular-dynamics simulation of the liquid-metal-amorphous-semiconductor transition in germanium*. Phys. Rev. B, 1994. **49**: p. 14251.
32. G. Kresse and J. Furthmüller, *Efficiency of ab-initio total energy calculations for metals and semiconductors using a plane-wave basis set*. Comput. Mat. Sci., 1996. **6**: p. 15.
33. G. Kresse and J. Furthmüller, *Efficient iterative schemes for ab initio total-energy calculations using a plane-wave basis set*. Phys. Rev. B, 1996. **54**: p. 11169.
34. J.P. Perdew, K. Burke, and M. Ernzerhof, *Generalized Gradient Approximation Made Simple*. Phys. Rev. Lett., 1996. **77**: p. 3865.
35. J.P. Perdew, K. Burke, and M. Ernzerhof, *Erratum: Generalized Gradient Approximation Made Simple*. Phys. Rev. Lett., 1997. **78**: p. 1396.
36. P.E. Blöchl, *Projector augmented-wave method*. Phys. Rev. B, 1994. **50**: p. 17953.
37. G. Kresse and D. Joubert, *From ultrasoft pseudopotentials to the projector augmented-wave method*. Phys. Rev. B, 1999. **59**: p. 1758.
38. H. Jónsson, G. Mills, and K.W. Jacobsen, *Nudged Elastic Band Method for Finding Minimum Energy Paths of Transitions*, in *Classical and Quantum Dynamics in Condensed Phase Simulations*, B.J. Berne, G. Ciccotti, and D.F. Coker, Editors. 1998, World Scientific. p. 385-404.
39. H. Graeme and J. Hannes, *A dimer method for finding saddle points on high dimensional potential surfaces using only first derivatives*. The Journal of Chemical Physics, 1999. **111**(15): p. 7010-7022.
40. J. Macht, M.J. Janik, M. Neurock, and E. Iglesia, *Catalytic Consequences of Composition in Polyoxometalate Clusters with Keggin Structure*. Angewandte Chemie International Edition, 2007. **46**(41): p. 7864-7868.
41. H.J. Monkhorst and J.D. Pack, *Special points for Brillouin-zone integrations*. Physical Review B, 1976. **13**(12): p. 5188-5192.
42. A. Zecchina, S. Bordiga, G. Spoto, D. Scarano, G. Spano, and F. Geobaldo, *IR spectroscopy of neutral and ionic hydrogen-bonded complexes formed upon interaction of CH₃OH, C₂H₅OH, (CH₃)₂O, (C₂H₅)₂O and C₄H₈O with H-Y, H-ZSM-5 and H-mordenite: comparison with analogous adducts formed on the H-Nafion superacidic membrane*. Journal of the Chemical Society, Faraday Transactions, 1996. **92**(23): p. 4863-4875.

43. H.G. Karge, *Comparative Measurements on Acidity of Zeolites*, in *Studies in Surface Science and Catalysis*, G. Öhlmann, H. Pfeifer, and R. Fricke, Editors. 1991, Elsevier. p. 133-156.
44. N. Cardona-Martinez and J.A. Dumesic, *Applications of Adsorption Microcalorimetry to the Study of Heterogeneous Catalysis*, in *Advances in Catalysis*, D.D. Eley, H. Pines, and P.B. Weisz, Editors. 1992, Academic Press. p. 149-244.
45. P. Batamack, C. Doremieux-Morin, R. Vincent, and J. Fraissard, *Broad-line proton NMR: a new application for studying the Brønsted acid strength of solids*. *The Journal of Physical Chemistry*, 1993. **97**(38): p. 9779-9783.
46. M. Brändle and J. Sauer, *Acidity Differences between Inorganic Solids Induced by Their Framework Structure. A Combined Quantum Mechanics/Molecular Mechanics ab Initio Study on Zeolites*. *Journal of the American Chemical Society*, 1998. **120**(7): p. 1556-1570.
47. I.A. Koppel, P. Burk, I. Koppel, I. Leito, T. Sonoda, and M. Mishima, *Gas-Phase Acidities of Some Neutral Brønsted Superacids: A DFT and ab Initio Study*. *Journal of the American Chemical Society*, 2000. **122**(21): p. 5114-5124.
48. H.V. Brand, L.A. Curtiss, and L.E. Iton, *Ab initio molecular orbital cluster studies of the zeolite ZSM-5. 1. Proton affinities*. *The Journal of Physical Chemistry*, 1993. **97**(49): p. 12773-12782.
49. M.J. Janik, J. Macht, E. Iglesia, and M. Neurock, *Correlating Acid Properties and Catalytic Function: A First-Principles Analysis of Alcohol Dehydration Pathways on Polyoxometalates*. *The Journal of Physical Chemistry C*, 2009. **113**(5): p. 1872-1885.
50. C. Lo and B.L. Trout, *Density-functional theory characterization of acid sites in chabazite*. *Journal of Catalysis*, 2004. **227**(1): p. 77-89.
51. G. Sastre and A. Corma, *Relation between structure and Lewis acidity of Ti-Beta and TS-1 zeolites: A quantum-chemical study*. *Chemical Physics Letters*, 1999. **302**(5-6): p. 447-453.
52. F. Bessac and G. Frenking, *Why Is BCl₃ a Stronger Lewis Acid with Respect to Strong Bases than BF₃?* *Inorganic Chemistry*, 2003. **42**(24): p. 7990-7994.
53. H. Fang, A. Zheng, Y. Chu, and F. Deng, *¹³C Chemical Shift of Adsorbed Acetone for Measuring the Acid Strength of Solid Acids: A Theoretical Calculation Study*. *The Journal of Physical Chemistry C*, 2010. **114**(29): p. 12711-12718.
54. S. Kotrel, H. Knözinger, and B.C. Gates, *The Haag-Dessau mechanism of protolytic cracking of alkanes*. *Microporous and Mesoporous Materials*, 2000. **35-36**(0): p. 11-20.
55. F.C. Jentoft and B.C. Gates, *Solid-acid-catalyzed alkane cracking mechanisms: evidence from reactions of small probe molecules*. *Topics in Catalysis*, 1997. **4**(1-2): p. 1-13.
56. S.M. Babitz, B.A. Williams, J.T. Miller, R.Q. Snurr, W.O. Haag, and H.H. Kung, *Monomolecular cracking of n-hexane on Y, MOR, and ZSM-5 zeolites*. *Applied Catalysis A: General*, 1999. **179**(1-2): p. 71-86.
57. S.A. Zymunt, L.A. Curtiss, P. Zapol, and L.E. Iton, *Ab Initio and Density Functional Study of the Activation Barrier for Ethane Cracking in Cluster Models of Zeolite H-ZSM-5*. *The Journal of Physical Chemistry B*, 2000. **104**(9): p. 1944-1949.
58. X. Zheng and P. Blowers, *Reactivity of Alkanes on Zeolites: A Computational Study of Propane Conversion Reactions*. *The Journal of Physical Chemistry A*, 2005. **109**(47): p. 10734-10741.
59. T. Bučko, L. Benco, J. Hafner, and J.G. Ángyán, *Monomolecular cracking of propane over acidic chabazite: An ab initio molecular dynamics and transition path sampling study*. *Journal of Catalysis*, 2011. **279**(1): p. 220-228.
60. R. Gounder and E. Iglesia, *The catalytic diversity of zeolites: confinement and solvation effects within voids of molecular dimensions*. *Chemical Communications*, 2013. **49**(34): p. 3491-3509.
61. R. Gounder and E. Iglesia, *The Roles of Entropy and Enthalpy in Stabilizing Ion-Pairs at Transition States in Zeolite Acid Catalysis*. *Accounts of Chemical Research*, 2011. **45**(2): p. 229-238.
62. R. Gounder and E. Iglesia, *Catalytic Consequences of Spatial Constraints and Acid Site Location for Monomolecular Alkane Activation on Zeolites*. *Journal of the American Chemical Society*, 2009. **131**(5): p. 1958-1971.
63. L. Vilà-Nadal, S. Romo, X. López, and J. Poblet, *Structural and Electronic Features of Wells-Dawson Polyoxometalates*, in *Complexity in Chemistry and Beyond: Interplay Theory and Experiment*, C. Hill and D.G. Musaev, Editors. 2012, Springer Netherlands. p. 171-183.
64. J.A. Miller, M.J. Pilling, and J. Troe, *Unravelling combustion mechanisms through a quantitative understanding of elementary reactions*. *Proceedings of the Combustion Institute*, 2005. **30**(1): p. 43-88.

Chapter 6 Conclusions and Recommendations

6.1 Conclusions

Catalytic dehydrogenation and catalytic cracking of hydrocarbon fuels present two possible endothermic reactions that may be used in the regenerative cooling of hypersonic jet engines as well as catalytic combustion of jet fuels. First-principles density functional theory (DFT) calculations were carried out to provide fundamental insights into the reaction pathways and mechanisms that control catalytic dehydrogenation and cracking of model alkanes over unsupported and supported model Pt, Co, and Au clusters and WO_x/ZrO_2 solid acid catalysts, respectively. The work is focused on the fundamental efforts aimed at establishing the influence of metal particle size, morphology and composition on the catalytic activity and selectivity for nanoparticle; elucidating the interaction between the metal or metal oxide nanoparticles and the support; and understanding important paths that can lead to catalytic deactivation.

Propane and cyclohexane were used as surrogate molecules to examine the reaction paths and mechanisms for the molecules involved in the catalytic dehydrogenation over sub-nanometer and nanometer supported Pt and Co catalysts. More specifically we find the following,

- Within the studied size range of Pt_n ($n=4\sim 9,13$) and Co_n ($n=5\sim 14$), Pt_n clusters had much lower C-H bond activation barriers than Co_n clusters. The Pt_n clusters were found to have higher ionization potentials (IP) and electron affinities (EA) allowing

them to accept electrons from propane in the transition state in activating the secondary C-H bond of propane. Co_n clusters, on the other hand, donate electrons to propane and have a higher C-H bond activation barrier. The intrinsic barriers for C-H bond activation were found to directly correlate with the chemical hardness of Pt_n and Co_n clusters.

- Changes in the size of carbon nanotubes used to support Pt_n clusters were found to influence the reactivity of the Pt_n cluster. Charge transfer from the Pt cluster to the CNT substrate induces a charge polarization resulting in a negative charge on the top Pt atom that is not bonding to CNT. The activation of the C-H bond at this site has a much higher barrier than that on freestanding Pt_5 cluster, which is in agreement with experimental observation that anionic Pt clusters are less reactive than charge neutral and cationic ones.
- The site-averaged rates of cyclohexene dehydrogenation and cyclohexene desorption calculated over cubo-octahedral Pt_n nanoparticles at high surface coverages show that smaller particles favor cyclohexene dehydrogenation to form benzene while larger particles favor desorption of cyclohexene. The DFT-calculated selectivities and their trends are in good agreement with experimental findings.

The catalytic dehydrogenation studies over nanometer supported metal particles were extended to catalytic oxidation pathways which are important in the subsequent catalytic

combustion of the fuel. More specifically we examined the oxidative dehydrogenation of cyclohexene, an important initial step in catalytic oxidation, over Au/Co₃O₄.

- Au nanoparticles transfer electrons to Co₃O₄ support upon their adsorption. The charge is localized near the gold-oxide interface. The increased electron density at the interfacial Co^{octa} cations weakens the Co-O bond and increases the hydrogen affinity of the O site. This increase in hydrogen affinity in interfacial O site results in a lower activation barrier for the initial C-H bond activation of cyclohexane at the Au-Co₃O₄ interface. The partially reduced Co^{octa} cation at the interfacial O-vacancy also enhances the dissociation of molecular O₂ at this site which results in the formation of a reactive mono-oxygen surface species.

In the final work, we explored the solid acid catalyzed cracking of alkanes as a second viable reaction for the removal of waste heat. Tungstated zirconia is thought to be acidic and thermally stable under reactions conditions.

- Zr-containing polyoxotungstates with a variety of 3D structures were found to be more acidic (lower values of DPE) than 2D surface tungstate clusters supported on ZrO₂. The rates of these reactions were all directly correlated to the acidity of the catalyst. However the sensitivity of activation barrier to the change in DPE are different in different reactions, which may help to guide the rational design of a solid acid catalyst that can promote cracking and minimize coking.

6.2 Recommendations

- Sub-nanometer clusters tend to restructure upon the adsorption of adsorbates and adapt their structures to the transformation of adsorbed molecules. A study focused on the fluxionality of small clusters is strongly recommended. A sampling of possible structural change of clusters during the reaction of adsorbed molecules should be performed, instead of examining only one single structure that are thought to be the “most stable”. Molecular dynamics and Monte Carlo simulation methods can be employed to facilitate this research.
- Thermal decomposition experiments of Au/Co₃O₄ and Co₃O₄ is recommended to be carried out, which will provide invaluable direct thermal dynamics information of phase transitions and bond strengths.
- Creating a full list of acid catalyzed reactions with their sensitivity to the change of Brønsted acidity (measured by DPE) is strongly recommended, by feeding these information into a kinetic model one should be able to solve for an optimal DPE and optimal acid site densities that result in a high catalytic selectivity towards certain products.